8-1-2012

Thermally Actuated Resonant Silicon Crystal Nanobalances

Arash Hajjam
University of Denver

THERMALLY ACTUATED RESONANT SILICON CRYSTAL NANOBALANCES

A Dissertation

Presented to

the Faculty of Engineering and Computer Science

University of Denver

In Partial Fulfillment

of the Requirements for the Degree

Doctor of Philosophy

by

Arash Hajjam

August 2012

Advisor: Siavash Pourkamali

Author: Arash Hajjam
Title: THERMALLY ACTUATED RESONANT SILICON CRYSTAL NANOBALANCES
Advisor: Siavash Pourkamali
Degree Date: August 2012

Abstract

As the potential emerging technology for next generation integrated resonant sensors and frequency references as well as electronic filters, micro-electro-mechanical resonators have attracted a lot of attention over the past decade. As a result, a wide variety of high frequency micro/nanoscale electromechanical resonators have recently been presented. MEMS resonators, as low-cost highly integrated and ultra-sensitive mass sensors, can potentially provide new opportunities and unprecedented capabilities in the area of mass sensing. Such devices can provide orders of magnitude higher mass sensitivity and resolution compared to Film Bulk Acoustic resonators (FBAR) or the conventional quartz and Surface Acoustic Wave (SAW) resonators due to their much smaller sizes and can be batch-fabricated and utilized in highly integrated large arrays at a very low cost.

In this research, comprehensive experimental studies on the performance and durability of thermally actuated micromechanical resonant sensors with frequencies up to tens of MHz have been performed. The suitability and robustness of the devices have been demonstrated for mass sensing applications related to air-borne particles and organic gases.

In addition, due to the internal thermo-electro-mechanical interactions, the active resonators can turn some of the consumed electronic power back into the mechanical structure and compensate for the mechanical losses. Therefore, such resonators can provide self-sustained-oscillation without the need for any electronic circuitry. This

unique property has been deployed to demonstrate a prototype self-sustained sensor for air-borne particle monitoring.

I have managed to overcome one of the obstacles for MEMS resonators, which is their relatively poor temperature stability. This is a major drawback when compared with the conventional quartz crystals. A significant decrease of the large negative TCF for the resonators has been attained by doping the devices with a high concentration of phosphorous, resulting in even slightly positive TCF for some of the devices. This is also expected to improve the phase noise characteristics of oscillators implemented utilizing such frequency references by eliminating the sharp dependence to electronic noise in the resonator bias current.

Finally it is well known that non-uniformities in fabrication of MEMS resonators lead to variations in their frequency. I have proposed both active (non-permanent) and permanent frequency modification to compensate for variations in frequency of the MEMS resonators.

ACKNOWLEDGEMENTS

First and foremost, I want to thank my advisor and mentor, Professor Siavash Pourkamali for his continuous support, encouragement, and advice. I appreciate all his assistance, including the dedication of his time, ideas, and funding to make my Ph.D. experience productive, exciting and more importantly possible. I would also like to thank my committee members, Professors James C. Wilson, Corinne Lengsfeld and Mohammad Matin and for their help, guidance and support.

I would like to thank all my past and present colleagues; especially Amir Rahafrooz who was the one that initially gave me tips on how to start working inside the clean-room. Amir was much more than a colleague to me. There had been many times which we had to stay all night long in order to catch conference deadlines. I have to thank him as a loyal, supportive close friend. I would like to thank Andrew Logan, Yedan Guo, Kristine Dietrich and Brandon Bourn who worked for me as undergraduate assistants. They were all very responsible and special praise should be given for their efforts.

I would like to express my appreciation to the staff in both the Electrical and Computer Engineering and Mechanical and Materials Engineering departments; Assistant to the chairs, Crystal Harris and Renee Carvalho, for their continuous help. Gerald R. Edelstein and Jon Buckley for their help providing me with the needed equipments and components and Tim Sheu for helping me with all my IT related problems.

Last but not least, I would like to thank my parents Mahboobeh and Sohrab who raised me with love and supported me in all my pursuits. They have truly devoted their life to the comfort and success of their children and my love, Neekan Aeini that has been the main source of inspiration and motivation in most of my recent success.

Table of Contents

LIST OF TABLES

LIST OF FIGURES

LIST OF TERMS

AC: Alternating Current

AlN: Aluminum Nitride

BAR: Bulk Acoustic wave Resonator

BAW: Bulk Acoustic Wave

BOX: Buffer Oxide

CMOS: Complementary Metal-Oxide Semiconductor

DC: Direct Current

DRIE: Deep Reactive Ion Etching

EPA: Environmental Protection Agency

FBAR: Film Bulk Acoustic Resonator

HF: High Frequency

HF: Hydrofluoric Acid

IBAR: I-shaped Bulk Acoustic Resonator

IC: Integrated Circuit

KOH: Potassium Hydroxide

MEM: Micro-Electro-Mechanical

MEMS: Micro-Electro-Mechanical Systems

NEMS: Nano-Electro-Mechanical Systems

PCB: Printed circuit board

Q: Quality Factor

QCM: Quartz Crystal Microbalance

RIE: Reactive Ion Etching

SAW: Surface Acoustic Wave

SCS: Single Crystal Silicon

SEM: Scanning Electron Microscopy

SOI: Silicon on Insulator

TCF: Temperature Coefficient of Frequency

TCXO: Temperature Compensated Quartz Oscillator

VOC: Volatile Organic Compound

VHF: Very High Frequency

1. INTRODUCTION

MEMS/NEMS resonators, as low-cost highly integrated and ultra-sensitive mass sensors, can potentially provide new opportunities and unprecedented capabilities as ultra sensitive mass sensors in the micro and nanoscale. Such devices can provide orders of magnitude higher mass sensitivity and resolution compared to Film Bulk Acoustic resonators (FBAR) or the conventional quartz and Surface Acoustic Wave (SAW) resonators due to their much smaller sizes and can be batch-fabricated and utilized in highly integrated large arrays at a very low cost. MEMS resonators also carry a lot of potential for applications such as highly stable frequency references. Different types of MEMS oscillators have been developed over the past few years that are becoming more popular and commercially available. The main driving force for such MEMS products is their small size, the fact that they could be batch fabricated in high quantities at a very low cost and also their potential compatibility with CMOS integrated circuit technologies which could lead to on-chip integrated frequency references.

In this thesis, comprehensive experimental studies on the performance of thermal-piezoresistive resonant devices for mass sensing applications related to air-borne particles and organic gases has been presented. A temperature compensation technique as well as both reversible frequency tuning (non-permanent) and permanent frequency trimming

techniques have also been demonstrated to compensate for variations in frequency of the MEMS resonators.

1.1 Mechanical Resonators

A mechanical resonator is a device or structure that upon excitation has the potential to exhibit resonance or resonant characteristics. It naturally oscillates at some frequencies, known as its resonant frequencies which depend on its dimensions and physical properties. At this frequency, it has the potential to store parts of the excitation energy which causes an increase in its vibration amplitude. A classical example of such in macroscale is a guitar string. Every guitar string, depending on its length, tension, and properties of its structural material has a certain frequency of vibration. In case of guitar the resonance frequencies of all strings fall in the audio frequency range (20Hz-20 kHz). If the resonator dimensions are scaled down into the micrometer range, resonance frequencies in the order of MHz and even GHz are achievable.

A mechanical resonator can be modeled as a mass, spring, and damper system in mechanics. Figure 1.1 shows a mass (m), spring (k) and damper (D) system as well as its frequency response with the resonance frequency of f_0. Transfer function of such a system which relates the applied actuation force (F) to the displacement of the resonator (x) can be written as follows:

$$\frac{x(s)}{F(s)} = \frac{1}{k\left(\frac{s^2}{\omega_0^2}+\frac{s}{\omega_0 Q}+1\right)} \tag{1.1}$$

where s is the Laplace transform parameter, ω_0 and Q are the angular resonance frequency and quality factor of the resonator respectively and are related to the component values as follows:

$$\omega_0 = 2\pi f_0 = \sqrt{\frac{k}{m}} \tag{1.2}$$

$$Q = \frac{\sqrt{k.m}}{D} \tag{1.3}$$

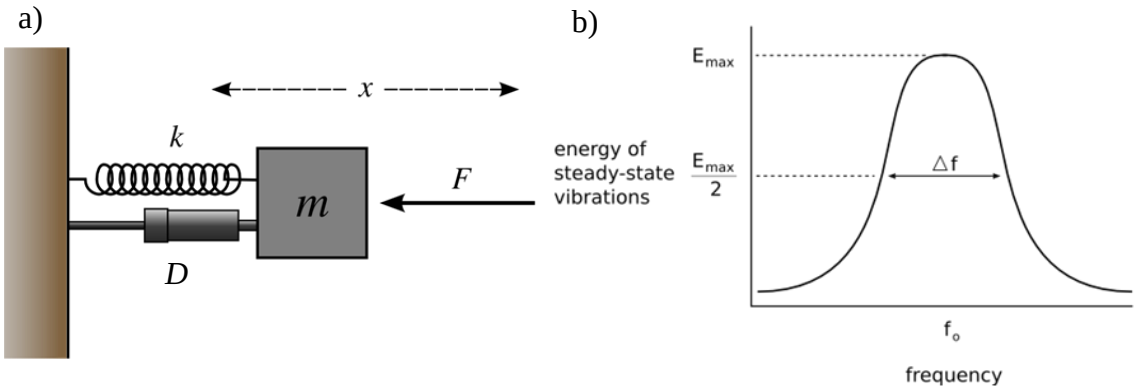

Figure 1.1. a) A mass connected to a damper (D) and a spring (k) to form a second order mechanical system. b) The bandwidth, Δ*f*, of a damped oscillator is shown on a graph of energy versus frequency. The Q factor of the damped oscillator is $f_0/\Delta f$. The higher the Q, the narrower and sharper the peak is [1].

Both the frequency and quality factor (Q) values can be found from the frequency response of the resonator; resonance frequency is the frequency at which the vibration amplitude maximizes which is in fact in the center of the passband of the frequency response. On the other hand, quality factor can be defined as:

$$Q = \frac{f_0}{\Delta f} = \frac{\omega_0}{\Delta \omega} \tag{1.4}$$

where Δf and Δω are the width of the frequency range and the angular frequency range out of which the energy of the resonator decreases to half of its maximum value (Fig. 1.1b). In the context of resonators, Q is defined in terms of the ratio of the energy stored in the resonator to the energy supplied by a generator, per cycle, to keep signal amplitude constant, at the resonant frequency, where the stored energy is constant with time [2]. Since Q is the ratio of the resonant or center frequency of a resonator to the bandwidth, Q is therefore a measurement of the sharpness of the response of system to the resonant

frequency. Therefore, a resonant frequency with a high Q factor would decay more quickly as the frequency moves away from the resonant frequency, and it would be more accurate and stable. Q factor values are therefore very important during frequency measurements.

1.2 Mechanical Resonator Applications

MEMS resonators carry a lot of potential for applications such as highly stable frequency references [2] or chemical and biological sensors. Different types of MEMS oscillators have been developed over the past few years that are now commercially available and becoming more popular.

The main driving force for such MEMS products is their small size, the fact that they could be batch fabricated in high quantities at a very low cost and also their potential compatibility with CMOS integrated circuit technologies which could lead to on-chip integrated frequency references.

MEMS resonators and oscillators have proven to be suitable as mass sensors for a variety of applications such as airborne particle mass measurement [3], volatile organic compound [4] and moisture detection [5]. The increase in the mass of the structure causes the frequency of the resonator to decrease based on Eq. (1.2). The mass sensitivity of the resonators can be theoretically calculated as follows:

$$f = \frac{1}{2\pi}\sqrt{\frac{k}{m}} \qquad \Rightarrow \qquad \frac{\Delta f}{f} = -\frac{\Delta m}{2m} \tag{1.5}$$

where Δm is the change in mass and Δf is the change in resonance frequency of the resonator due to the added mass. Based on Eq. (1.5) it is evident that by using smaller resonators with higher resonance frequencies, the frequency shifts resulting from the

same amount of mass change are bound to also increase therefore making the resonator more sensitive to the added mass.

1.3 Mechanical Resonator Transduction

In order to be able to utilize a mechanical resonator as a highly stable frequency reference or for sensory applications, a mechanism is required to actuate the resonator and initiate its mechanical vibration. Therefore, a mechanical force with proper amplitude and frequency should be applied to the resonator. After the vibration is started, another mechanism is required to measure the vibration amplitude of the resonator and convert it into a readable signal. A variety of different transduction mechanisms have been investigated and utilized for micro mechanical resonators by different researchers. A brief description of some of the most popular of such mechanisms follows.

1.3.1 Piezoelectric Transduction

The generation of an electric charge in certain nonconducting materials, such as quartz crystals, when they are subjected to mechanical stress, or the generation of vibrations in such materials when they are subjected to an electric field is known as the piezoelectric effect. Piezoelectric materials exposed to a constant electric field tend to vibrate at a precise frequency with very little variation. On the other hand, by applying a mechanical force to such materials, an electric field and polarization of electric charges occurs inside the material that could be sensed and used to detect the vibration amplitude of the resonator [2]. Therefore piezoelectricaly actuated resonators can be utilized for time keeping and sensory application (Fig. 1.2)

The nature of the piezoelectric effect is closely related to the occurrence of electric dipole moments in solids. The piezoelectric material is composed of ions or

molecules with asymmetric charge surroundings. Dipoles near each other tend to be aligned in regions called Weiss domains [6]. The domains are usually randomly oriented, but can be aligned by a strong electric field applied across the material [6]. Alignment of the dipoles due to the applied electric field result in the material stretching along the direction of the applied electric field and therefore generating a mechanical force.

Piezoelectric resonators such as Quartz Crystal Microbalance (QCM) [7], Surface Acoustic Wave (SAW) [8], and Film Bulk Acoustic resonators (FBAR) [9] have all previously been utilized for sensory applications. Such devices can quantify the cumulative mass deposited on their surfaces as a shift in their resonant frequency.

A Quartz Crystal Microbalance (QCM) consists of a thin piezoelectric plate with electrodes evaporated onto both sides. Due to the piezoelectric effect, appliance of an AC voltage across the electrodes causes the structure to vibrate at a certain frequency. A QCM is used to measure a mass per unit area by recording the change in frequency of a quartz crystal resonator. The resonance varies by the addition or removal of a small mass at the surface of the acoustic resonator. An FBAR consists of a piezoelectric material sandwiched between two electrodes and acoustically isolated from the surrounding medium. FBAR devices resonate in the frequency range of roughly 100 MHz to 10 GHz. A SAW resonator consists of a piezoelectric substrate with two or more inter-digitated low-density metal electrodes and potentially two acoustic reflectors patterned on top of the piezoelectric material. The mass sensing principle of both the FBAR and the SAW resonator are similar to that of the QCM.

Several efforts have been carried out to come up with new miniaturized piezoelectric resonator structures on silicon substrates. Piazza et. al. [11-13] presented a

new class of aluminum nitride (AlN) piezoelectric resonators that have their fundamental frequency defined by in-plane dimensions. For this reason the devices were called contour-mode resonators. The use of contour modes allowed the batch fabrication of arrays of piezoelectric microresonators with different frequencies on a single chip. These devices mostly were realized in the form of rectangular plates. The other class of microscale piezoelectric resonators that developed in parallel with the monolithic AlN counter mode resonators is the counter mode piezoelectric on silicon counter mode resonators [14, 15]. In this structure, piezoelectric material is used for transduction of silicon body of the resonator. Recently the same structure has been used however, by using diamond rather than silicon as the resonating material higher quality factors has been achieved at higher frequencies [16].

1.3.2 Capacitive Transduction

Capacitive or electrostatic transduction is another mechanism widely used for micromechanical resonators transduction. Assuming a parallel plate capacitor, by applying a voltage across the plates, the accumulated opposite charges on both surfaces apply an attracting force to each other, leading to the two plates attracting each other. The resulting force (F), as shown in equation 1.6, depends on the gap size (d) between the two parallel plate capacitors, plate area (A) and the applied voltage (V) across the plates.

$$F = \frac{V^2 \varepsilon_0 A}{2d^2} \tag{1.6}$$

By applying an alternating voltage across the plates, the periodic mechanical force can be used to actuate a micromechanical resonator. On the other hand, in order to sense the vibration amplitude of a resonator, the same parallel plate capacitor can be utilized. By

connecting the parallel plate capacitor to a constant DC voltage, if somehow the distance between the plates changes, there is going to be a change in capacitance of the capacitor. This causes a transient current to be generated that can be measured. In a vibrating resonator, the mechanical vibration can modulate the gap size and therefore, produce an alternating output current.

Figure 1.4 shows the schematic view of a disk resonator which upon actuation vibrates in its in-plane counter resonance mode. The disk in the middle is hovering on top of the substrate and therefore upon actuation it freely vibrates. If an AC voltage which has a frequency equal to the resonance frequency of the device is applied to the input (actuation) electrode, it will be actuated. Due to the constant DC voltage present between the disk and the right-side electrode during resonance, the vibration amplitude will be modulated by an alternating output current which can b sensed.

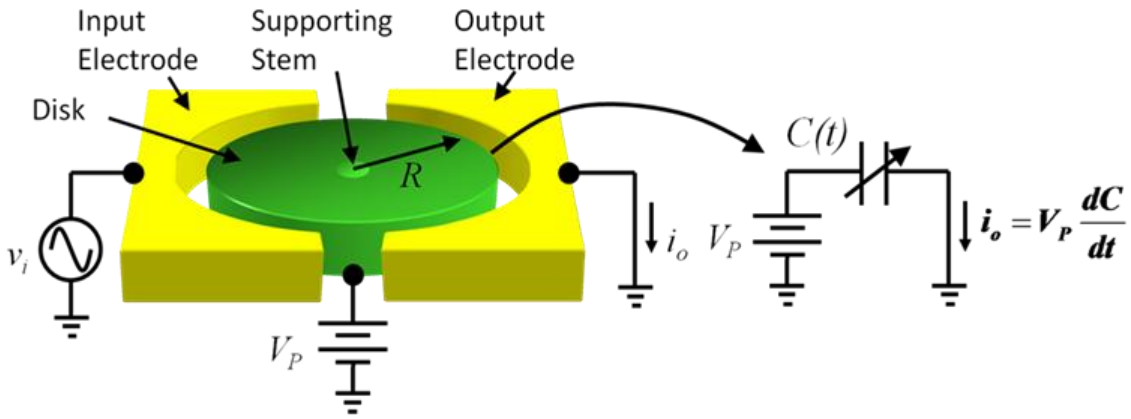

Figure 1.2. A schematic view of a counter mode electrostatic disk resonator. the left and right side electrodes are being used for actuation and sensing of the resonator respectively [27].

In order to achieve a strong enough electromechanical transduction and consequently a large signal to noise ratio, capacitive resonators require relatively large electrode areas (thousands of μm^2) consuming costly real-estate on the chip and limiting

the maximum number of devices that can be integrated on a single chip and besides that, large capacitive values themselves could become problematic.

1.3.3 Thermal Actuation with Piezoresistive Readout

When current passes though a conductor, the large electrical resistance present in the structure, causes it to dissipate energy. Dissipation of energy leads to elevation of its temperature and the resulting increase in temperature causes a thermal expansion of the structure as follows:

$$\Delta L=\alpha L\Delta T \tag{1.7}$$

where L and T are the length and temperature of the structure, and α is the thermal expansion coefficient which depends on the physical attributions of the utilized material. Thermal expansion of the structure leads to an internal stress and therefore can be used as an actuation mechanism for generating force and displacement. On the other hand, as a resonator vibrates, the resistance of the resonator also changes due to the piezo-resistive effect. In metals changes in the geometry of the resonator due to mechanical stress, cause changes in electrical resistance ($R = \rho\frac{L}{A}$), where R is resistance, L is length, A is area and ρ is resistivity. The piezoresistive effect which happens in semiconductors, describes a change in both geometry as well as the electrical resistivity of a semiconductor when mechanical stress is applied. This effect has up to a few orders of magnitude higher effect than that of the involved mechanism in metals. This is due to the fact that in semiconductors, stress variation cause changes in the band structure and therefore their electrical resistance [2]. The change in resistance due to the piezoresistive effect depends on the applied stress to the structure and can be shown as follows:

$$\Delta R=R\pi_i\Delta L \tag{1.8}$$

where R, π_l and L are the resistance, longitudinal piezoresistive coefficient and length of the structure respectively.

Recent studies and experiments have shown promising results and plenty of unexplored potentials for thermally actuated high frequency resonators [1]. Both modeling and experimental measurements suggest that as opposed to the electrostatic and piezoelectric resonators, thermal-piezoresistive resonators perform better as their size is shrunk down. All of the mentioned means that they could be a much stronger candidate for realization of highly integrated nanomechanical signal processing arrays.

2. THERMALLY ACTUATED MICROMECHANICAL RESONATORS FOR AIRBORNE PARTICLE MASS SENSING

In this chapter thermally actuated micromechanical resonant devices with frequencies in the hundreds of kHz to a few MHz are presented. Their suitability and robustness for airborne particle cumulative mass measurements are demonstrated.

2.1 Resonator Structure

The goal for the sensors targeted in this project was to measure the mass of every single particle added to the resonator. Therefore, it is desired to maintain a consistent mass sensitivity all over the resonator surface so that the mass of each particle can be determined with high precision independent of the location on the resonator where it has landed. Furthermore, even for cumulative mass measurement of the particles, the mass distribution of the particles could be uneven over the resonator surface resulting in the same uncertainty.

Resonant frequency of a mechanical resonator is given by:

$$f = \frac{1}{2\pi}\sqrt{\frac{k}{m}} \tag{2.1}$$

where k and m are the effective stiffness and effective mass of the resonator in the specific resonant mode of interest.

The shift in resonant frequency (Δf) of the resonator resulting from a small added mass (Δm) can be calculated as:

$$\frac{\Delta f}{\Delta m} = -\frac{f}{2m} \Rightarrow \frac{\Delta f}{f} = -\frac{\Delta m}{2m} \tag{2.2}$$

However, it should be noted that the overall effective mass of a resonator at each location is a function of the vibration amplitude of the structure at that specific location. This could be explained by the fact that the overall energy stored and released in the resonator is the same independent of which location on the resonator body is taken as the reference point. Stored energy in the resonator in each cycle is given by:

$$E_p = \frac{1}{2} k x^2 \tag{2.3}$$

where x is the vibration amplitude at a specific point on the resonating body and k is the effective stiffness of the resonator at that point. Therefore, if the vibration amplitude of the resonator at some point on its body is smaller than another point by a factor "a", the effective stiffness at that point has to be "a^2" times larger to result in the same stored energy for the resonator. As a result, the effective mass at that point should also be "a^2" times larger to maintain the same resonant frequency. Hence, particles added to the resonator structure at different locations with different vibration amplitudes will experience different effective mass for the resonator and therefore, the frequency shift they induce in the resonator will be different.

To avoid the abovementioned problem and get a uniform mass sensitivity all over the resonator surface (or a big portion of it), the resonator structure shown in Figure 2.1 was initially used for cumulative mass sensing of airborne particles. The resonator is

comprised of a central square-shaped mass and four support beams connected to its four corners. Such structure has several mechanical resonant modes, but the mode of interest which is more suitable for the targeted application in this work is the fundamental in-plane resonant mode. Two of the support beams are split into two unequal branches at their clamping point and the two branches are connected to two electrically isolated pads. The narrower branches are used for thermal actuation of the structure by passing an electrical current through them. The thermal actuators embedded in the resonator structures generate in-plane forces and are suitable for actuation of the fundamental in-plane mode. In chapter 3 we demonstrate another resonator structure referred to as I-Shaped Bulk Acoustic Resonators (IBARs; also known as dog-bone resonators). The IBAR resonators are much smaller and more sensitive than the structures shown in Fig 2.1 and they were used for individual airborne particle sensing.

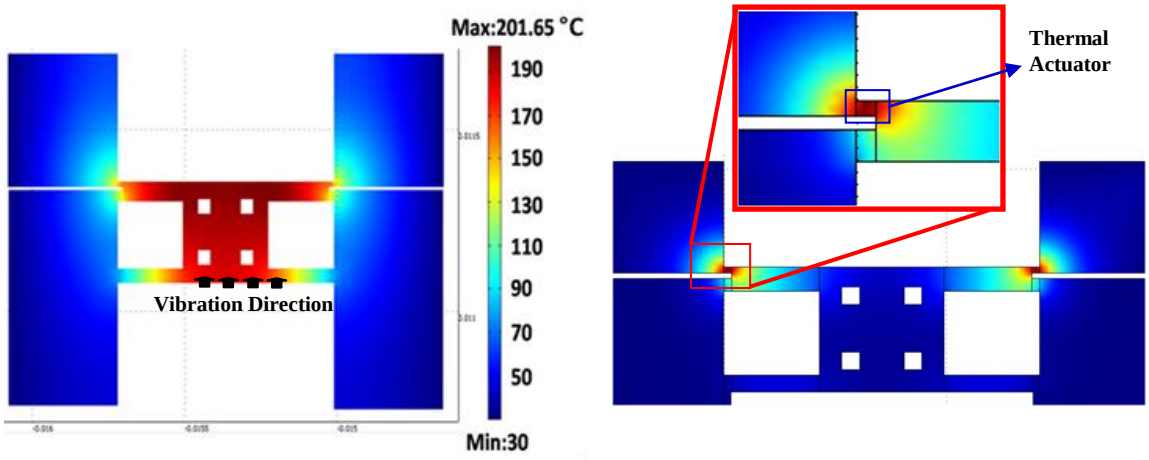

Figure 2.1. Schematic view of a thermally actuated 4-tether plate resonator showing the thermal actuator/piezoresistive sensor beams embedded in the resonator supports at the clamping points. The colors show the qualitative distribution of AC temperature fluctuation

Figure 2.2a shows the fundamental in-plane resonant mode shape of a 15μm thick 688kHz resonator while Figure 2.2b shows the in-plane extensional resonant mode of a

60MHz I-shaped resonator. For the first structure, the masses on the two ends of the pillars vibrate back and forth in opposite directions. At resonance, the resistance of the pillars will be modulated by the resulting alternating mechanical stress due to the piezoresistive effect that results in a detectable small signal motional current in the device. An engineering, design, and finite element analysis software environment called 3D COMSOL [17] which *is* used for the modeling and simulation of any physics-base structure was used to derive the fundamental in-plane mode shapes through Eigen frequency analysis. In simple terms eigen frequency analysis uses eigenvector calculations to determine the natural frequencies (or eigenfrequencies) of vibration for a structure, and the eigenvectors determine the shapes of the vibrational modes.

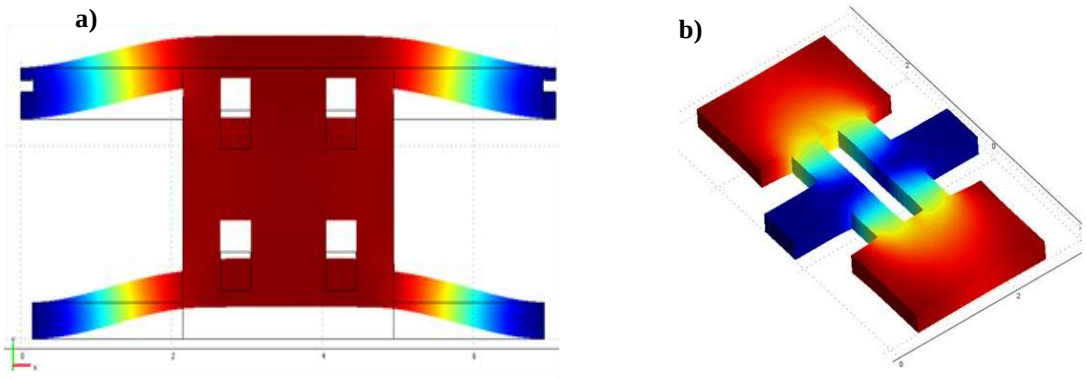

Figure 2.2. Angles view and top view of the COMSOL Eigen frequency analysis results showing the fundamental in-plane resonance mode shape for a) a 4-tether plate resonator with a resonant frequency of 688kHz. and b) I-shaped thermally actuated resonator with a frequency of 60.1MHz. Solid lines represent the unformed shape and the color code on the deformed structure represents the relative displacement in different parts of the resonator with the dark blue and red showing zero and maximum displacements respectively.

Since the in-plane stiffness of the central plate is orders of magnitude larger than that of the support beams, its deflections in the in-plane resonance mode are negligible resulting in the whole plate to vibrate with uniform vibration amplitude. Therefore, the effect of similar particles added to different locations on the plate, on the overall resonance frequency of the structure will be the same (uniformity of mass sensitivity).

This is not the case for the support beams, i.e. particles sitting on different locations of the beams will have different effects on the resonance frequency of the structure (due to different vibration amplitudes and therefore different effective stiffness and effective resonator mass at different locations). However, since the overall surface area of the support beams are typically much smaller than that of the plate, this effect could be negligible. To further increase the precision of measurements one can add a shadowing stationary surface covering the support beams.

In order to examine the uniformity of mass sensitivity on the resonating plate, a cubic 5x5x5μm^3 particle was placed on different locations on the plate in the COMSOL model and the resulting frequency shifts were calculated. Density of 1230Kg/m^3 and Young's modulus of 2.9GPa were assigned to the particle. The particle was placed in six different locations on top of the resonating plate. Figure 2.3 shows the six particle locations and the resulting frequency shift in each case. As expected, the frequency shifts for the particles in different locations are very close with a variation of only 0.6Hz and the average value of ~18.2 Hz.

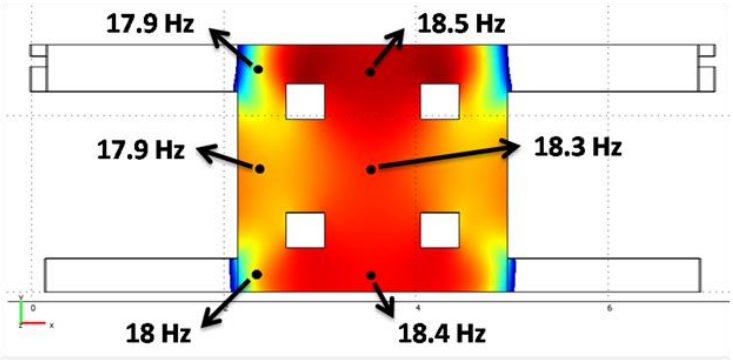

Figure 2.3. Frequency shift induced in the fundamental in-plane resonant mode of the plate resonator of Fig. 2.2 resulting from addition of a 5x5x5μm particle in six different locations on the plate showing almost the same frequency shift independent of the location of the particle on the plate. The color code shows slight differences between vibration amplitude of different locations on the plate that justifies the slight differences between different frequency shifts (higher amplitude → larger shift). The added particle has density of 1230Kg/m3 and Young's modulus of 2.9GPa.

This translates to a variation in the frequency shift of ~3.3% that could be due to the simulation inaccuracies or slight differences in the vibration amplitudes at different locations on the plate.

The theoretically calculated frequency shift resulting from the added mass of such particle, based on the resonator effective mass, was found to be 17.8Hz which is in good agreement with the average value of 18.2Hz provided by COMSOL finite element analysis. From this analysis it is understood that the frequency shifts due to the addition of mass at different locations on the surface of the plate is approximately the same, therefore proving the concept of uniform sensitivity.

The other motivation for choosing the in-plane plate resonators is that for measurement of air-borne particles, the resonators have to operate under atmospheric pressure or low vacuum (50-100Torr). Therefore, it is highly desirable to minimize the effect of air viscous damping on the resonators to maintain a high quality factor in air. In the in-plane resonant mode, only the small areas on the edges of the resonator move perpendicular to the interface with surrounding air while most of the resonator overall surface (horizontal surfaces) only slides parallel to the surrounding air interface. This helps significantly reduce air damping and therefore relatively large quality factors are expected for such devices even under atmospheric pressure.

2.2 Resonator Fabrication

A single mask microfabrication process was used to fabricate the resonators on a low resistivity P-type Silicon on Insulator (SOI) substrate with device layer thickness of 15μm and buried oxide layer (BOX) thickness of 5μm. Figure 2.4 shows the fabrication

process that starts by growing a thin (~200nm) layer of thermal silicon dioxide on the substrate (blue layer in Fig 2.4). By using photolithography, the silicon dioxide layer is patterned to define the resonator structures. The silicon structures are then carved into the SOI device layer by deep reactive ion etching (DRIE) of silicon all the way down to the buffer oxide layer. Finally, a 35 minute dip in 49% hydrofluoric acid (HF) is performed to release the resonant structures (in the middle of Fig 2.4) by etching the underlying BOX layer. At the same time the remaining oxide mask on top of the structures is also etched away.

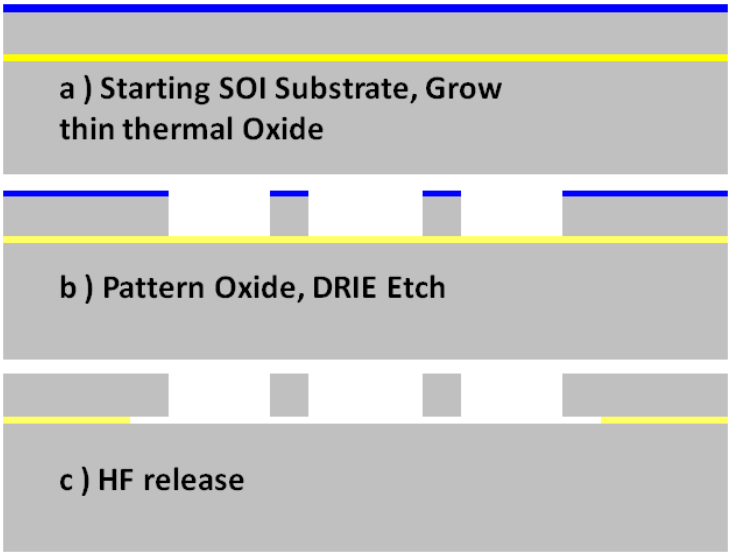

Figure 2.4. Schematic cross-sectional view of the process flow used for fabrication of the resonators on SOI substrates.

The result will be suspended single crystalline silicon resonant structures with integrated thermal actuator/ piezoresistive sensors. SEM view of two of the fabricated resonators with plate dimensions of 560 and 280 μm and support length of 85μm are shown in Figure 2.5.

Depending on the size of the resonating plate, a number of release holes have been etched into each plate to minimize release time in HF and avoid excessive undercut of the wire-bond pads.

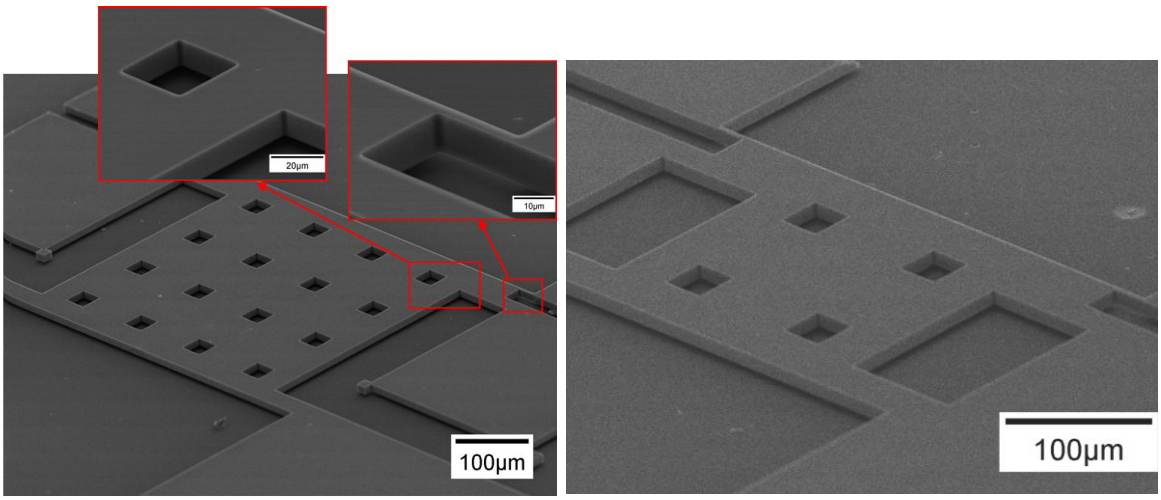

Figure 2.5. SEM view of two fabricated thermal-piezoresistive resonators with sensing platform square size of 560 and 280μm and support length of 80 μm. The narrow actuator beam is 32 μm long and 5μm wide.

2.3 Device Characterization

Since the fabricated resonators have monolithic low resistivity silicon structures and therefore there is no electrical isolation between the two actuators embedded in each resonator, they cannot be tested in a two-port configuration. Hence, to characterize the resonators, they were tested in a one-port configuration with the two thin beams acting simultaneously as both thermal actuators and piezoresistive sensors. It should be noted that in this case the device motional current (resulting from resonance) should be extracted from the overall current passing through the resonator that includes a relatively strong resistive feed-through current on top of the resonance current. This was done by post-processing of the measured data using a MATLAB code subtracting the large feed-through signal from the measured data. This analysis could have be done manually,

however there were a lot of data points for which the calculations should have been made and therefore MATLAB was used.

In order to generate an actuation force at the input signal frequency, a combination of DC and AC current components were applied between the two pads connected to the thermal actuators on the two sides of the structures. The silicon chip containing the resonators was placed on a printed circuit board (PCB) containing the required resistors and capacitors for AC and DC isolation. Figure 2.6 shows the circuit configuration used to test the resonators. Bias resistors with value of 100Ω and 0.1μF isolation capacitors were used for biasing and isolation. The actuation voltage amplitude used in all measurements (v_{in}) was 1V.

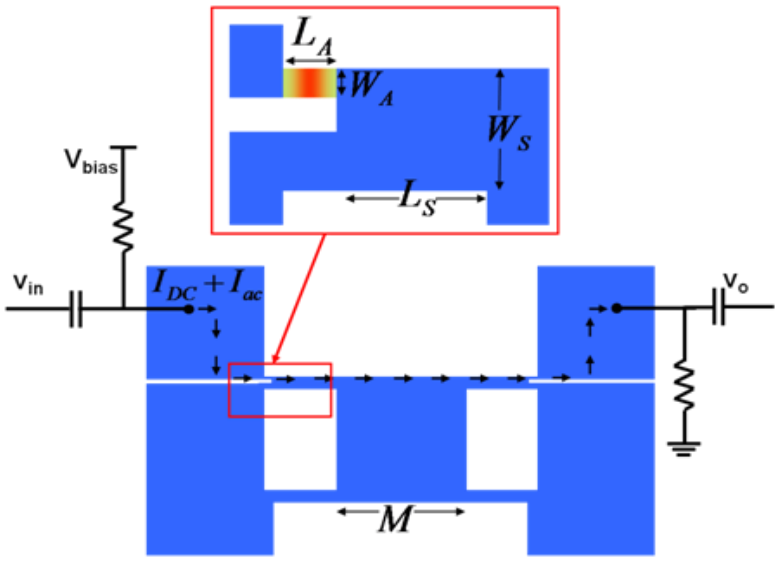

Figure 2.6. Schematic diagram of the electrical connections to the resonators for one-port operation and measurement.

Electrical connections to the resonators were provided by wedge-bonded aluminum wires. The PCB was then placed in a vacuum chamber with electrical feedthroughs. Extensive measurements were performed on several devices with different dimensions to investigate parameters of interest including resonant frequency, quality factor and

motional conductance (g_m). These parameters were measured at different bias currents both under vacuum and atmospheric pressure.

Table 2.1 presents the measured data. Three different sets of data are provided for each resonator.

Table 2-1 Measurement and calculation results for resonators with different dimensions.

Resonator Dimensions (µm)			**Applied Parameters**		**Measured Parameters**		
Plate size	L_A W_A	L_S W_S	I_{DC} **(mA)**	**Vac./Air**	***Q.* Factor**	**Freq. (MHz)**	g_m **(mA/V)**
280	32 5	80 70	24	Vac.	11000	1.4144	0.621
			43	Vac.	8200	1.4125	1.52
			55	Air	3300	1.4119	0.771
280	32 5	160 70	25	Vac.	17700	0.83509	5.45
			50	Vac.	13300	0.83052	18.0
			54	Air	4200	0.83197	6.41
280	32 5	200 70	25	Vac.	10500	0.67707	4.03
			54	Vac.	6700	0.6696	11.9
			55	Air	2000	0.67438	3.35
560	32 5	160 70	25	Vac.	9300	0.43839	5.66
			55	Vac.	6000	0.43274	15.9
			55	Air	3200	0.43721	9.27
280	17 15	197 55	48	Vac.	14500	0.65141	27.6
			60	Vac.	14500	0.64972	43.3
			60	Air	4200	0.65116	11.1
280	17 15	400 55	15	Vac.	18000	0.269	7.51
			48	Vac.	13200	0.26396	69.5
			57	Air	3000	0.26618	18.4
560	17 15	200 55	35	Vac.	20000	0.34915	33.9
			61	Vac.	15300	0.34345	102

The first row is associated with the bias current at which the highest quality factor value has been measured for the resonator under vacuum. The second row includes measurement data under vacuum with the bias current at which the highest transmission (highest motional conductance) has been measured. Motional conductance is defined as

the ratio of the output current to the actuation voltage and therefore a higher motional conductance value means it will be easier for the device to be integrated as an electrical component. The third row of data has been collected from the resonator operating under atmospheric pressure at its highest transmission level.

Figures 2.7 (a) and (b) show different frequency response plots for an 830kHz resonator at different bias currents under both vacuum and atmospheric pressure respectively. The vertical axis defines the values of motional conductance in decibels.

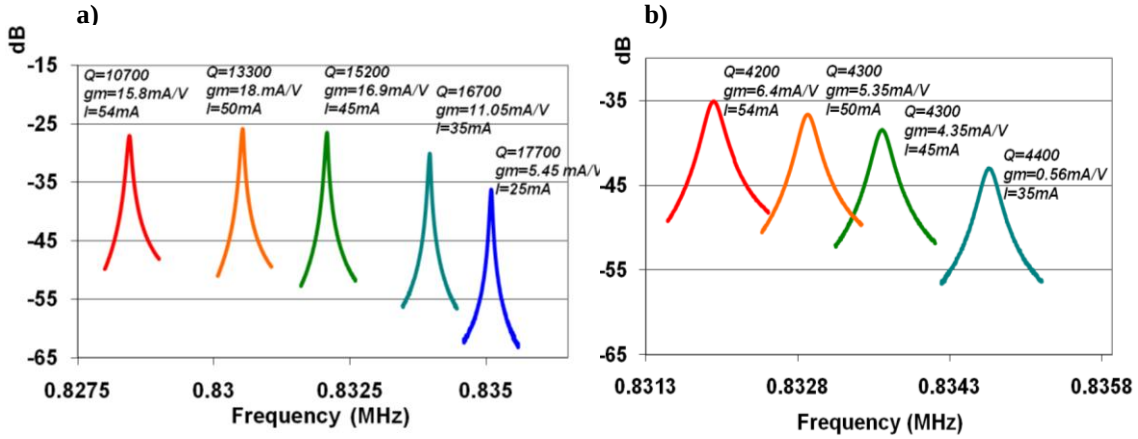

Figure 2.7. Measured frequency responses for a thermally actuated resonator with different bias currents. a) Figure on the left shows the results in vacuum while b) Figure on the right represents the results measured in air. The resonating device and support dimensions are 280 μm and 190 μm, while the actuating beam has length and width dimensions of 32 μm and 5 μm respectively.

Equivalent motional conductance as high as 18mA/V have been extracted for this resonator which is more than enough to be able to use such device as an electronic component. As expected, by increasing the DC bias current the motional current level (which is resulting current from resonance) increases while the resonator frequency decreases due to the higher static temperature and softening of the structural material. The measured resonance frequencies for resonators with different dimensions obey the expected trend, i.e. for similar support sizes, larger masses result in lower frequencies and

for similar mass sizes, shorter supports result in higher flexural stiffness of the support beams and therefore higher resonance frequencies.

As shown in Figure 2.8, a general trend of reduction in the quality factor is observed as the bias currents increase. Since the air viscous damping becomes the dominant loss mechanism when operating the resonators under atmospheric pressure, the effect of temperature induced loss becomes much less pronounced.

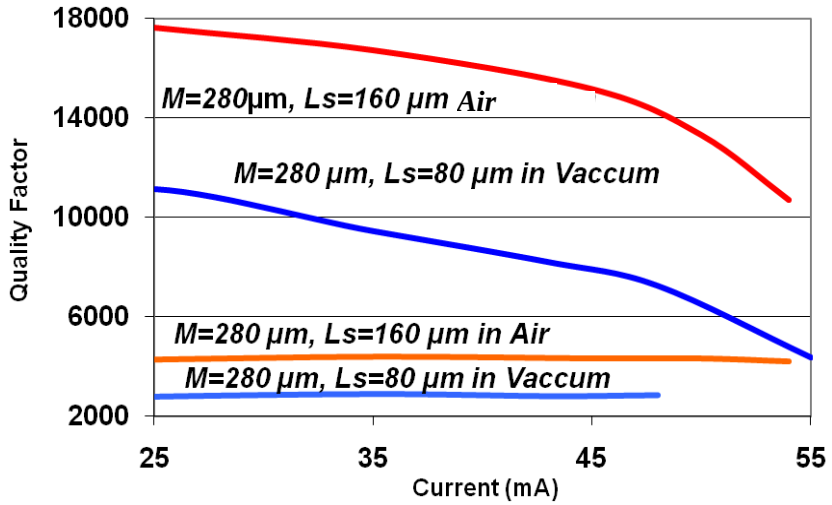

Figure 2.8. Measured quality factors for two thermally actuated plate resonators versus the applied bias current. The resonators have resonating mass and support lengths of 280-160µm and 280-80µm respectively. Each device was tested in both vacuum and air.

One of interesting and highly desirable characteristics of the resonator structures used in this work is that, as expected and discussed in section 2.1, they maintain relatively high quality factors in the order of a 2000-4500 in air. Quality factors of capacitive beam resonators with such low frequencies typically drop to 100 or less in air [11-12]. This makes such resonators particularly suitable for environmental sensory applications.

2.4 Mass Sensitivity Characterization

In order to measure the mass sensitivity of the fabricated resonators, aerosol particles with known size and composition were generated and deposited on the resonators while monitoring their frequency shift. Figure 2.9 shows the schematic diagram of the aerosol particle generator used for this purpose.

The system includes a micro syringe pump that was filled with a solution of methylene blue in ethanol (50mg/L). The flow of liquid coming out of the micro syringe is first turned into small droplets (atomized) by a perpendicular flow of nitrogen gas. The droplets are passed through a Kr-85 bipolar diffusion charger that neutralizes most of the charge left on the particles as a result of atomization and establishes a charge distribution close to Boltzman distribution for the droplets (mostly neutral, some±1e, less ±2e, etc.).

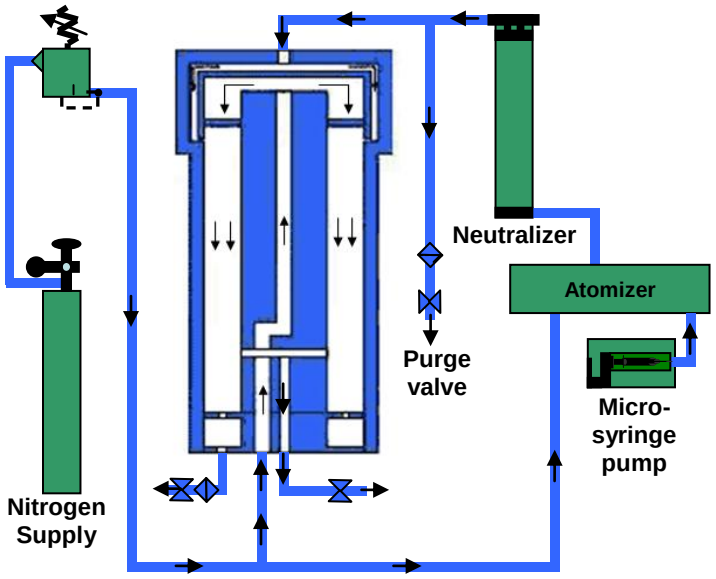

Figure 2.9. Schematic diagram of the aerosol particle generator. Dried aerosol is injected into the differential mobility analyzer (the central column) that permits selection of only particles with specific diameters based on its adjusted voltage and flows.

In the meantime the solvent in the droplets is evaporated and the dried aerosol is injected into a differential mobility analyzer that separates the particles using an electrostatic field (based on their size and electric charge) allowing only particles with specific mass to charge ratio to pass through it.

In this experiment, the voltage and flows were regulated to permit selection of particles having a diameter near 1 micron. The particles were then directed into a low pressure chamber comprised of a bell-jar, placed and sealed on a metallic plate with electrical and air feed-throughs. One of the air inlets was connected to a small vacuum pump generating a pressure of ~60-80 Torr. The flow of particles was connected to the other inlet of the chamber and the particles were deposited on the sensors through a nozzle embedded in a microscope (Figure 2.10) with one of the objective lenses of the microscope replaced by the nozzle. The particles are deposited onto the MEMS sensor by impaction. The aerosol is accelerated by passing through the orifice nozzle and the resulting jet strikes the specific resonator. The particles have sufficient inertia to strike the resonator and they stick there.

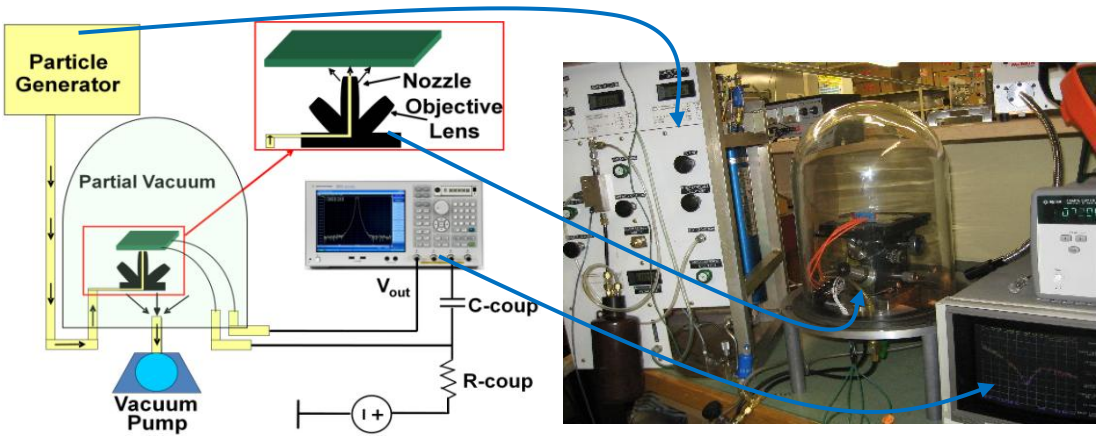

Figure 2.10. Schematic view and camera picture of the setup used to characterize the resonator mass sensitivities. The aerosol jet was positioned over the sensor using a modified microscope with an integrated nozzle and a micro-positioning stage.

The microscope is used to align the beam of particles to the resonator under test which is mounted on a micro-positioning stage. The alignment is performed by looking at the resonator sample through the microscope and aligning the sample so that the resonator under test is in the middle of the view. The objective platform is then turned to switch to the nozzle without changing the position of the sample. As a result, the nozzle will be positioned exactly on top of the resonator under test.

Resonators with different dimensions were exposed to the flow of particles for several consecutive intervals of a few minutes each. After each interval the resonator characteristics were measured and recorded. Figure 2.11 shows the measured change in the resonance frequency versus the overall exposure time of a resonator with a square size of 280μm and support length of 400μm which has a frequency of 266 kHz. The narrow actuator beam is 17μm long and 15μm wide. It is clear that as more particles are deposited on the resonator, its resonant frequency decreases almost linearly over time.

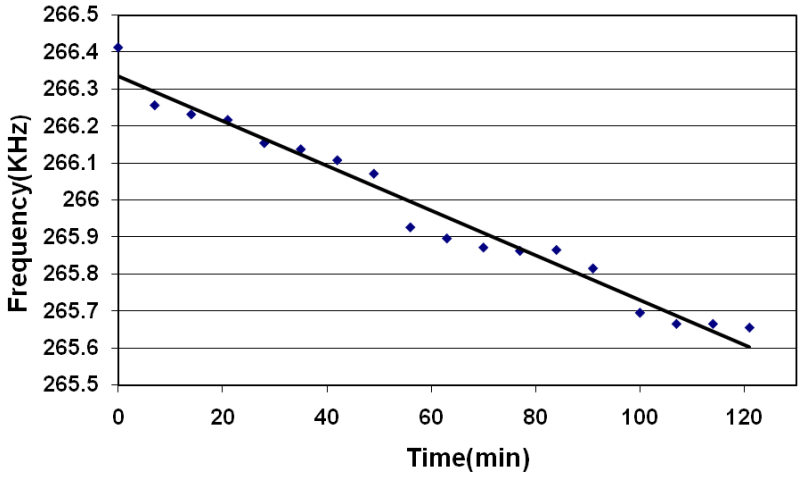

Figure 2.11. Change in the measured resonance frequency for a 266KHz resonator as a function of the overall exposure time showing an overall frequency shift of ~760Hz (0.29%).

Figure 2.12 shows different frequency response plots for the same resonator biased at a constant current of 30mA for an overall exposure time of 120 minutes. It should be noted that the resonator quality factors are surprisingly robust to the deposited particles and even after deposition of thousands of particles, no significant Q degradation is observed. This robustness is mainly attributed to the thermal-piezoresistive nature of the resonators. An air gap capacitive resonator could not have survived such particle bombardment over such long period as one single particle entering the transduction gaps could have completely made the resonator nonoperational.

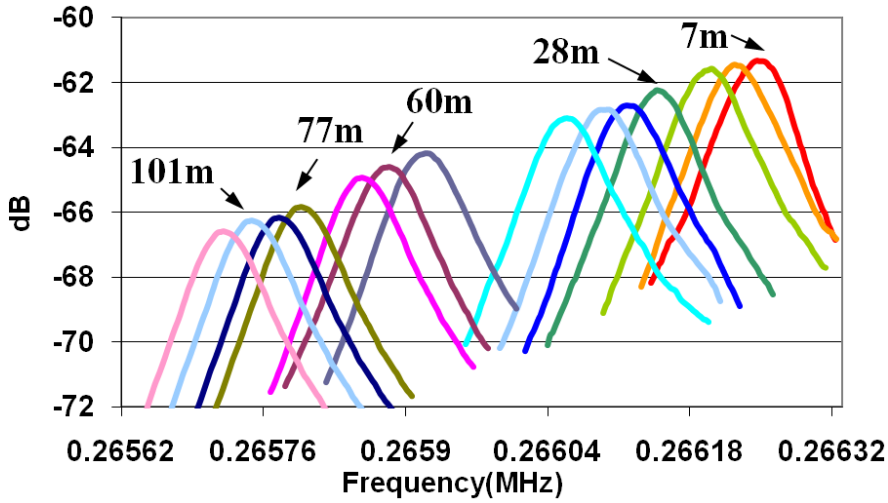

Figure 2.12. Measured frequency responses for the 266KHz resonator after several consecutive steps of particle deposition.

The added mass of the particles is expected to reduce the resonant frequency according to equation 2.1. Knowing the dimensions and therefore the mass of the resonators, the mass of the deposited particles were estimated from the measured frequency shifts (Table 2.2). Independently, the number of deposited particles was estimated by SEM inspections after deposition (Figure 2.13). Partial counting and

estimation methods were used to determine the approximate number of deposited particles. The overall particle mass was then calculated using:

$$\Delta m = \frac{N\rho\pi\, d^3}{6} \tag{2.9}$$

where N is the number of particles, ρ is the particle density and *d* is the particle diameter.

As shown in Table 2.2, comparison of the theoretically calculated and practically estimated masses shows an acceptable agreement between the two. Resonator mass sensitivities are in the 50-300 Hz/ng range and as expected are higher for higher frequency devices. Orders of magnitude higher mass sensitivities can be achieved by further shrinking the size of the resonators.

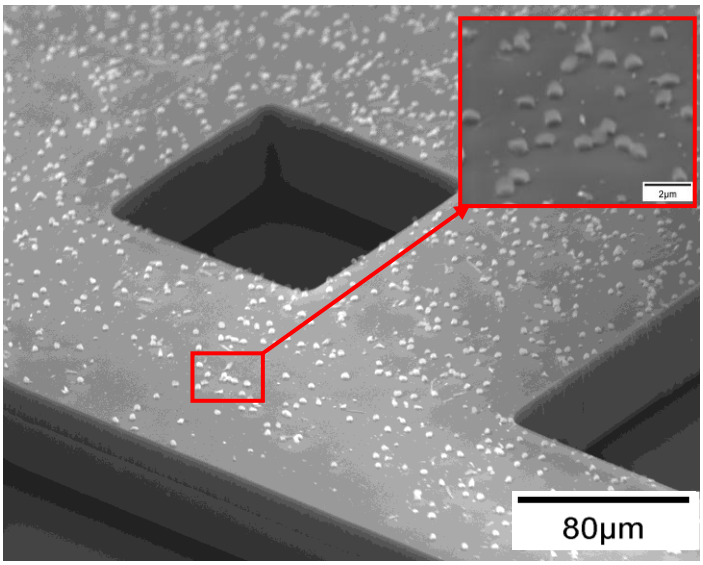

Figure 2.13. SEM view of part of a resonator after deposition of ~1µm diameter particles.

Table 2-2 Summary of measurement results obtained from different resonators.

Resonator and Support(*Ls/Ws*) Dimension (μm)	Freq. (kHz)	*Q.* Factor	Time (min)	Freq. Shift (Hz)* %	*ΔM* from Calc. (ng)	*ΔM* from Particle Counts (ng) ~ # Particles	S_{Theory} (Hz/ng)	S_{meas} (Hz/ng)
280 - 85 / 55	1781.31	760	0	-475 0.026%	1.45	1.7 2,800	327	280
	1781.26	870	20					
	1781.08	730	30					
	1780.83	990	45					
280 - 200 / 55	665.683	2220	0	-390 0.059%	3.46	3.4 5,300	112	115
	665.458	2280	15					
	665.354	2340	30					
	665.294	2220	45					
280 - 400 / 55	266.413	3050	0	-760 0.29%	19	14.9 23,000	40	51
	266.154	2890	28					
	265.926	2880	56					
	265.815	2480	91					
	265.655	2480	121					
*: The frequency shift values are in accordance to overall particle deposition time of 45, 45 and 121 minutes								

Using the Allan-variance method [12], frequency measurement accuracies in the sub-0.01 Hz have been measured and reported for thermally actuated resonators with similar frequencies and quality factors in [13].

Assuming temperature uncertainty of 10ºC (which is typical in targeted environmental applications) and temperature coefficient of frequency (TCF) of -40ppm/ºC, which is typical for uncompensated silicon resonators, the frequency of a 1.7MHz resonator could shift by up to 680Hz due to temperature. This limits the mass resolution to ~2.3ng. TCF as low as -0.05ppm/ºC has been achieved for compensated version of thermally actuated silicon resonators [14] reducing the temperature induced frequency inaccuracy of the same 1.7MHz resonator to 34Hz. This translates into a mass resolution of ~115pg. Minimum detectable mass limits in the pico-gram range for FBARs [9,15] and in the tens of pico-gram range [7,8,16-18] for QCM and SAW resonators have been reported. However such estimates generally neglect the effect of temperature induced frequency uncertainties.

2.5 Air-Borne Particle Mass Density Measurement

After characterization of the resonator mass sensitivities and their performance as particle mass sensors with artificially generated particles, a number of the resonators were used to measure the concentration of air-borne particles in a regular air sample from the surrounding lab environment.

In this experiment the PCB was placed in the same low pressure (~60-80 Torr) chamber with one of the feed-throughs connected to a small vacuum pump. The other air inlet, internally connected to the particle deposition nozzle, was left open allowing the air from outside (along with the particles suspended in it) to be sucked into the chamber. The air and airborne particles are directed and accelerated at the narrow opening at the end of the nozzle towards the resonator. A valve was also connected to the air inlet to allow turning the particle flow on and off. With the inlet valve closed, under a constant bias current, the main parameters of interest including the resonance frequency, quality factor and resonator equivalent resistance at resonance (motional resistance) were recorded.

The inlet valve was then opened exposing the resonator under test to the air flow and consequently the aerosol particles. The exposure was done in 10 second intervals and after each exposure the resonator parameters were measured and recorded.

Similar set of measurements were performed on different resonators with different dimensions. As expected, as a result of the added mass of the absorbed particles to the resonating body of the devices, the resonant frequency of the resonators was reduced after each exposure step. The absorbed mass (Δm) can similarly be calculated based on

the measured frequency shift (Δf) and mass of the resonator itself (m) as previously shown in equation 2.1.

Figure 2.14 shows the SEM view of the resonator of Fig. 2.5b after it was exposed to the aerosol particles in the atmosphere for 80s. Calculated values for deposited masses in each 10s interval was in the 100 to 1000 pg range. Figures 2.15 a and b show the change in the resonance frequency and quality factor of the resonator of Figure 2.14 versus the overall exposure time.

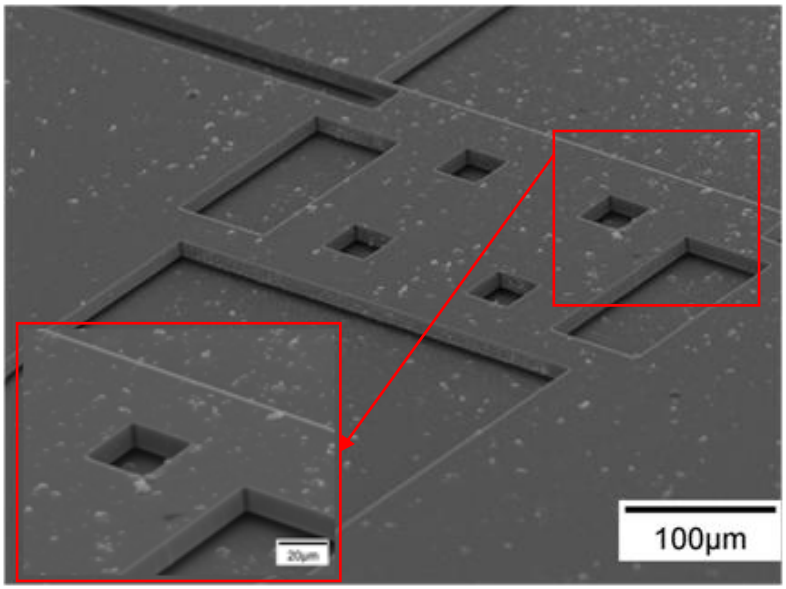

Figure 2.14. SEM view of the thermal resonator of Fig. 2.5b after exposure to aerosol particles in the atmosphere for 80s.

To calculate the particle mass density in the air sample, Equation 2.10 can be used to calculate the mass flow of the air entering the chamber (w) [18]:

$$w = 0.685\frac{Ap_0}{\sqrt{RT_0}} \quad (\frac{Kg}{s}) \tag{2.10}$$

where R is the ideal gas constant $(287\frac{J}{Kg.K})$, T_0 is the temperature in Kelvin, P_0 is the

pressure difference in Pascal and *A* is nozzle orifice area in m^2. Knowing the upstream air density (ρ), the upstream volumetric flow can be calculated ($F = \frac{w}{\rho}$).

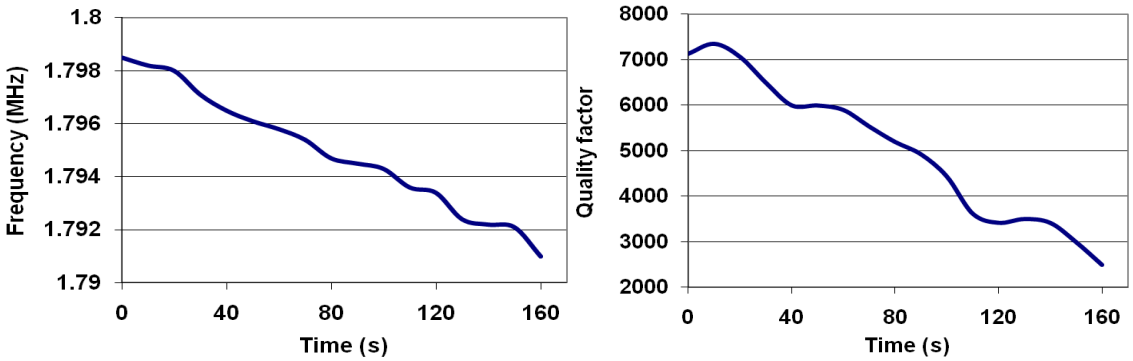

Figure 2.15. a) Change in the measured resonance frequency for the resonator of Fig. 2.14 as a function of the overall exposure time showing an overall frequency shift of over 8kHz (0.44%). b) Measured quality factors versus overall time of exposure to aerosol particles for the resonator of Fig. 2.14.

By calculating *F* and knowing the change in mass (Δm), the aerosol mass concentration can be calculated as:

$$C = \frac{\Delta m}{Ft} \tag{2.11}$$

where *t* indicates the exposure time.

Based on the measurement results and using Equations 2.10 and 2.11, value of 14.2µg/m^3 was calculated for aerosol concentration in the lab environment. According to the annual environmental protection agency (EPA) report, the average PM2.5 (particles less than $2.5\mu m$ diameter) for Denver in 2008 was ~7.35 µg/m^3 while PM10 was ~25.8µg/m^3. The calculated value based on our experiment is in the same range that confirms the experiment calculations are similar.

To summarize this chapter, thermally actuated single crystal silicon in plane resonators with piezoresistive output detection were successfully fabricated and characterized.

Frequencies in the 250kHz to 2MHz range and quality factors as high as 20,000 in vacuum and 4,400 in air were measured for the resonators, making them ideal for sensory applications. The resonators were used for the cumulative mass measurement of air-borne micro-particles. Not only did the described in-plane thermally actuated flexural resonators maintain high quality factors in air, but they were also very robust to the deposited particles and even after deposition of thousands of particles, no significant Q degradation was observed for such devices. Relatively low motional impedances in the few kΩ range obtained for the resonators is bound to make them suitable components for utilization in electronic systems. Mass sensitivities in the order of hundreds of Hz per ng were measured for such resonators that are in good agreement with the theoretically calculated mass sensitivities. Measurement of mass density of arbitrary airborne particles in the surrounding lab environment also showed a good agreement with the value indicated by the environmental protection agency.

3. INDIVIDUAL AIR-BORNE PARTICLE MASS MEASUREMNET USING HIGH FREQUENCY MICROMECHANICAL RESONATORS

3.1 Resonator Description and Fabrication

Uniform mass sensitivity is a necessity when targeting mass measurement of individual air-borne particles. Electro-thermal actuators are extremely simple to implement requiring only a heating resistance. They are also very suitable for actuation of in-plane translational resonance modes, providing uniform mass sensitivity over a big portion of the resonator surface area [24, 25]. In chapter 2, the suitability and robustness of thermally actuated micromechanical resonators for airborne particle cumulative mass measurements was demonstrated. This section presents smaller and higher frequency versions of such devices capable of detection and measurement of single submicron particles.

The resonators utilized in this work are referred to as I-Shaped Bulk Acoustic Resonators (IBARs; also known as dog-bone resonators) [25-27]. The schematic view of a thermally actuated IBAR is shown in Figure 3.1a.

Such devices are very suitable for thermal actuation as they can easily be actuated by passing a fluctuating electrical current between the two pads on their two sides. This results in an AC ohmic loss component in the current path. Due to their higher resistance, most of the ohmic loss occurs in the thin pillars located in the middle of the structure. The AC force generated in the pillars as a result of the fluctuating temperature and therefore

alternating thermal stress in the pillars, can actuate the resonator in its in-plane resonant mode.

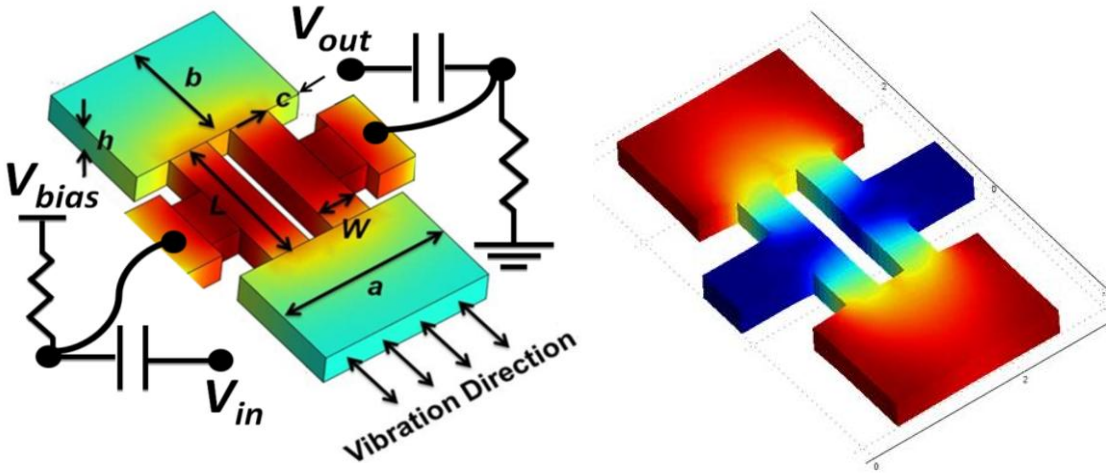

Figure 3.1. a) Schematic view of the utilized thermally actuated resonant sensors showing the qualitative distribution of AC temperature fluctuation amplitude (red being the maximum and blue the minimum). The electrical connections required for one-port operation of the resonator are also shown; b) COMSOL eigen frequency analysis results showing the fundamental in-plane resonance mode shape for an IBAR [25].

Figure 3.1a shows the qualitative distribution of AC temperature fluctuation amplitude. The electrical connections and components required for isolation of the AC actuation current from the DC bias current required for operation of the resonator [25] are also shown in Figure 3.1a. Figure 3.1b shows the in-plane extensional resonant mode of the resonators. In this mode the masses on the two ends of the pillars vibrate back and forth in opposite directions. At resonance, the resistance of the pillars will be modulated by the resulting alternating mechanical stress due to the piezoresistive effect that results in a detectable small signal motional current in the device.

The standard single mask SOI MEMS process explained in chapter 2 was also used for fabrication of the IBAR resonators mentioned here [25]. The resonators were fabricated on two different low resistivity SOI substrates: 1) a P-type SOI substrate with

device layer thickness of 15μm and buried oxide layer (BOX) thickness of 5μm, and 2) an N-type SOI substrate with both device layer and BOX thickness of 5μm respectively.

Figure 3.2 shows the SEM view of two of the fabricated IBARs which were used in the experiments. For the device on the right hand side (Fig 3.2b), the actuator beams were thinned down in order to minimize resonator power consumption. This was done by performing a number of consecutive thermal oxidation and oxide removal steps after the devices were released. At the same time, the resonator thicknesses were also reduced.

Due to the nearly rigid body of the moving plates of the resonators, their deformation in the in-plane resonance mode is negligible. Therefore, the whole plate vibrates with relatively uniform vibration amplitude. As a result, the effect of similar particles added to different locations on the plate, on the overall resonance frequency of the structure will be the same (uniformity of mass sensitivity) [24,25].

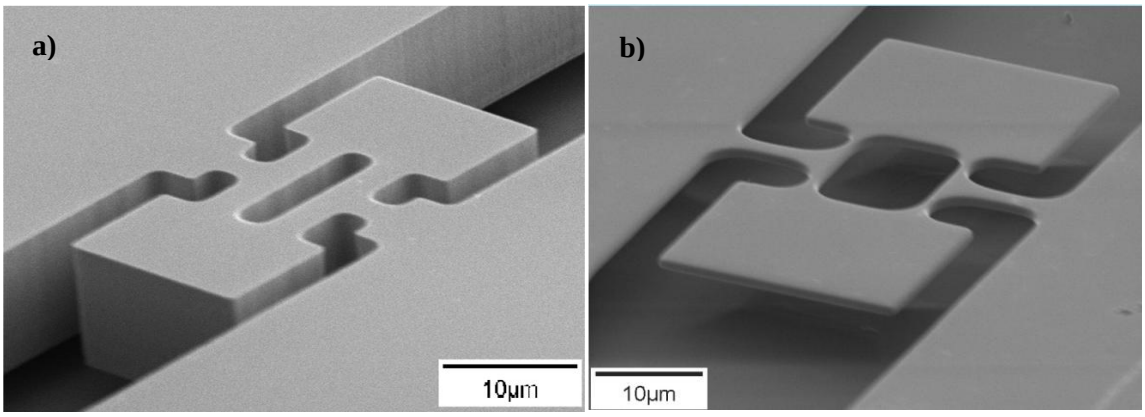

Figure 3.2. SEM views of two of the fabricated IBARs, a) a 61MHz, 15μm thick resonator, and b) a fabricated 20.5 MHz, 2.7μm thick resonator. Both resonators were etched using DRIE (ICP + Bosch process).

3.2 Resonator Mass Sensitivity and Characterization

In order to characterize mass sensitivity of the fabricated resonators, the silicon chip containing the devices was placed on a printed circuit board (PCB) containing the

required resistors and capacitors to apply DC bias and AC actuation currents to the resonators. The value of the bias resistors and isolation capacitors were 100Ω and 0.1μF respectively. Connections to the resonators were provided by wedge-bonded aluminum wires. The PCB was then embedded in the same custom made setup comprised of a sealed vacuum chamber, an aerosol particle generator, and an alignment apparatus shown in Fig 2.10. Particles coming out of the particle generator are deposited on the resonator under test. Resonators with different dimensions were exposed to the flow of particles for several consecutive intervals of a few minutes each. After each interval, the resonator characteristics were measured and recorded.

Figure 3.3 shows the resonant frequency of the 61MHz and 20MHz resonators of Figure 3.2 versus the overall exposure time after each exposure step. It is clear that reduction of the resonant frequency of the resonator is quantized and occurs in steps that are multiples of ~800Hz for the 60MHz and ~900Hz for the 20MHz resonator. This makes the effect of every single particle on the resonance frequency distinguishable.

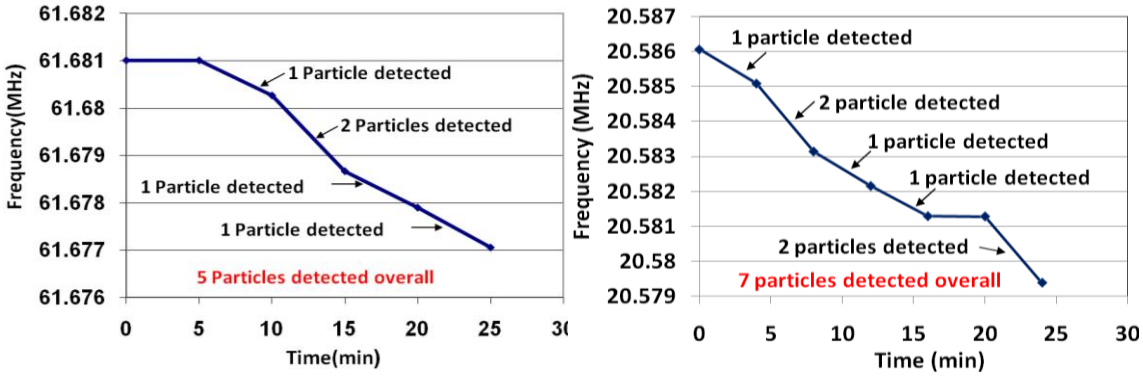

Figure 3.3. The left graph shows the measured resonance frequency for the 61MHz resonator of Fig. 3.2a as a function of the overall exposure time showing an overall frequency shift of ~4kHz (65ppm). The figure shows four consecutive reduction steps with one of the steps having a slope twice the rest showing that two particles have been deposited during that specific interval (10-15min). The right figure is showing the change in the measured resonance frequency versus time for the 20MHz resonator of Fig.3.2b showing an overall frequency shift of ~6.7kHz (325ppm). Here there are 5 frequency reduction steps, of which 2 have a slope twice that of the rest which again shows that 2 particles have been deposited on the device during that period. In conclusion, 5 particles and 7 particles have overall been deposited on the 61MHz and 20MHz resonator respectively.

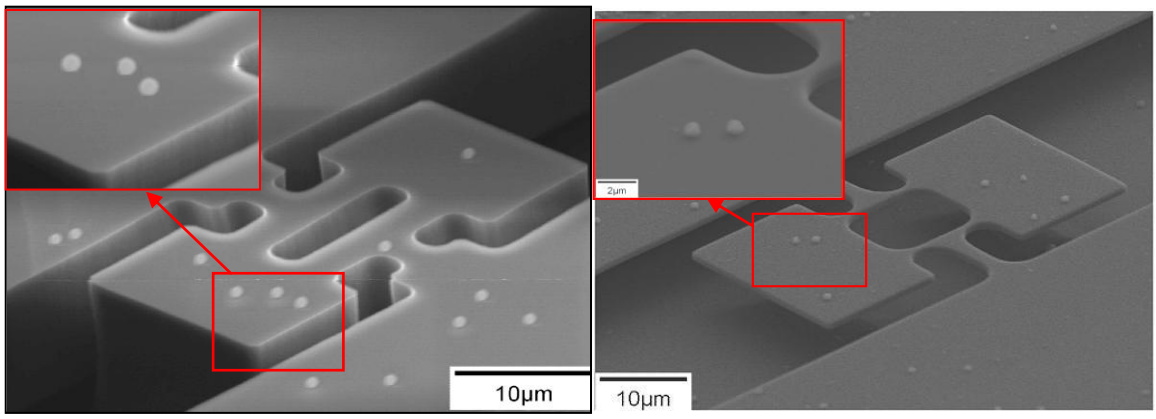

Figure 3.4. SEM view of the resonators of Fig. 3.2 after exposure to aerosol particles for 25 and 24 minutes respectively; showing 5 and 7 spherical particles deposited on their two sensing plates.

Figure 3.4 shows the SEM view of the resonators of Figure 3.2 after 25 and 24 minutes of exposure showing exactly 5 and 7 spherical particles of ~1µm diameter deposited on their two sensing plates. This is in complete agreement with the step by step frequency shifts shown in Figure 3.3.

In case of the first resonator, the particle on the thermal actuator beam has negligible effect on the resonant frequency since the vibration amplitude at that location is very small compared to the plates. Particles sitting on different locations of the thermal actuator beams will have different effects on the resonance frequency of the structure (due to different vibration amplitudes and therefore different effective stiffness and effective resonator mass at different locations). However, since the overall surface area of the thermal actuator beams are typically much smaller than that of the plates, the resulting error could be negligible. To further increase the precision of measurements one can add a shadowing stationary surface covering the thermal actuator beams.

Figure 3.5 shows different measured frequency response plots for the 61 MHz resonator of Fig. 3.2 during particle deposition. As shown in Figure 3.6 the resonator

quality factor is slightly degraded as more particles are deposited on it and that is the reason why the peak signal level decreases over time in Fig. 3.5.

The mass sensitivity of the resonators can be theoretically calculated based on the resonant frequency and effective mass of the resonator (Equation 2.2). Knowing the dimensions and therefore the effective mass of the resonators, the overall mass of the deposited particles (δm) were estimated from the measured frequency shifts (δf). The overall mass of the particles was also independently calculated based on the number of the deposited particles given by SEM inspections of Figure 3.4.

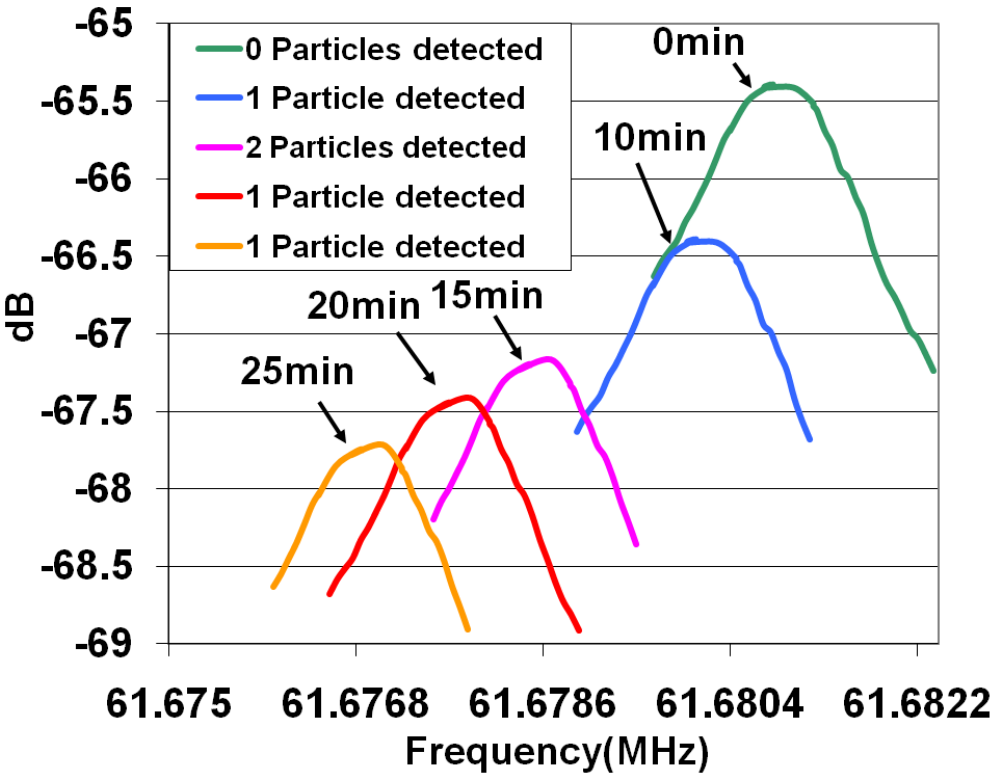

Figure 3.5. Measured frequency responses for the 61 MHz resonator of Fig. 3.2a while biased at a constant current after different exposure intervals.

Table 3.1 summarizes the measurement results for the tested resonators and compares the experimental frequency shift caused by the added mass of the particles

(~0.65pg per particle) with the expected frequency shift according to the mass of the resonator and Equation 1, showing a good agreement between the two.

Resonator mass sensitivities are in the 1.1-1.7 kHz/pg range. As expected, devices with higher frequency and smaller size have higher sensitivities. The demonstrated mass sensitivities are orders of magnitude higher than the reported values for conventional quartz [7, 16, 17], SAW [8, 28, 29], and even FBARs [9] due to their much smaller sizes.

Table 3-1 Summary of measurement results obtained from the two resonators in Fig.3.2 and comparison of the measured mass sensitivity with the theoretically predicted mass sensitivity.

Resonator Dimensions (μm)		Q factor	Freq (MHz)	Time (min)	Freq. Shift (Hz)	No. of particles detected	Overall Mass from freq. shift (pg)	Overall Mass from Microscope count (pg)	Calculated Sensitivity (kHz/pg)	Measured Sensitivity (kHz/pg)
a-b-c	L-W-h									
22-15.4-4.4	17.6-5-15	11140	61.68101	0	-	-	3.43	3.22	1.152	1.228
		11300	61.68101	5	0	0				
		11100	61.680268	10	-742	1				
		10930	61.678668	15	-1600	2				
		10890	61.677896	20	-771	1				
		10740	61.677055	25	-842	1				
30-19.7-7	15-0.8-2.7	5120	20.58606	0	-	-	4.877	4.508	1.369	1.481
		5010	20.585085	4	-975	1				
		4960	20.58314	8	-1945	2				
		4730	20.582151	12	-989	1				
		4600	20.581286	16	-865	1				
		4610	20.581279	20	-7	0				
		4350	20.579381	24	-1898	2				
29.9-20-7	14-1.9-2.7	4595	26.962981	0	-	-	2.283	2.576	1.727	1.593
		4580	26.962973	4	-8	0				
		4410	26.962049	8	-924	1				
		4340	26.960979	12	-1070	1				
		4290	26.960972	16	-7	0				
		4165	26.959944	20	-1028	1				
		4025	26.958886	24	-1058	1				

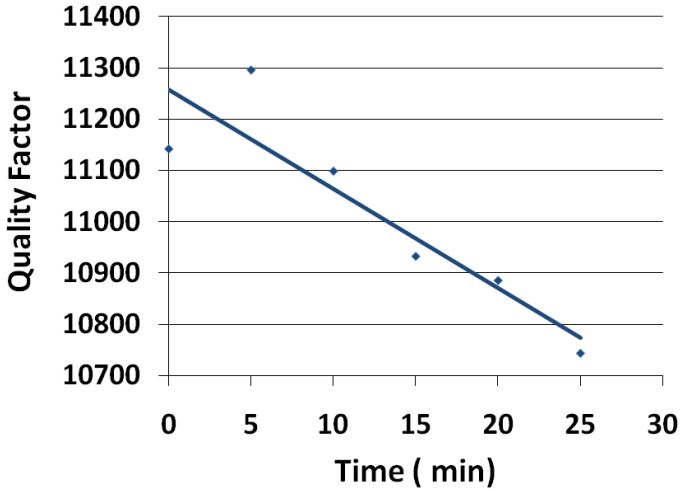

Figure 3.6 Measured quality factor versus overall exposure time to aerosol particles for the 61 MHz resonator in Fig. 3.2a.

3.3 Comparison of Different Technologies

Table 3.2 shows the comparison between the mass surface density sensitivity and absolute mass sensitivity as well as resolution for different technologies.

In our experimental setup, a minimum frequency shift of 10Hz could easily be detected using the network analyzer. For resonator mass sensitivity of 1.6kHz/pg, the experimental minimum detectable mass is approximately 7fg. However, this limit is much smaller than the limit imposed by the temperature induced frequency drift of the devices.

Table 3-2 Comparison of the mass surface density sensitivity and absolute mass sensitivity as well as resolution of the thermally actuated IBARs with that of different technologies such as QCM, SAW and FBAR.

Type of Sensor	Mass Surface Density Sensitivity /Mass Sensitivity	Mass Surface Density Resolution /Mass Resolution
QCM	$0.3-1.6\frac{Hz.cm^2}{ng}$ [16,17] / $1\frac{Hz}{ng}$ [7]	$\sim 10\frac{ng}{cm^2}$ [16,17] / $3000pg$ [7]
SAW	$15\frac{Hz.cm^2}{ng}$ [28, 29] / $260\frac{Hz}{ng}$ [8]	$\sim 1\frac{ng}{cm^2}$ [28,29] / $0.3pg$ [8]
FBAR	$\sim 800\frac{Hz.cm^2}{ng}$ [9]	$2.5\frac{ng}{cm^2}$ [9] / $1pg$ [9]
Piezoelectrically Actuated MEMS	$10\frac{Hz.cm^2}{ng}$ / $4\frac{kHz}{ng}$ [20]	$1\frac{\mu g}{cm^2}$ / $0.25pg$ [20]
Thermally Actuated MEMS	$15\frac{Hz.cm^2}{ng}$ / $1500\frac{kHz}{ng}$	$0.6\frac{ng}{cm^2}$ / $0.01pg$

Assuming temperature uncertainty of 10ºC (which is typical in targeted environmental applications) and typical resonator temperature coefficient of frequency (TCF) of -40ppm/ºC [30] for uncompensated silicon resonators, the frequency of a 26MHz resonator could shift by up to 10.5 kHz due to temperature. This limits the mass resolution to ~6pg. TCF as low as -0.05ppm/ºC has been achieved for compensated version of thermally actuated silicon resonators [30] reducing the temperature induced frequency inaccuracy of the same 26MHz resonator to 13Hz. This translates into a mass resolution of ~9fg which is equivalent to a particle diameter of ~180nm. Minimum detectable mass limits in the tens of pico-gram range [16,17] for QCM and SAW resonators and in the pico- gram range [9,28] for FBARs have been reported. However such estimates generally neglect the effect of temperature induced frequency uncertainties that typically make further increases of the minimum detectable limits.

3.4 Arbitrary Air-Borne Particle Measurements

After characterizing the resonator mass sensitivities using known particles, their performance in a real world application when exposed to arbitrary air-borne particles was investigated. In this experiment the PCB was placed in the same low pressure chamber. An air inlet, internally connected to the particle deposition nozzle, was left open allowing the air from outside (internal cleanroom air along with the particles suspended in it) to be sucked into the chamber and deposited on the resonator under test. The tests were carried out in the cleanroom (a class 1000 standard) so that a smaller number of air-borne particles would be deposited on the resonator. This would allow enough time between

arrival of different particles making it possible to detect and measure the effect of each particles by having small exposure intervals. A valve was also connected to the air inlet to allow turning the particle flow on and off. With the inlet valve closed, under a constant bias current, the resonance frequency was recorded. The inlet valve was then opened exposing the resonator under test to the air flow and consequently the aerosol particles. The exposure was done in 10 second intervals and after each exposure the resonator parameters were measured and recorded. With such relatively short exposure interval, in some intervals there were no particles deposited on the resonator. Therefore, when there was an actual frequency shift in an interval, with a good approximation it could be assumed to be due to a single particle deposited on the surface of the device. It should be mentioned that using the current devices, particles smaller than 200nm in diameter size could not be detected. Figure 3.7 shows the SEM view of one of the tested resonators after it was exposed to the air-borne particles in the cleanroom for 640 seconds.

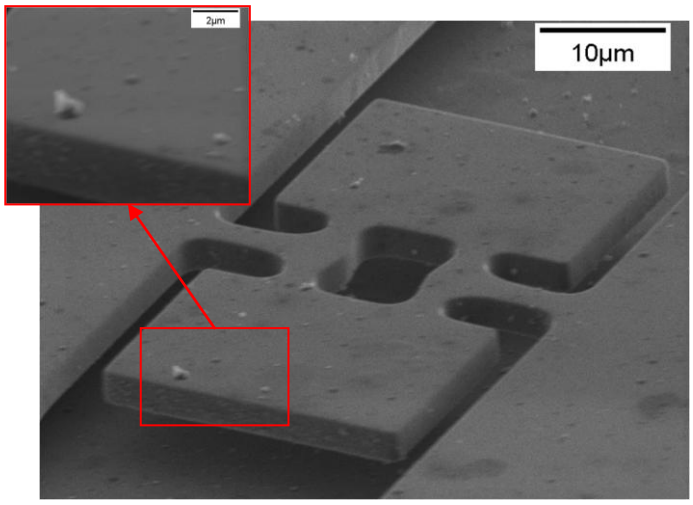

Figure 3.7. SEM view of one of the thermally actuated IBAR resonators after being tested under exposure to aerosol particles in the clean-room environment for a total time of 640 seconds.

Figure 3.8 shows the measured resonance frequency as a function of the exposure time. It should be noted that the resonator quality factors are surprisingly robust to the deposited particles.

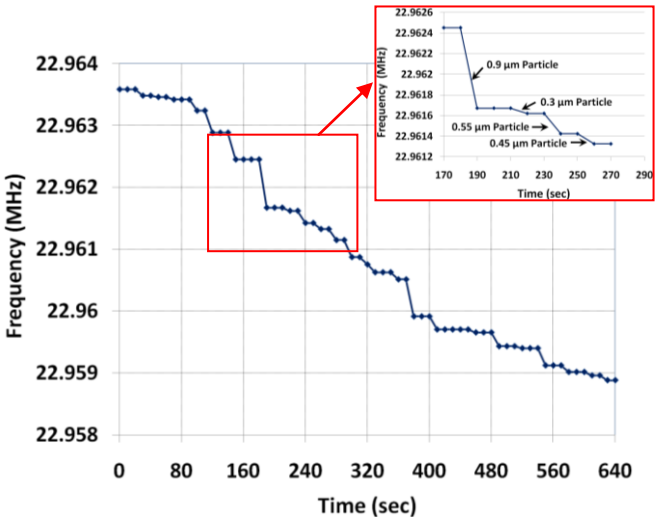

Figure 3.8. Change in the measured resonance frequency for a 22.9MHz 3.2 µm resonator as a function of the overall exposure time showing an overall frequency shift of ~4.7kHz (205ppm). Zoomed in view of the graph shows the amount of frequency shift during each interval allowing determination of the size of the deposited particle in each period.

After deposition of tens of particles of different sizes, no significant Q degradation was observed. This demonstrates their much higher robustness compared to capacitive resonators with extremely vulnerable air-gaps and multi-layered thin film piezoelectric resonators.

Based on the graph shown in Figure 3.8 and also the shift in frequency at each step, the deposited mass during that period can easily be calculated. Assuming an approximate density of 3g/cm^3 for the particles, the approximate diameter of the deposited particles in each time period could also be estimated. Figures 3.9a and 3.9b show the mass and diameter distribution of particles extracted from the measured frequency shifts for the 22.9 MHz resonator of Figure 3.7.

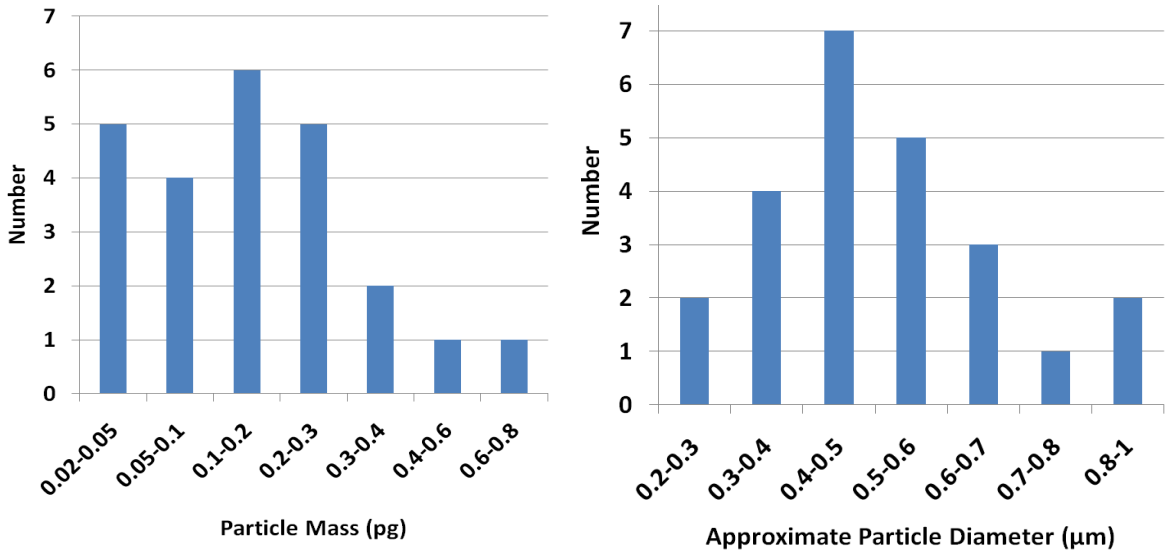

Figure 3.9. a) Graph showing the mass distribution of particles deposited on the 22.9 MHz device shown in Figure 3.7 based on measurement results shown in Figure 3.8. b) Graph showing the size distribution of particles deposited on the 22.9 MHz device shown in Figure 3.8. The density of the deposited particles was assumed to be 3g/cm^3.

Table 3.3 summarizes the measurement results for the different resonators tested in the cleanroom. The theoretical sensitivity is calculated based on the device dimensions of each device. Knowing the sensitivity, the total deposited mass which is also separately shown in the table can be derived.

Table 3-3 Summary of measurement results obtained from the resonators exposed to the flow of air-borne particles in a class 1000 softwall cleanroom. Theoretically predicted mass sensitivity as well as the size distribution data for the particles deposited on each.

Resonator Dimensions (µm)		**Q factor**	**Freq. (MHz)**	**Time (sec)**	**Freq. Shift (Hz)**	**% of particles detected for different diameters (µm)**							**Δm Accum-ulative mass (pg)**	**S_{theory} (kHz/ pg)**
a-b	**L-W-h**					**0.2 - 0.3**	**0.3 - 0.4**	**0.4 - 0.5**	**0.5 - 0.6**	**0.6 - 0.7**	**0.7 - 0.8**	**0.8 - 1**		
29.5-22	10.5-2.9-3.2	3680	29.153	350	-4960	0	6.2	25	37.5	18.7	6.2	6.2	3.35	1.471
30.5-21	10.5-3.5-3.2	3930	27.271	440	-3905	7.1	14.2	28.5	21.4	14.2	7.1	7.1	2.84	1.387
28-20.5	9-3.5-3.2	3850	26.642	460	-4570	4.7	14.2	28.5	28.5	19	0	4.7	3.53	1.371
31-20.5	12-3-3.2	4520	24.828	420	-3720	5.5	11.1	50	16.6	11.1	0	5.5	2.91	1.273
31.5-21.5	12.4-3-3.2	3970	22.964	640	-4700	8.3	16.7	29.1	20.8	12.5	4.2	8.3	4.56	1.106
31.5-21.5	12-3-3.2	4100	21.959	440	-2940	7.1	21.4	35.7	28.6	7.1	7.1	7.1	2.89	1.058

The distributive percentage of particles with diameters in different ranges deposited on each device is also included in the table. The overall air volume that was sucked into the vacuum chamber was calculated to be 1.2 ft^3. However also taking the ratio of the landing zone surface to the device surface area into account, the amount of air volume (that particles were collected from) actually being blown onto the device was 8×10^{-3} ft^3.

Cleanrooms are classified according to the number and size of particles permitted per volume of air. For a class 1000 of the US FED STD 209E standard, approximately 1000 particles per cubic foot with diameter ranges between 0.5μm and 5μm are permitted. Particle sizes less than 0.5μm in diameter size are non-applicable combinations for this class. Taking into account the amount of air volume which the particles in the experiments were collected from, there should be roughly 10 particles in that diameter range collected. Based on this, it was demonstrated that the particle concentration distribution in our cleanroom closely matches that of the class 1000 standard.

4. SELF-SUSTAINED MICROMECHANICAL RESONANT PARTICULATE MICROBALANCE/COUNTERS

A major advantage of thermal-piezoresistive resonators exploited in this work is their self-sustained oscillation capability.

Mutual interactions of thermal actuation and the piezoresistive effect can lead to a positive internal feedback loop maintaining mechanical vibrations without the need for a sustaining amplifier. Such self sustained oscillations have been recently demonstrated for high-frequency dual-plate extensional mode structures [31]. This unique property has been deployed in this work to demonstrate a prototype self-sustained sensor for air-borne particle monitoring.

4.1 Sensor Description

The finite element modal analysis result showing the resonant mode shape for a 4.6MHz dual plate resonator in its in-plane extensional mode is shown in Fig.4.1. This is pretty much the same IBAR structure used in the previous section with only support beams added to it. Red and blue colors show locations with the largest and smallest vibration amplitudes respectively. At resonance the two plates move back and forth in opposite directions causing the narrow actuator beams to expand and compress periodically. The 4 support beams on the outer corners of the plates are to increase the vertical stiffness of the structure and avoid stiction of the plates to the handle layer during

device fabrication. Since the in-plane stiffness of the moving plates is orders of magnitude larger than that of the actuator and support beams, their deflections in the in-plane resonance mode are negligible resulting in the plates to vibrate with uniform vibration amplitude as a whole. Therefore, the effect of similar particles added to different locations on the plate, on the overall resonance frequency of the structure will be the same. Such uniform mass sensitivity on the surface of the plate enables measurement of the mass of individual particles.

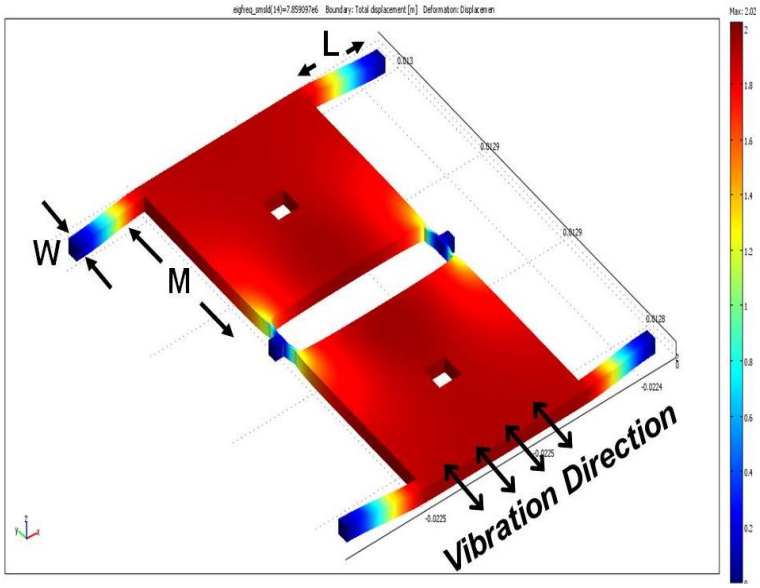

Figure 4.1. COMSOL modal analysis, showing the in-plane resonance mode shape of interest for a 4.6MHz dual-plate resonator. The two plates move back and forth in opposite directions while the narrow actuator beams undergo periodic compression and extension. Red and blue colors show locations with the largest and smallest vibration amplitudes respectively.

Fabrication of the resonators was carried out using the standard single mask SOI-MEMS process which has previously been explained in previous chapters [25]. Thermally actuated oscillation is initiated by passing a DC current between the two support pads on their two sides of the structure. Due to their higher resistance, most of the electrical ohmic loss is generated in the thin extensional beams located in the middle of the structure. The beams expand due to thermal stress and the resulting inertia in the

plates causes an over-expansion and consequently tensile stress in the beams. Due to the negative longitudinal piezoresistive coefficient of N-type silicon, tensile stress in the beams will cause their electrical resistance to decrease. With the constant bias current, this translates into lowered ohmic loss forcing the actuator beams to contract. The same sequence is repeated after the structure over-contracts due to the inertia in the plates (resonant behavior). If the overall loop gain for this sequence is larger than one, i.e. the thermal energy fluctuations that actuate the structure are larger than the mechanical energy loss of the structure in each period, this sequence keeps repeating itself. In this manner the vibration amplitude keeps increasing until it reaches a saturation point (e.g. due to mechanical nonlinearities). Hence, if large enough DC bias current is applied to a thermal-piezoresistive resonator with negative piezoresistive coefficient, it will initiate self-sustained oscillations at its mechanical resonant frequency. Figure 4.2 shows the SEM view of a 3μm thick 4.6MHz dual-plate resonator which was fabricated on an N-type low resistivity SOI substrate with a buried oxide layer (BOX) thickness of 5μm.

The output signal showing self-oscillation of the 4.6MHz resonator by application of only a 1.4mA DC bias current is also shown (no amplifier was used).

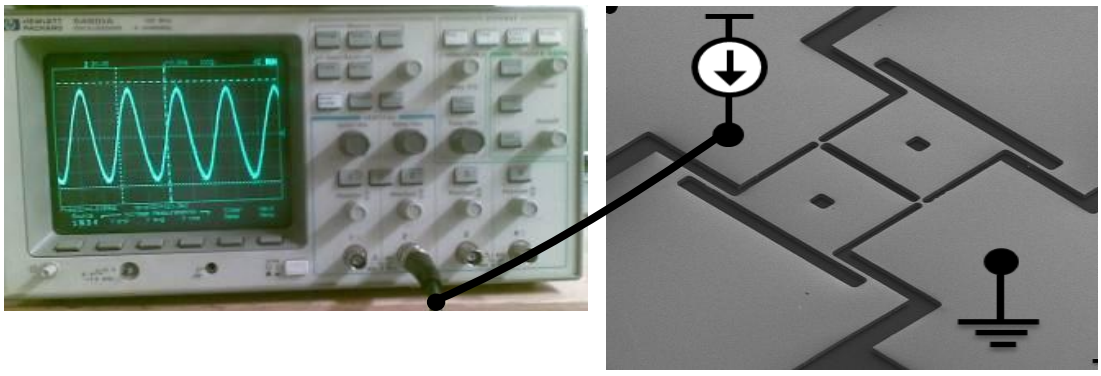

Figure 4.2. SEM view and output voltage of a self-oscillating 4.6MHz 3μm thick thermal-piezoresistive resonator. Only a DC bias current of 1.4mA is being applied to the resonator (no amplifier).

4.2 Particle Measurement Results

Figure 4.3 shows the test setup used for characterization of sensory behavior of the oscillators and its schematic diagram which is very similar to the test setup in Figure 2.10 except that here, the output of the micromechanical oscillator is directly connected to a frequency counter. Oscillating resonators with different dimensions were exposed to the flow of particles for several consecutive intervals of a few minutes each. After each interval, the oscillator frequency was recorded.

Figure 4.4 shows the SEM view of the resonator of Fig. 4.2 after exposure to the flow of particles coming out of the particle generator for 108 minutes showing hundreds of particles deposited on its surface.

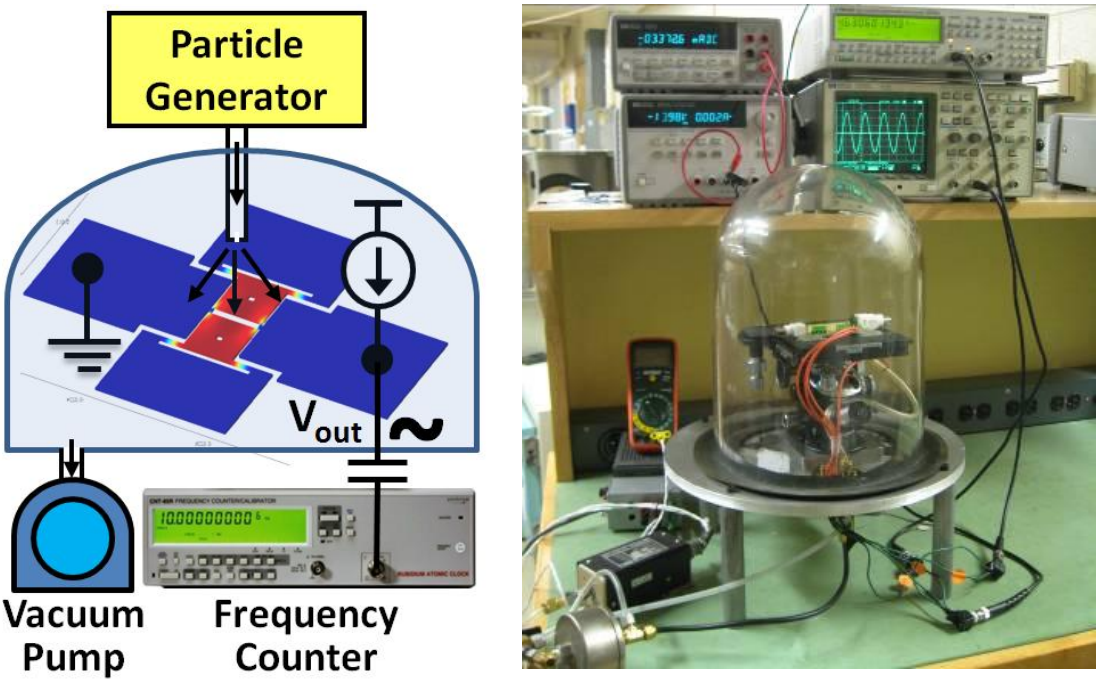

Figure 4.3. Schematic diagram and camera picture of the test setup used for characterization of resonator mass sensitivities. The suction caused by the vacuum pump and resulting low vacuum (~70Torr) under the bell-jar accelerates the particles towards the resonator. The particles are directed towards the resonator through a nozzle embedded in a microscope. The microscope facilitates alignment of the nozzle to the resonator under test.

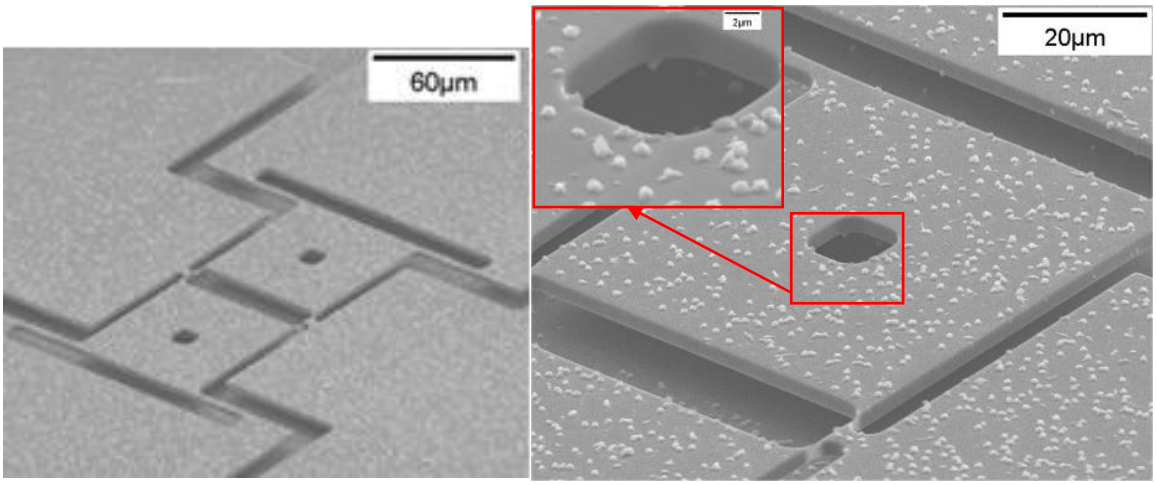

Figure 4.4. SEM view of the resonator of Fig. 4.2 and parts of it after exposure to the flow of ~1µm diameter particles for 108 minutes.

Figure 4.5 shows the measured frequency drift of the oscillating resonator of Fig. 4.2 during the 108 minute particle deposition period showing an overall frequency shift of 14.1 kHz. A zoomed in view of the graph, also shown in Fig. 4.5, reveals the quantized nature of the frequency shift steps enabling one to count the number of particulates deposited in each time period.

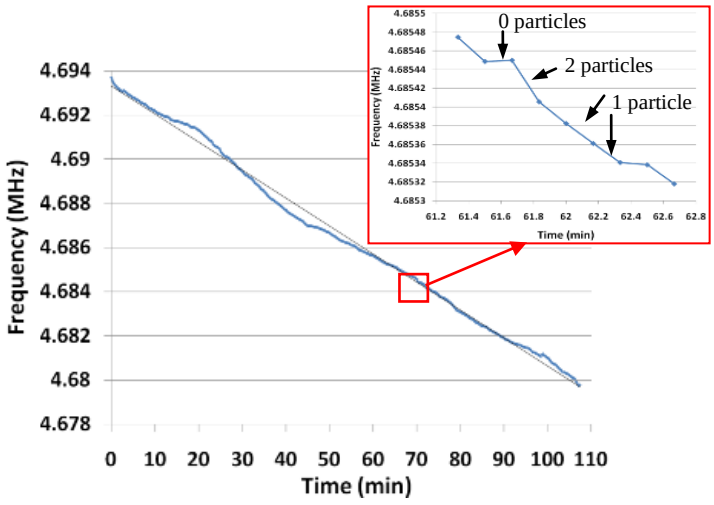

Figure 4.5. Change in the measured resonance frequency for the 4.6MHz resonator of Fig. 4.2 as a function of the exposure time showing an overall frequency shift of ~14.2KHz. Zoomed in view of part of the graph shows quantized frequency shift slopes allowing determination of number of particles deposited in each period.

Table 4.1 includes measurement results from different devices showing a good agreement between the measured frequency shifts caused by the added mass of particles and the calculated frequency shifts based on the resonator dimensions and number of deposited particles. Resonator mass sensitivities are in the 10-30 Hz/pg range. As expected, mass sensitivities are higher for higher frequency and smaller size devices.

Table 4-1 Summary of measurement results obtained from different self-oscillating resonators and their comparison with theoretically predicted values showing a good agreement between the two.

Resonator Dimensions (μm) (M/L/W)	**V_{pp} (mV)**	**I_{bias} (mA)**	**R (KΩ)**	**Power (mW)**	**Freq. (MHz)**	**Time (min)**	**Δf_{meas} (kHz) ppm**	**Number of Particles Counted ΔM (pg)**	**Measured Sensitivity (Hz/pg)**	**Theoretical Sensitivity (Hz/pg)**
72/14/0.3	136	1.33	7.8	13.8	4.69370	0	-14.16	695	31.5	32.2
					4.68636	53				
					4.67954	108	3016	450		
97/14/0.3	138.5	1.21	1.6	2.34	3.45966	0	-5.35	540	15.3	13.5
					3.45734	20				
					3.45432	46	1545	350		
194/58/3	252	7.3	3.1	165	1.977988	0	-7.04	5495	1.99	1.93
					1.974562	125				
					1.970946	256	3560	3540		

Therefore here it was shown that self-sustained thermally actuated micromechanical oscillators were fabricated and used as highly sensitive mass sensors for detection of airborne particles. Artificially generated air-borne particles were used to characterize the resonant sensors. Mass sensitivities as high as 31.5Hz/pg were measured for the microbalance sensors that are in good agreement with the theoretically calculated mass sensitivities. Due to the quantized nature of the frequency shifts, the number of particles deposited during each time interval was distinguishable.

4.3 Analysis of Robustness towards Air-Borne Particles

One of the requirements of the discussed resonant particulate sensors as commercially viable products is their robustness towards particle loading. Generally, such devices stop working after loading with an excessive amount of particles. This could be due to the particles getting stuck in the gaps between the resonating parts and stationary surroundings, or due to introducing excessive imbalance or mechanical loss to the structure significantly degrading the resonator quality factor making the resonant peak undetectable, or the self-sustained oscillation impossible. One of the important parameters to be investigated and determined in this regard is the maximum mass loading that such devices can tolerate, hence providing an estimate of typical device life-times in different applications.

Table 4-2 Summary of measurement results showing frequency shifts before the resonators stopped working for resonators with different size plates under lower test setup pressure. It can be seen that resonator with larger dimensions (more release holes) tend to have less robustness towards airborne particles whereas resonator with less release holes, show more robustness and show a larger shift in frequency before they stop working.

Resonator Dimensions (M / L / W)	**Frequency (MHz)**	**Frequency Shift (kHz)**	**Frequency Shift (%)**
70 / 15 / 0.3	5.17	390	7.5
70 / 15 / 0.3	5.1	280	5.5
70 / 15 / 0.3	5.25	260	49520
70 / 15 / 0.3	5.2	370	71150
70/ 15 / 0.3	4.56	270	59210
100 / 15 / 0.3	2.21	58	26250
100 / 15 / 0.3	2.38	89	37400
100 / 15 / 0.3	2.52	64	25400
100 / 15 / 0.3	2.4	85	35420
100 / 15 / 0.3	2.46	73	29680
200 / 60 / 0.3	1.39	19	13670
200 / 60 / 0.3	1.36	27	19850
200 / 60 / 0.3	1.22	21	17210
200 / 60 / 0.3	1.41	27	19150

Therefore a series of tests were carried out in which devices with different dimensions were exposed to regular air particles in the environment using the same impactor setup explained in the previous sections. The tests were all carried out in an identical environment. However to make sure that nozzle pressure does not speed up the process of impact and lead to sudden failure of the devices, the pressure in the chamber was reduced in comparison to the previous experiments. This was done by making a leak pathway in the chamber and therefore preventing a high vacuum being made. The results obtained were interesting in the sense that larger resonant devices with more release holes were less robust to air-borne particles and the overall frequency change shown by them before break down/non-functionality was less than the smaller resonator with less release holes. Frequency shifts as high as 7.5% were obtained for devices with one single release hole in each plate. It is understood that the particles go through each of the release holes and at some point gradually get trapped in the gap layer between the resonator and the handle substrate, eventually leading to device becoming non-operational.

5. TEMPERATURE COMPENSATION OF THERMALLY ACTUATED HIGH FREQUENCY SILICON MICROMECHANICAL RESONATORS THROUGH HIGH CONCENTRATION PHOSPHORUS DOPING

Issues such as the temperature drift of Micro-Electro-Mechanical Systems (MEMS) silicon resonators are among major drawbacks in their competition with temperature compensated crystal oscillators and conventional quartz crystals as commercially viable miniaturized frequency references and sensors. Silicon resonators typically exhibit temperature coefficient of frequency (TCF) in the -20 to -40ppm/ºC range [26,32] whereas the temperature compensated crystal oscillators, known as TCXO commercially available, have an overall temperature drift as low as ~ ±3.5ppm over the range of -20ºC to 70ºC [33]. The relatively large negative TCF of silicon resonators is mainly due to the softening of the structural material as the temperature increases. This change in stiffness, translates into a change in the resonant frequency of the structure.

A number of both active and passive temperature compensation techniques have been demonstrated for improvement of the temperature stability of MEMS resonators. One of the active temperature compensation approaches is to utilize a tunable resonator along with a temperature sensitive circuit applying the appropriate tuning signal to the resonator in accordance with changes in temperature [34]. Another active method is to encapsulate the resonator in a miniaturized thermally isolated container (micro-oven). In

this approach heating elements keep the temperature of the isolated area constant at an elevated level to achieve frequency stability [35-37]. In addition to the power consumption issues, the general disadvantage of active compensation techniques is the added complexity and cost to the system.

A number of passive resonator temperature compensation techniques, that are generally more desirable, have also been demonstrated. One of such techniques that can only be applied to lower frequency air-gap electrostatic resonators is to make the resonator and its electrode(s) out of different materials. If designed properly, the difference between thermal expansion coefficients of the two materials can tune the gap size and consequently the resonator frequency with temperature to cancel out the effect of structural material softening [38]. Another passive temperature compensation technique is utilization of composite structures made of materials with opposing elastic constant temperature dependence [39, 40]. The geometric design of the structure has also shown to contribute to the temperature drift behavior [41]. Finally, high concentration p-type doping of silicon has proven to be a highly effective and simple temperature compensation solution [14].

Although thermally actuated resonators operate at elevated temperatures due to the bias current required for their operation, they generally follow a similar trend of sharp negative frequency drift as their surrounding temperature increases. This is due to the fact that their temperature, even though higher than the surroundings, still changes with the changes in the surrounding temperature. Significantly improved temperature stability has been demonstrated for highly N-type (Phosphorous) doped single crystalline silicon

thermal-piezoresistive resonators [30] and a comprehensive study of significantly improved temperature stability for single crystalline silicon thermal-piezoresistive resonators using highly N-type (Phosphorous) doping has been demonstrated.

5.1 Operating Principle

The resonators utilized in this work are the same I-shaped Bulk Acoustic Resonators (IBARs; also known as dog-bone resonators) [24, 27] presented in chapter 3.

The standard single mask SOI MEMS process was used for fabrication of the resonators as talked about previously. Figure 5.1 shows the SEM view of a fabricated 60MHz IBAR. In order to reduce the bias current required for operation of the resonators and minimize their power consumption, the actuator beams were narrowed down.

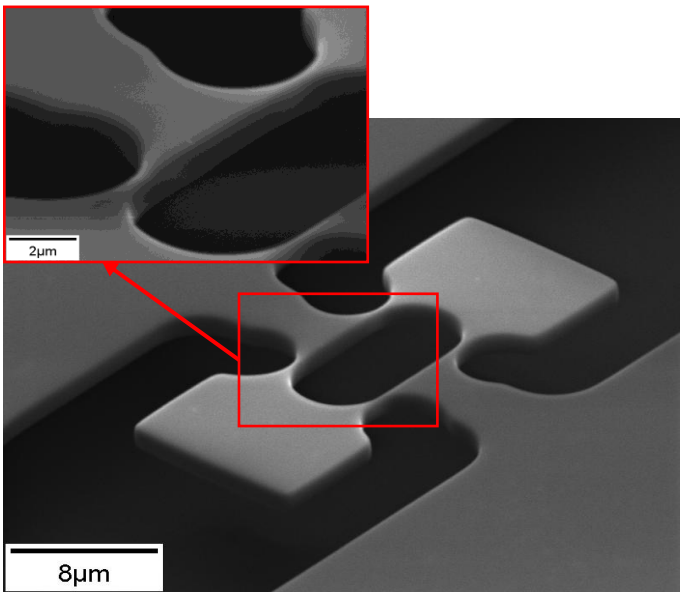

Figure 5.1. SEM view of a 60MHz thermal-piezoresistive IBAR and the zoomed in view of its actuator beams showing their submicron width achieved through thermal oxidation and oxide etch. The resonator is fabricated on a low resistivity (~0.01Ω.cm) N-type SOI substrate using a single mask process including device layer patterning (silicon DRIE) and undercut in HF.

This narrowing of the actuator beams were done by performing a number of consecutive thermal oxidation and oxide removal steps after the devices were released. At the same time, the resonator thicknesses were also reduced.

The mechanical stiffness of the IBAR structures in the in-plane extensional resonant mode of interest is supplied by the actuator beams. Since the IBAR resonators have very narrow actuator beams, high concentration dopant levels can be achieved all the way through the bulk of the beams using relatively short doping and drive-in steps. This highly reduces the amount of time required for doping compared to the bulk structures in [42] making it a much more convenient approach.

5.2 Measurement Results

Temperature induced frequency drift of the fabricated resonators were measured by placing them in a temperature controlled oven and monitoring their resonant frequencies at different elevated temperatures. The blue plot in Figure 5.2 shows the measured frequency drift of -38ppm/ºC for a 22.1MHz IBAR. It was observed that as expected, the elevated temperature of the resonator due to the current flows does not affect its temperature drift characteristics.

To investigate the effect of doping on such resonators, a similar device was doped at 950ºC for 2 hours using a solid phosphorous source followed by 2 hours of annealing at 1100ºC (drive-in). The measured temperature drift behavior for this resonator is shown by the red plot in Figure 5.2 showing a TCF of +0.7ppm/ºC.

Obtaining a positive value for the temperature drift coefficient of frequency after doping is very interesting. This positive TCF value which was obtained due to the high

dopant concentration penetrating through the narrow beams, shows that if different parameters are optimized, it should be possible to keep the TCF exactly where the transition from negative to positive TCF occurs, and therefore have a zero TCF point.

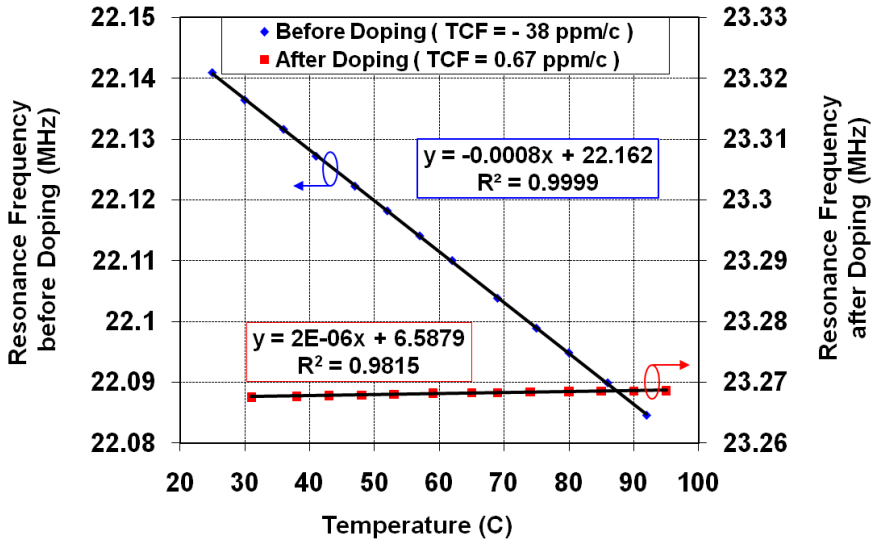

Figure 5.2 Measured temperature drift characteristics for two similar IBARs before and after being highly doped with phosphorous. The undoped resonator shows TCF of -38ppm/ºC, while the temperature drift coefficient for the doped resonator has decreased significantly and even turned positive to the value of +0.7ppm/ºC.

5.2.1. Dependence of TCF on bias current

One interesting trend that can be observed for the doped resonators is that when operated at higher bias currents (higher static temperature) the TCF values become more positive (or less negative). Therefore by having the right doping level and bias current, potentially zero TCF can be achieved for such devices. Figure 5.3 shows the measured temperature characteristics of the highly doped 60MHz resonator of Fig. 5.1 measured at two different bias currents. The two plots show slightly different TCF values, showing that the resonator TCF can be tuned by changing its operating bias current.

Figure 5.4 shows the same trend for the measured TCF of a highly doped 8.2MHz resonator operating at two different bias currents. By adjusting the bias current, a linear

temperature drift as low as -0.05ppm/ºC equivalent to an overall temperature drift of -3.6ppm over the range of 25ºC to 100ºC has been achieved for this resonator.

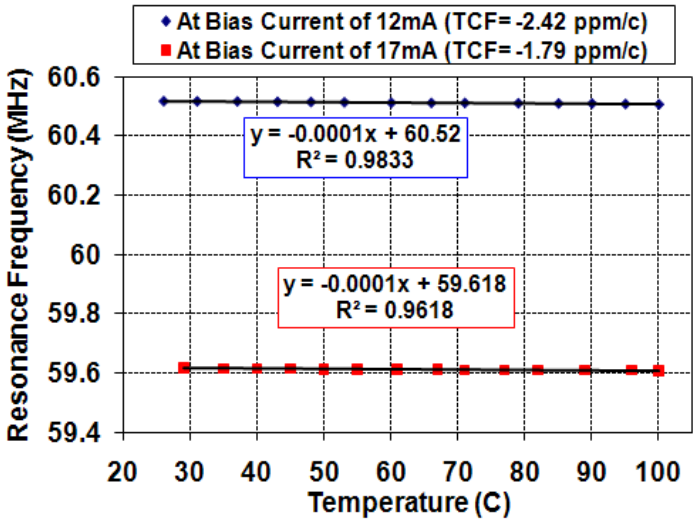

Figure 5.3. Temperature drift characteristics for the 60MHz resonator of Fig. 5.1 measured under different bias currents.

At such high stability level we are basically limited to our measurement accuracy and the real TCF could even be lower than the mentioned value.

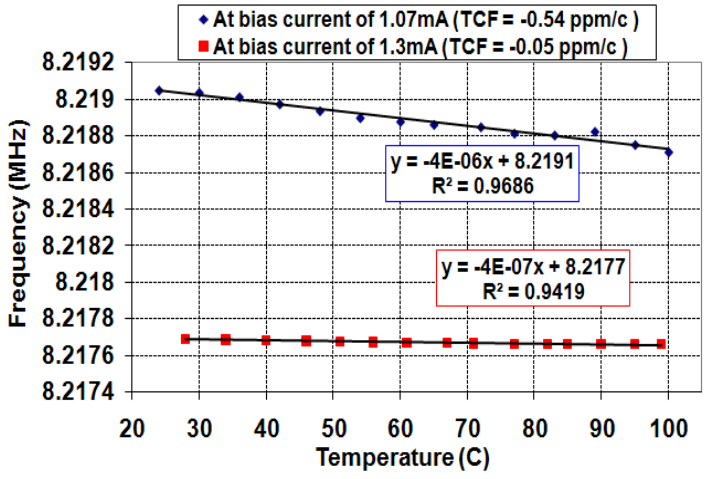

Figure 5.4. Temperature drift characteristics for a highly doped 8.2MHz resonator measured at two different bias currents. Similar to Fig. 5.3, higher bias current results in a higher TCF (lower negative TCF). By choosing an optimized bias current, TCF as low as -0.05ppm/ºC has been achieved.

Another point that needs to be discussed here is that before temperature compensation, the resonant frequency of thermally actuated resonators is sharply dependent on their bias current. This is due to the fact that any change in bias current translates into a change in the temperature of the device (Joule heating) and therefore frequency drift. This could be a major problem for implementation of frequency references because any noise or fluctuations in the bias current of such devices will turn into oscillator phase noise or frequency drift.

In order to demonstrate the dependence of the resonator frequency on the bias current and its correlation with TCF, a parameter *a* has been defined. This is mainly because due to different device dimensions, comparing the dependence of the resonator frequencies with their bias current would not provide a valid (apple to apple) comparison. The changes in *a* is equal to the changes in the temperature difference of the actuating beams of the devices with the surroundings (room temperature). As shown in equation 5.1, this parameter was calculated by multiplying the power consumed (*P*) in the resonator actuator beams by a factor proportional to its thermal resistance (R_{Th}). The unit for thermal resistance is *(ºC/W)* and therefore multiplying thermal resistance by power is going to give the unit of temperature.

$$a = P.R_{Th} \tag{5.1}$$

On the other hand, thermal resistance is the temperature difference across a structure when a unit of heat energy flows through it in unit time. For an actuating beam with the cross sectional area *A* and length *L*, its thermal resistance equals:

$$R_{Th}\,\alpha\,\frac{L}{A} \tag{5.2}$$

Figure 5.5 shows the measured frequency change for different resonators versus *a*.

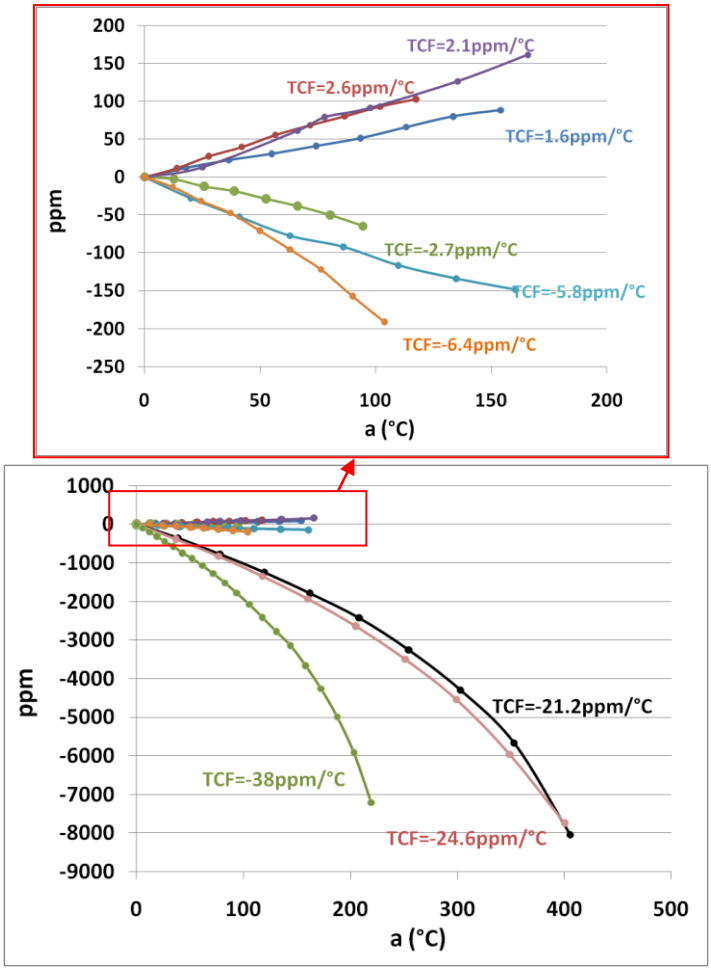

Figure 5.5. Comparison between the frequency-dependent curve of several resonators with different TCF values is shown. The frequency change with increase in bias current is demonstrated. For the less compensated resonators, the resonant frequency change is much higher (7000-8000ppm range) with increase in the actuating beam temperature, while in the highly doped temperature compensated resonators, the overall frequency shift is shown to be less. Zoomed in view of the graph shows lesser frequency shifts (200ppm range) of the more compensated resonators with increase in the temperature of the actuating beams [14].

resonant frequency change is much higher (7000-8000ppm range) with increase in the bias current, while in the highly doped temperature compensated resonators, the overall frequency shift is shown to be much less (200ppm range). Therefore it can be seen

that by doping of the resonators, the sharp dependence of their resonance frequency on the bias current is highly suppressed.

5.2.2 Dependence of TCF on Resonator Beam Width and Doping Temperature

In order to investigate the dependence of TCF on resonator doping level, a number of resonators with different stiffness element width were doped at different temperatures.

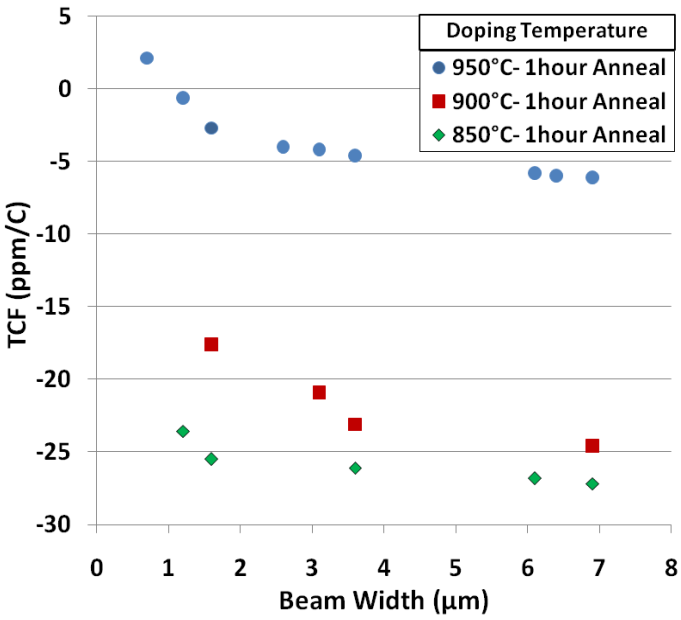

Figure 5.6. Measured TCF values for different highly phosphorous doped resonators based on the temperature to which they were doped at and also the maximum width of actuator beams (stiffness element) in the middle of their sturucture. All the resonators were doped for a duration of two hours and annealed for one hour. It is clearly visible that as the width of the beam gets narrowed and also with increase in doping temperature the TCF values tend to become more positive [14].

As can be seen in Figure 5.6 for resonators doped at the same temperature, the ones with the narrower actuator beams have a less negative TCF in comparison to those with wider actuator beams. This is due to higher dopant concentration being achievable all the way through the bulk of the beams (stiffness element) for the narrower beams. Figure 5.6 also demonstrates that as expected, higher doping temperatures result in higher dopant concentrations, leading to more positive TCF values.

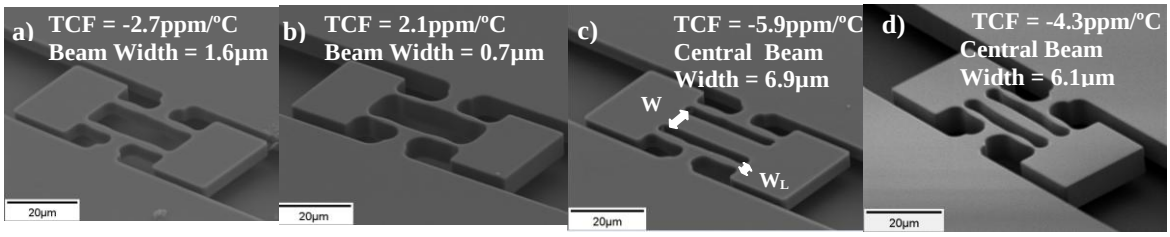

Figure 5.7. a) SEM view of a 21.8MHz I2-BAR. The actuator beams are 1.6µm wide. The measured TCF for this resonator at a bias current of 81mA was measured to be -2.7ppm/ºC; b) SEM view of an 18.3MHz I2-BAR fabricated on a similar substrate. This device was initially identical to the previous device but its actuating beams were narrowed down to 0.7µm by thermal oxidation. The measured TCF for this resonator at a bias current of 46mA was 2.1ppm/ºC ; c) SEM view of a 37.2MHz I3-BAR; The actuating beam in the middle of the structure is 6.9µm wide while the lateral actuating beams are 1.6µm. Other dimensions such as plate dimension and the length of the actuating beams are similar to the I2-BAR. The measured TCF for this resonator at a bias current of 76mA was -5.9ppm/ºC. ; d) SEM view of a 24.7MHz I3-BAR. The actuator beam is 2.6µm wide while the lateral actuating beams are 0.8µm. Other dimensions such as plate dimension and the length of the actuating beams are similar to the other IBARs. The measured TCF for this resonator at a bias current of 48mA was -4.3ppm/ºC. All devices were fabricated on 100 SOI low resistivity n-type substrates and were phosphorus doped for 2 hours under similar conditions at a temperature of 950°C. They were then annealed at a temperature of 1100°C for an hour.

Table 5.1 summarizes measured TCF values for a number of different IBAR resonators, some of which are shown in Figure 5.7, with different bias currents.

Comparison between I^2-BAR's (I-shaped resonators with two extensional actuating beams in the middle of the structure) and I^3-BAR's (I-shaped resonators with three extensional actuating beams in the middle of the structure) generally show that for the I^3-BAR's devices, due to the thicker third actuating beam in the middle of the structure (thicker stiffness element), those devices are generally less temperature compensated. Other than that the TCF measurement results for a number of devices at different bias currents has also been demonstrated.

Table 5-1 Measured TCF values and other characteristics for different highly phosphorous doped resonators under different bias conditions. The resonators were similarly phosphorus doped for different durations and at different temperatures and later annealed at a temperature of 1100°C for one hour (*: Dope duration was 2 hours instead of 1 hour.)

Resonator Dimensions (μm)						Freq. (MHz)	Q_{air}	Bias DC (mA)	R_{DC} (Ω)	Power (mW)	Doped Temp.(°C)	TCF PPM/°C
a	b	L	W_L	W_m	H							
33	23	36	1.6	-	4.6	21.8	5200	68.9	18.9	89.72	950	**-3.95**
							4400	81.2	18.9	124.6	950	**-2.7**
							4100	88.3	18.9	147.3	950	**-2.1**
33	23	36	1.6	3.6	4.6	28.2	5850	66.6	21.5	95.36	950	**-5.8**
							5200	79.9	21.5	137.2	950	**-4.6**
33	23	36	1.6	6.9	4.6	37.2	3600	67.4	19.1	86.76	950	**-6.3**
							3150	75.5	19.1	108.8	950	**-5.9**
31.4	22.3	36	1.2	-	8.2	18.2	5390	56.5	18.2	58.09	950	**-1.2**
							4800	65	18.2	76.89	950	**-0.65**
30.2	21.8	36	0.7	-	7.8	18.3	5700	45.7	14.1	29.44	950	**2.1**
							5450	59.2	14.4	50.46	950	**2.65**
33	23	36	1.6	3.1	8.2	25.1	3740	56.8	18	58.07	950	**-4.7**
							3400	64.7	18	75.34	950	**-4.2**
33	23	36	0.8	2.6	8.2	24.7	5400	48	14.6	33.63	950	**-4.3**
							5150	61.2	14.6	54.68	950	**-4**
33	23	36	1.6	6.4	8.2	28.6	4270	56.9	17.7	57.30	950	**-6**
							4050	73.6	17.7	95.88	950	**-5.9**
33	23	36	1.6	3.6	4.6	31.8	5450	45	103	208.5	900	**-23.1**
33	23	36	1.6	-	4.6	22.8	8100	24.4	116	69.06	850	**-25.5**
33	23	36	1.6	3.6	4.6	33.4	6050	17.4	125	37.84	850	**-26.4**
33	23	36	1.6	6.9	4.6	37.2	5870	12.3	119	18	850	**-27.2**
30.6	20.6	14.9	0.7	-	2.6	23.2	2600	5.31	50.5	1.42	950*	**0.67**
30.2	20.2	30.8	0.2	-	2.2	8.21	7500	1.07	155	0.18	950*	**-0.54**
							7000	1.30	155	0.26	950*	**-0.05**

5.3 Discussion

The exact phenomena leading to doping induced temperature compensation of resonators are not completely understood at this point. However, one possible explanation could be the nonlinear dependence of the electronic bandgap of silicon on mechanical strain. It is well known that the electronic bandgap of silicon changes due to mechanical stress and applying tensile stress results in reduction of the gap size [24]. However, although to the best of our knowledge no accurate data is available, most likely

this dependence is not a linear function and includes some higher order terms as demonstrated in equation 5.3.

$$E_g = E_0 - C_1 * \varepsilon + C_2 * \varepsilon^2 + ... \tag{5.3}$$

In this equation, ε is the applied tensile strain, E_g is the strain dependent energy of an electron in the conduction band and E_0 is the initial energy gap.

The relationship between mechanical force and energy level of a system is also known from basic physics. Equation 5.4 shows the fact that forces formed in physical systems always tend to move the system towards the lowest possible energy level. For example, a force generated by a compressed spring wants to return the spring back to its undeformed form that has the lowest stored energy level.

$$F = -\frac{dE}{dx} \quad \Rightarrow \quad \frac{dE_e}{dx} = -F_{electrical} \tag{5.4}$$

Applying this same principle to the strain dependent energy of an electron in the conduction band of silicon results in an internal mechanical force ($F_{electrical}$) that will be referred to as electrical force.

$$E_e = nE_g = n(E_0 - C_1 * \varepsilon + C_2 * \varepsilon^2 + ...) \tag{5.5}$$

$$F_{electrical} = n(-C_1 + C_2 * \varepsilon) \tag{5.6}$$

As shown in equation 5.5, this force has a constant term coming from the linear term in the electronic gap-strain equation and a term that is proportional to the applied strain and comes from the second order term of the gap equation. This term is equivalent

to a mechanical stiffness that can be referred to as the electrical stiffness ($K_{electrical}$) because it is a result of the electrical energy in the system. Here we are assuming that the electrical stiffness is a function of temperature which increases with temperature.

$$K_{electrical} = nC_2(T) \tag{5.7}$$

So the overall stiffness of the structure has a purely mechanical component that decreases with temperature and an electrical term that increases with temperature. If the temperature dependence of the electrical term is large enough, it can cancel out the effect of the temperature dependence of the mechanical stiffness and lead to temperature compensation. Since the electrical stiffness increases by increasing the number of electrons, at high doping levels its value becomes large enough to compensate the effect of mechanical stiffness completely. Furthermore, since the number of free carriers increases with temperature, the effect of this electrical stiffness increases as the resonator is operated at higher bias currents.

Therefore doping induced temperature compensation of thermally actuated N-type single-crystal silicon was demonstrated. Measurement data showing the correlation between doping concentration throughout the resonator stiffness elements and resonator TCF was presented showing that as expected, higher doping concentrations lead to less negative (more positive) TCF.

While highly suppressed temperature drifts were achieved for highly doped structures, it was observed that the resonator bias current provides an added degree of freedom enabling further fine tuning of the resonator TCF. Temperature compensated

resonators with fine tuned overall temperature drifts as low as -3.6ppm over the range of 25ºC to 100ºC were demonstrated.

Temperature compensation using the presented technique can not only minimize the temperature drift, but is also expected to improve the short term stability, including phase noise characteristics, of oscillators implemented utilizing such frequency references by eliminating the sharp dependence to electronic noise in the resonator bias current.

5.4 Temperature Compensated Single-Device Electromechanical Oscillators

Having already demonstrated temperature compensation and already knowing that the presented devices can self-oscillate, by putting the two together, stable oscillators can be made. Figure 5.8 shows the finite element modal analysis for one of the dual plate in-plane extensional mode resonators that have been used in this work.

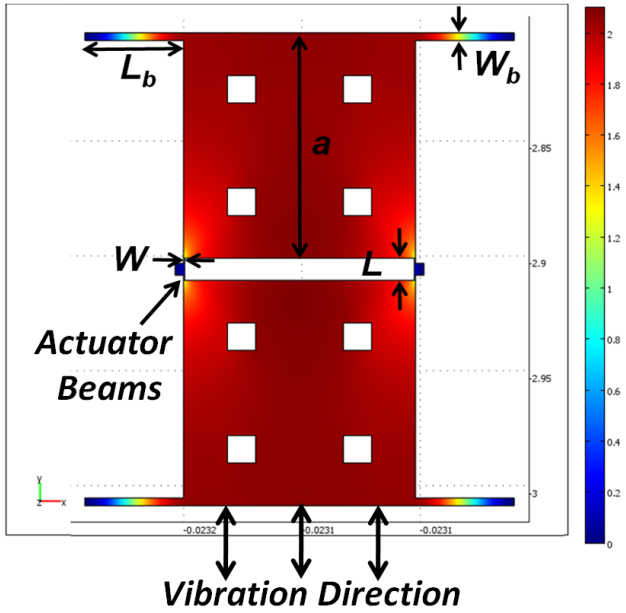

Figure 5.8. COMSOL modal analysis results, showing the in-plane resonance mode shape for a 4.23MHz dual-plate extensional mode resonator.

At resonance the two plates move back and forth in opposite directions causing the narrow actuator beams in the middle to expand and contract periodically. The four support beams on the outer corners of the plates are to increase the vertical stiffness of the structure and avoid stiction of the plates to the handle layer during device fabrication and release. The short narrow beams in the middle of the structure act as both thermal actuators and piezoresistive sensors. They also supply the structural stiffness for the resonant mode of interest and therefore temperature compensation can be achieved by minimizing temperature dependence of the stiffness of the actuator beams only.

Temperature compensation can be achieved in the structure of Fig. 5.8 by reaching high N-type dopant levels in the narrow beams that supply its mechanical stiffness. Due to the very small (submicron) width of the beams, this can be done by performing relatively short thermal diffusion doping and drive-in steps [30].

Thermal actuation of such resonators is performed by passing a fluctuating current between the two support pads on the two sides of the structure. Due to their higher resistance, most of the ohmic loss occurs in the thin actuator beams, causing a periodic thermal stress that can actuate the structure in its in-plane resonant mode. Due to the piezoresistive effect, the resulting alternating stress in the beams (which is maximized at resonant frequency) modulates the DC bias current in the structure leading to a motional current component (output current of the device). The motional conductance of the resonators (which is the ratio of motional output current versus input voltage) is shown in [31]:

$$g_m = \frac{i_m}{v_{ac}} = 4\alpha E^2 \pi_l Q \frac{A I_{dc}^{\ 2}}{KLC_{th}\omega_m} \tag{5.8}$$

where α, E, and π_l are the thermal expansion coefficient, Young's modulus, and longitudinal piezoresistive coefficient of the structural material, A, L, and C_{th} are the cross-sectional area, length, and thermal capacitance of the thermal actuators, and Q, K, ω_m, i_m and I_{dc} are the quality factor, mechanical stiffness, resonance frequency, motional and DC bias currents of the resonator respectively. According to Eq. 5.8, the motional conductance for a thermal-piezoresistive resonator becomes negative if the structural material has a negative piezoresistive coefficient (π_l). A negative resistance (or negative conductance) in electronics is equivalent to an active energy pump feeding some energy back into the mechanical structure. If the absolute value of the negative motional conductance resulting from negative piezoresistive coefficient is increased (by increasing the DC bias current) to reach and surpass the electrical conductance of the resonator structure (R_A^{-1}) that acts as a feed-through, instead of the resonator losing part of its energy in every cycle, it gains some extra energy in each cycle. This leads to instability of the resonant system and self-sustained oscillation. This can be explained by the internal positive feedback resulting from mutual interactions of thermal actuation and the piezoresistive effect which is illustrated in Fig. 5.9 [31].

Highly doping the structure significantly reduces R_A necessitating a proportionally higher g_m to initiate self-oscillation. Therefore, I_{dc}^2 has to increase proportionally to achieve self-sustained oscillation in temperature compensated structures. This alone does not lead to higher power consumption for the oscillator as the reduced structural resistance and increased current cancel the effect of each other out in the power equation ($P = R_A.I_{dc}^2$).

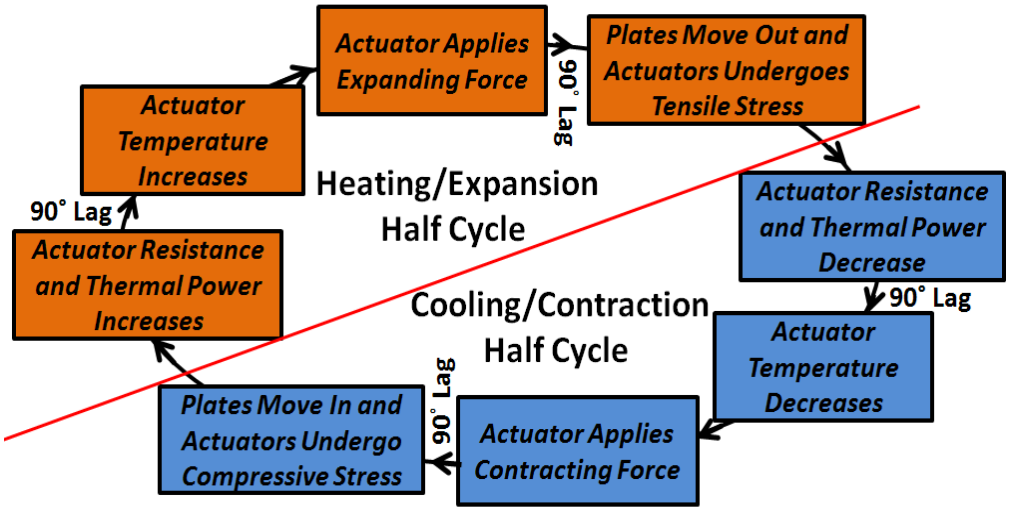

Figure 5.9. Sequence of phenomena leading to an internal positive feedback loop in thermal-piezoresistive resonators biased with a constant current that enables self-sustained oscillation.

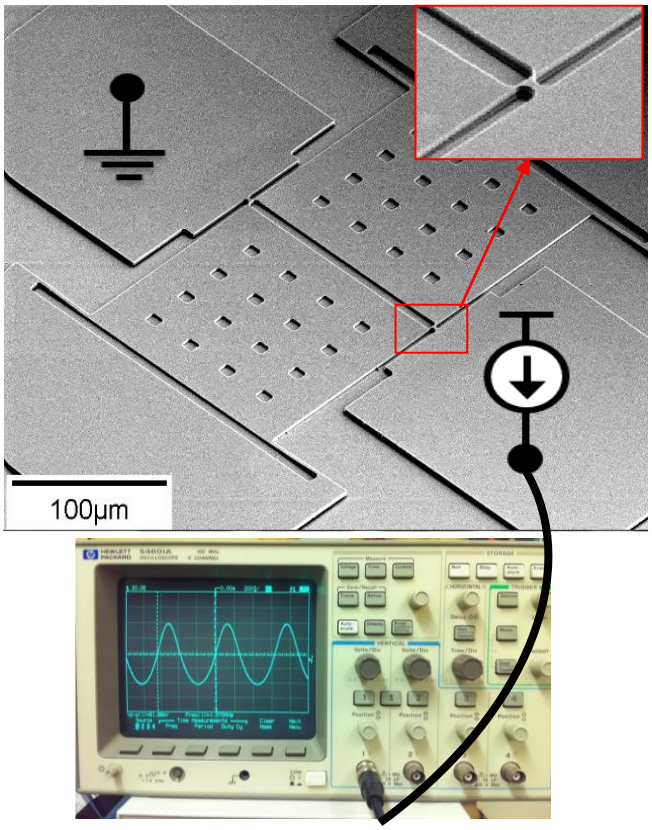

Figure 5.10. SEM view and output signal of a self oscillating 1.57MHz 3.1µm thick thermal-piezoresistive resonator. Only a DC bias current of 16.3mA is being applied to the resonator (no amplifier).

However, the piezoresistive coefficient of silicon also reduces at higher doping levels [31] necessitating further current increase to reach the required motional conductance. Therefore, temperature compensation via doping of thermal-piezoresistive oscillators generally leads to higher power requirement for self-sustained oscillation. Without optimization of resonator shape and dimensions, the required power could be well above the maximum ohmic power loss that the actuator beams can tolerate.

Figure 5.10 shows the SEM view of one of the fabricated resonators. The standard single mask process [24] was used to fabricate the resonators on a low resistivity N-type SOI substrate with device layer thickness of 3μm and buried oxide layer (BOX) thickness of 5μm.

To observe self-sustained oscillation, only a DC bias current was applied to the resonators. When the bias current reaches a specific level, the resonator initiates self-sustained oscillation and a sinusoidal wave emerges on the oscilloscope.

5.4.1. Temperature Drift Measurement Results

Temperature induced frequency drift of the oscillators were measured by placing them in a temperature controlled oven and drifting the temperature while monitoring their resonant frequency using a frequency counter. The blue plot in Fig. 5.11 shows the measured temperature induced frequency drift for an uncompensated 2.0MHz self-sustained oscillator showing a TCF of -37.9ppm/ºC.

To investigate the effect of high phosphorous doping on such oscillators, a similar 2.3MHz device was doped at 950ºC for 2 hours using a solid phosphorous source

followed by 1 hour of annealing at 1100ºC. The measured temperature drift behavior for this oscillator is shown by the red plot in Fig. 5.11 revealing a TCF of +0.41ppm/ºC.

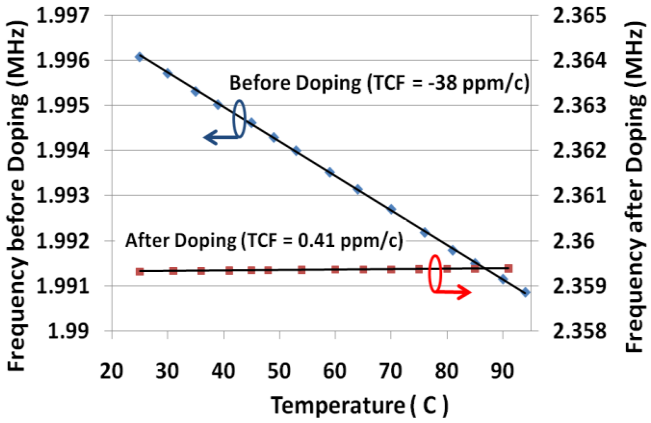

Figure 5.11. Measured temperature drift characteristics for two similar self-oscillating resonators with and without high phosphorous doping. The TCF for the doped resonator has decreased from -38ppm/ºC to 0.41ppm/ºC.

Figure 5.12 shows the measured temperature characteristics of the 1.57MHz resonator on the same doped sample operated at three different bias currents. The measured TCF has slightly different values at different bias currents showing that the oscillator TCF can be tuned by changing the DC bias current value.

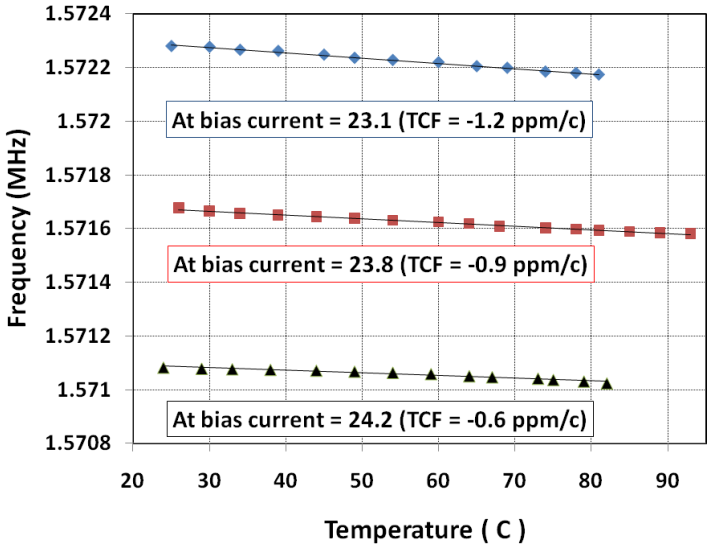

Figure 5.12. Temperature drift characteristics for the highly N-doped 1.57MHz self-oscillating resonator measured with different bias currents. Temperature stability improves as bias current increases.

Higher bias current values lead to less negative (or more positive) TCF that should be due to the higher static temperature of the actuator beams at higher bias currents.

Although the resonator of Fig. 5.10 did not survive a large enough bias current to further minimize its TCF, this data along with the fact that positive TCF is achievable for such devices (e.g. in Fig. 5.11), suggests that using optimized designs and doping concentrations, TCF much closer to zero is achievable using appropriate doping level and optimized bias currents.

Table 5.2 summarizes measured TCF values for a number of different temperature compensated oscillators.

Table 5-2 Measured TCF and other characteristics for different temperature compensated self-oscillating resonators.

Resonator Dimensions(μm)		**Freq. (MHz)**	**$V_{p\text{-}p}$ (mV)**	**I_{bias} (mA)**	**R_{DC} (Ω)**	**P_{DC} (mW)**	**TCF ppm/ºC**
a L W	**L_b W_b DL**						
197 24 0.5	58.5 3.5 3.1	1.571	78	23.1	44	23.6	-1.2
			82	23.8	44.7	25.5	-0.9
			83	24.2	45	26.6	-0.6
197 8 0.5	52 3.4 3.1	2.359	133	57.1	36.8	119	0.41
97 24 0.5	39.5 3.5 3.1	4.233	146	10.2	75	7.8	1.2

Therefore temperature compensated single-device electromechanical oscillators with temperature drift as low as 0.4ppm/ºC were demonstrated. N-type single crystalline silicon thermal-piezoresistive resonators capable of self-sustained oscillation were used as frequency references. Temperature compensation was achieved via high concentration phosphorus doping. It was shown that much better temperature stability could be

obtained by optimizing the doping level and bias current for such devices potentially leading to zero TCF single-device MEMS frequency references.

6. FREQUENCY TRIMMING AND FREQUENCY TUNING OF THERMAL PIEZO-RESISTIVE MEMS RESONATORS

The resonance frequency of silicon micromechanical resonators is dependent on the physical dimensions of the resonating structure. Process variations across the substrate (e.g Non-uniformities in photolithography, etching and film thickness) leading to variations and mismatch in the mechanical resonant frequencies are a major challenge for batch fabrication of micromechanical resonators. Post-fabrication trimming is one of the ways to solve this issue. The post frequency trimming methods make one-time permanent changes to the frequency of the devices. Different frequency trimming techniques for MEMS silicon based micromechanical resonators have been presented. The techniques range from pulsed-laser-deposition/trimming [44,45], gold diffusion into the bulk of the resonator [46] and localized thermal oxidation which we will present in parts of this chapter [47].

There are other frequency adjustments methods known as frequency tuning, that make active frequency changes without permanent changes to the structure of the micro-resonator. On the active frequency tuning side, several basic methods have previously been investigated. The first of the methods, tunes by making changes in the internal stresses of the structure to induce changes in resonance [48]. Another active frequency

tuning technique is to take advantage of the inherent temperature dependence of Young's modulus [49]. Tuning via an electrostatic stiffness change, where the stiffness can be adjusted electrostatically with capacitive structures has also been used as common frequency tuning method [50].

6.1 Localized Thermal Oxidation for Frequency Trimming and Temperature Compensation of Micromechanical Resonators

Figure 6.1 shows the COMSOL finite-element thermal analysis of an I-shaped resonator while applying a dc current. Static temperature of the structure resulting from the dc bias current is much higher in the middle of the structure where the actuator beams are located. Therefore as thoroughly explained in the measurement setup and results section, oxygen will be formed on the hot actuator surfaces in the middle of the structure when heated to high temperatures. Figure 6.2 shows the SEM view of a 4μm thick 53MHz I-shaped resonator which was fabricated on an N-type low resistivity SOI substrate with a buried oxide layer (BOX) thickness of 5μm.

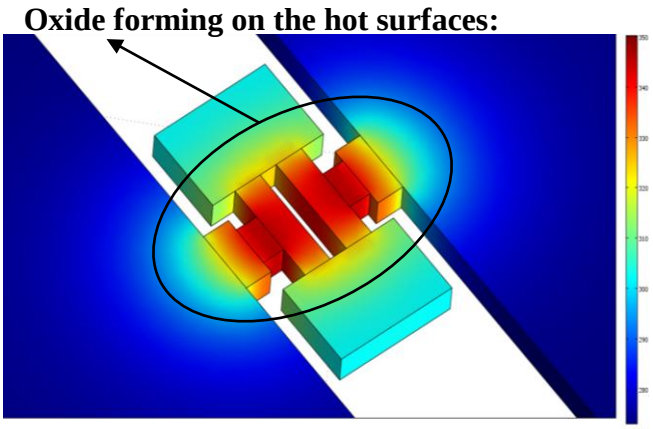

Figure 6.1. Three-dimensional schematic view of a thermally actuated I-shaped resonator. The actuators in the middle of the structure have a much higher temperature and therefore oxide forms on the surface of actuators.

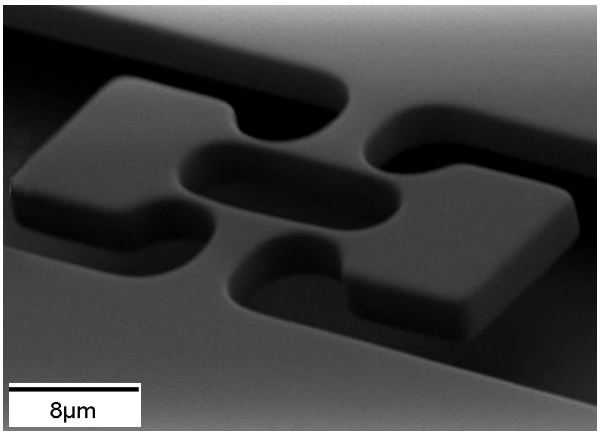

Figure 6.2. SEM view of a 53MHz, 4μm thick thermal-piezoresistive I-shaped resonator. The resonator is fabricated on a low resistivity (~0.01Ω.cm) N-type SOI substrate using a single mask process.

6.1.1 Measurement Setup and Results

Figure 6.3 shows the schematic diagram of the test setup used for performing the localized thermal oxidation process.

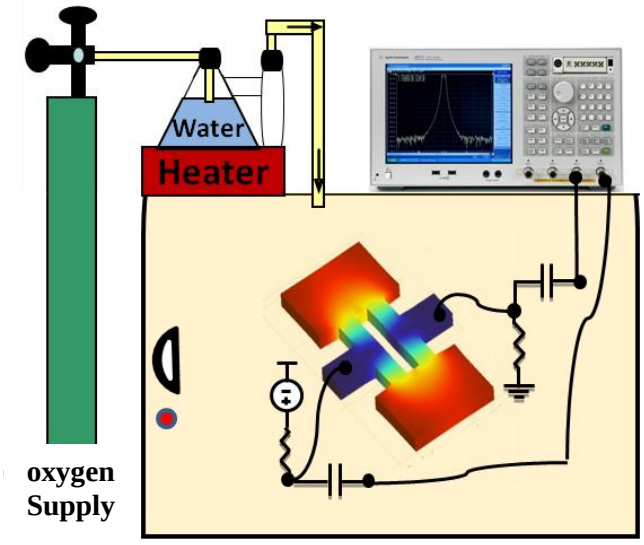

Figure 6.3. Schematic diagram of the measurement setup used in this experiment. Moisture rich oxygen was driven into the chamber while the device was biased at a high current (the beams were red). Measurements were performed by a network analyzer.

The resonators were placed in a chamber while connected to the test setup. Moisture rich oxygen was delivered into the chamber through an inlet tube to provide a suitable atmosphere for wet oxidation of silicon.

The localized oxidation and therefore frequency trimming starts by application of a relatively large current, more than what is typically required for operation of the device (the actuator beams visibly turned red on the silicon substrate) . When the large bias current passes through a resonator structure, joule heating caused by ohmic losses raises the temperature of the structure. At the same time as the forming of the oxide on the resonator structure, the frequency of the resonator was monitored by a network analyzer. Figure 6.4 shows the change in the measured resonance frequency for the 53MHz resonator of Figure 6.2 over time, during 4 oxidation steps.

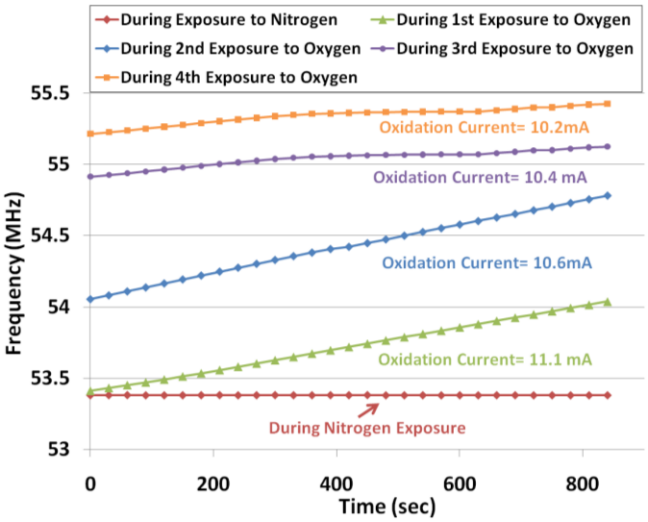

Figure 6.4. Change in the measured resonance frequency for the 53MHz resonator as a function of the exposure time during 4 oxidation steps showing an overall frequency shift of ~2MHz. No frequency shift is recorded when the resonator was exposed to nitrogen.

An overall frequency shift of ~2MHz was observed. However it can be seen here, that the slope of the changes decreased at the last steps which is due to the oxidation thickness reaching saturation. In order to prove the concept of change in frequency being caused by thermal oxidation of the resonator, the same self heating procedure was earlier performed in a nitrogen atmosphere. This time there was no frequency shift observed and

throughout the whole process time, the frequency of the resonator remained constant.

Another set of interesting data that was collected was with regard to the resonator temperature drift. Figure 6.5 shows the temperature drift characteristics of the same resonator measured before and after each of the oxidation steps. Silicon resonators typically exhibit temperature coefficient of frequency (TCF) in the -20 to -40ppm/ºC range [14]. Figure 6.5 shows that while the initial TCF for this resonator was measured to be -37 ppm/ºC, it has gradually increases after each oxidation step. This increase in TCF is due to the formation and thickening of the SiO_2 film (which has a positive temperature coefficient of Young's modulus) on the surface of the resonator. Thus, the potential of achieving highly suppressed temperature drifts is also demonstrated.

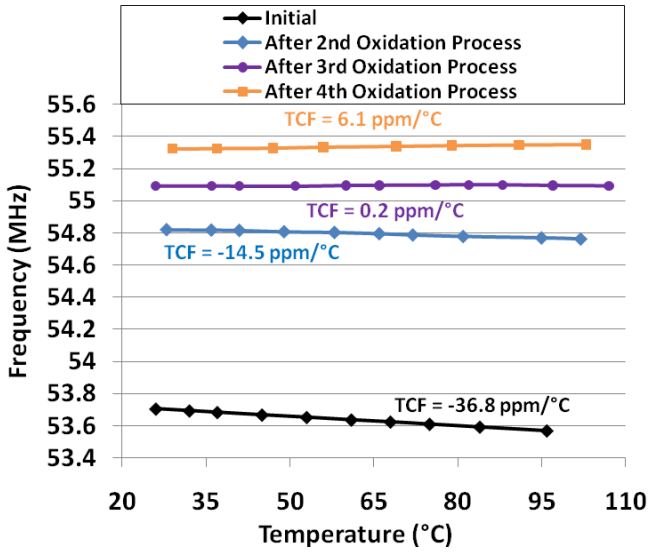

Figure 6.5. Temperature drift characteristics for the 53MHz resonator of Fig.6.2 measured before and after each of the oxidation steps. The TCF becomes more positive (less negative) after each step due to the formation and thickening of SiO2 on the surface of the actuators.

Figure 6.6 depicts the measured resonance frequency of the same resonator, at different bias currents. Different plots show data taken after different localized oxidation runs, at room temperature and after the oxygen source was removed and bias current decreased.

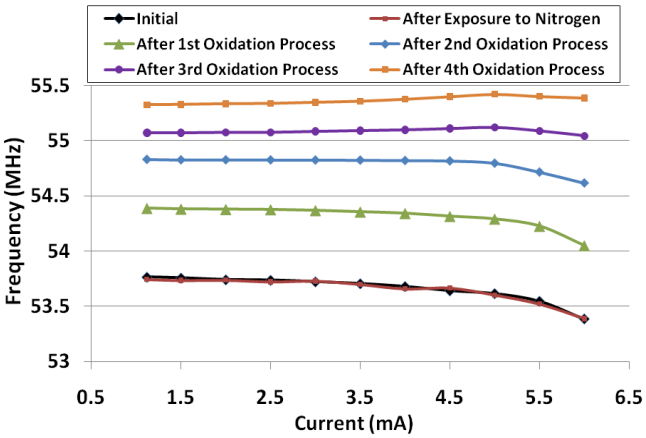

Figure 6.6. Measured resonance frequency of the 53MHz resonator of Fig. 6.2, at different bias currents. Different plots show the data taken after different localized oxidation runs at room temperature when the oxygen source was removed. As can be seen from the graph, the flow of nitrogen has had no effect on the resonant frequency, whereas after each oxidation process, the resonance frequency has increased.

The slope of the frequency curve has gradually increased after each oxidation step even turning positive after the 4th oxidation step (due to TCF reduction). Again it can be seen that exposure to nitrogen has not caused any shift in the resonance frequency.

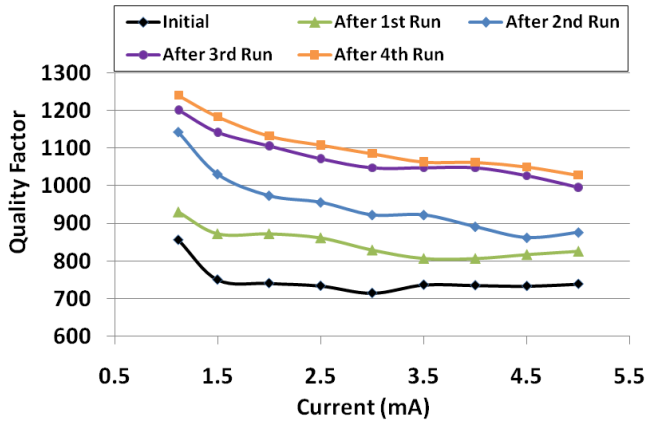

Figure 6.7. Measured quality factor of the same resonator at different bias currents after each oxidation step. The quality factor has slightly increased after each step.

Figure 6.7 depicts the measured quality factor of the 53MHz resonator at different bias currents. After each oxidation step, the quality factor has not only not degraded, but slightly increased, which could be explained by the possible increase in the stiffness of

the resonator structure.

Table 6.1 shows measurement results from two different devices after exposure to vapor rich oxygen in several steps as well exposure to nitrogen in a single step. The permanent change in the resonator frequency after each step is shown.

Table 6-1 Measured frequency changes for two I-shaped resonators of different dimensions, during several steps of exposure to moisture rich oxygen.

Resonator Dimensions(μm)	**Initial Freq. (MHz)**	**Freq. Shift (kHz), after :**				
		Oxygen exposure				**Nitrogen exposure**
a, b, L, W, H		**1st Run**	**2nd Run**	**3rd Run**	**4th Run**	
15, 10, 12, 1.2, 3	53.3	626	728	210	208	0.02
31, 21, 15, 1.2, 3	31.9	318	290	283	245	0.02

6.2 A Self-Controlled Frequency Trimming Technique for Micromechanical Resonators

This section shows preliminary measurement results for a more advanced version of the same localized oxidation based trimming approach with the potential ability to automatically limit itself.

As opposed to the previous section in which a DC current was applied, in this method localized oxidation is induced by applying an AC voltage $\left(V_{ac}cos(2\pi f_a t)\right)$ (Figure 6.8a) across the structure. The generated power has a square relationship with the applied voltage and gives birth to two frequency components at DC and twice the actuation frequency ($2f_a$):

$$P = \frac{{v_{ac}}^2 \cos^2(2\pi f_a t)}{R_A} = \frac{{v_{ac}}^2}{2R_A} + \frac{{v_{ac}}^2 \cos(4\pi f_a t)}{2R_A} \tag{6.1}$$

where R_A is the electrical resistance of the resonator and f_a is the actuation frequency. The resulting power translates to elevated temperature of the thermal actuators. It can be shown that the AC temperature term is proportional but also has a 90º lag in comparison to the AC power [1]. The resulting fluctuating temperature causes a thermal stress and therefore an alternating mechanical force inside the thermal actuators. If this applied force has the same frequency as the resonance frequency of the resonator, it actuates the device. In order for this to happen, the frequency of the actuation voltage should be half of the mechanical frequency. The resulting mechanical vibration of the resonator has a 90º lag with respect to the mechanical force [1]. The mechanical vibration leads to resistance fluctuations of the resonator due to the piezoresistive effect. The AC value is proportional and in phase with the mechanical vibration. Therefore this AC term which adds to the electrical resistance of the device has a 180º lag with respect to the applied actuation current due to thermal and mechanical delays. For N-type silicon the piezoresistive coefficient is negative which itself adds a 180º lag. Thus, the resistance fluctuation is in phase with the applied voltage (blue plot in Figure 6.8b) and this leads to the overall resistance of: $R_A + r_{ac}\cos\left(2\pi\, f_0 t\right)$. As a result the ohmic power in the structure will be:

$$P = \frac{{v_{ac}}^2 \cos^2(\pi\, f_0 t)}{R_A + r_{ac}\cos\left(2\pi\, f_0 t\right)} = \frac{{v_{ac}}^2\left(1+\cos\left(2\pi\, f_0 t\right)\right)}{2\left(R_A + r_{ac}\cos\left(2\pi\, f_0 t\right)\right)} \tag{6.2}$$

The r_{ac} value itself is equal to:

$$r_{ac} = \frac{R_A\left|\pi_l\right|Ex_m}{L} \tag{6.3}$$

where π_l is the longitudinal piezoresistive coefficient, E is the young's modules, L is the length of the thermal actuator and x_m is the vibration amplitude. The DC component of Eq.2 can be found to be equal to:

$$P_{DC} \cong \frac{v_{ac}^{\ 2}}{2\left(R_A + r_{ac}\right)} \tag{6.4}$$

By comparing the DC power consumptions in the two different states of off-resonance (DC part of Eq. 6.1) and at-resonance (Eq. 6.4), it is obvious that at-resonance state the power consumption goes down (Figure 6.8c). Therefore, during resonance the static temperature decreases (Figure 6.8d). This difference in temperature between the two cases of at-resonance and off-resonance can be utilized for self controlled trimming of the structures.

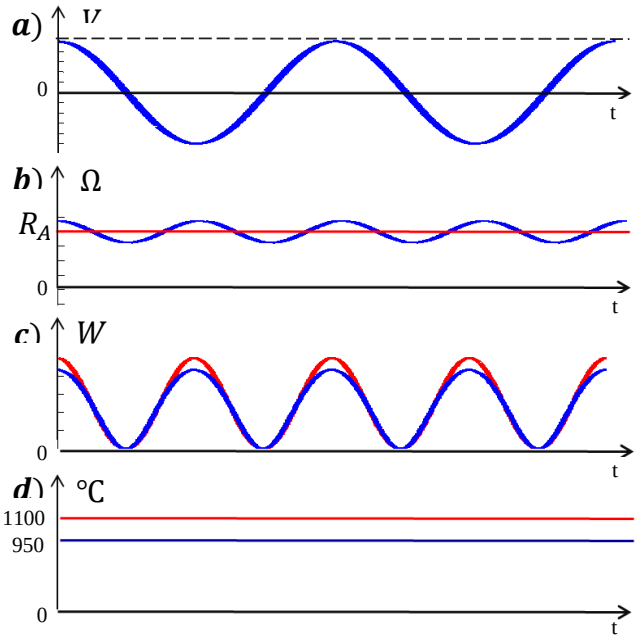

Figure 6.8. Waveform representation of a) Input AC voltage, b) Resistance of the resonator, c) Ohmic loss and d) Temperature in both conditions of off-resonance (red) and at-resonance (blue). It is assumed that $r_{ac}=0.15R_A$. Therefore, the DC power consumption drops 14% during resonance with respect to its off-resonance mode. As a result assuming the initial static temperature of 1100℃, temperature decreases to 950℃.

Figure 6.9 schematically depicts the proposed self-controlled electronic frequency trimming technique for micromechanical single crystalline silicon resonators. Half the desired frequency is applied with sufficient amplitude to allow the actuators to reach the temperatures required for oxidation.

As the oxidation process starts, the internal stress of the thermal actuators changes. This causes the resonance frequency of the resonator to gradually change and become closer to the desired resonance frequency. The process goes on until the resonance frequency of the resonator exactly matches the desired resonance frequency. At this point, the resonator starts vibrating and therefore the overall resonator static temperature drops significantly which could stop the local oxidation. In order to investigate the feasibility of this technique, assuming large vibration amplitudes and large piezoresistive coefficients, r_{ac} can become comparable with $R_{DC.}$ For instance, with a conservative piezoresistive coefficient of ($-10\times10^{-11}Pa^{-1}$), and vibration amplitude of 100x smaller than the actuator length, $r_{ac} = -0.15R_A$. In this case the value of P_{DC} at resonance becomes 14% less than its value out of resonance. This translates to a 14% reduction of the actuator static temperature difference from the surroundings. For instance, a resonator heated up to 1100ºC by the applied currents out of its resonance frequency, can cool down to about 950ºC if the actuation frequency becomes equal to its mechanical resonant frequency. Therefore, the overall resonator static temperature could drop significantly if the applied actuation AC signal has the right frequency required for excitation of the resonant mode. Sharp dependence of thermal oxidation rate on temperature can turn small temperatures changes into major changes in the oxidation rate and completely stopping it.

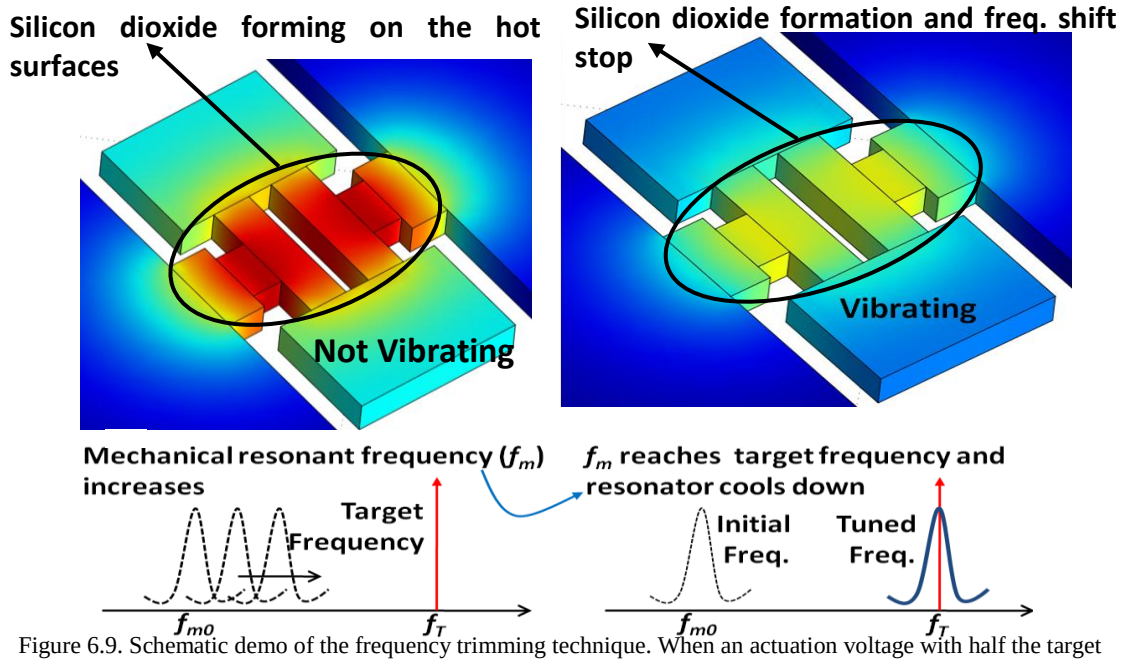

Figure 6.9. Schematic demo of the frequency trimming technique. When an actuation voltage with half the target resonance frequency is being applied across the actuator beams, the elevated temperature allows oxidation to take place on their surface. As a result, the structural stiffness gradually changes and the resonant frequency moves towards the target. When the mechanical resonant frequency reaches the target frequency, the resonator starts vibrating and therefore cools down. As a result, oxidation stops and the frequency will not shift further..

Figure 6.10 shows the schematic diagram of the test setup used for performing the localized thermal oxidation process. The resonators were placed in a chamber while connected to the test setup. Moisture rich oxygen was delivered into the chamber through an inlet tube to provide a suitable atmosphere for wet oxidation of silicon. The localized oxidation and therefore frequency trimming starts by application of a large amplitude AC voltage applied through the structure using a function generator. After this localized oxidation run, the devices were disconnected from the AC voltage source and were tested at room temperature using a network analyzer.

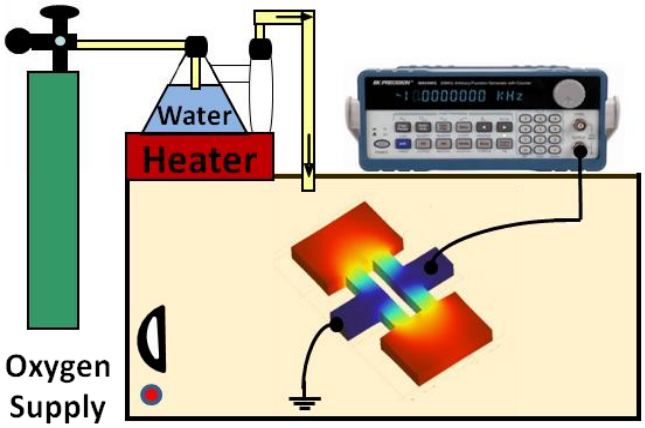

Figure 6.10. Schematic diagram of the setup used in this experiment. Moisture rich oxygen was driven into the chamber while a sinusoidal ac current was run through the device.

Figure 6.11 shows the change in the measured resonance frequency after different oxidation steps, for an 18MHz resonator. Different plots show data taken after localized oxidation runs via actuation by AC voltage with both off-resonance and at-resonance frequencies.

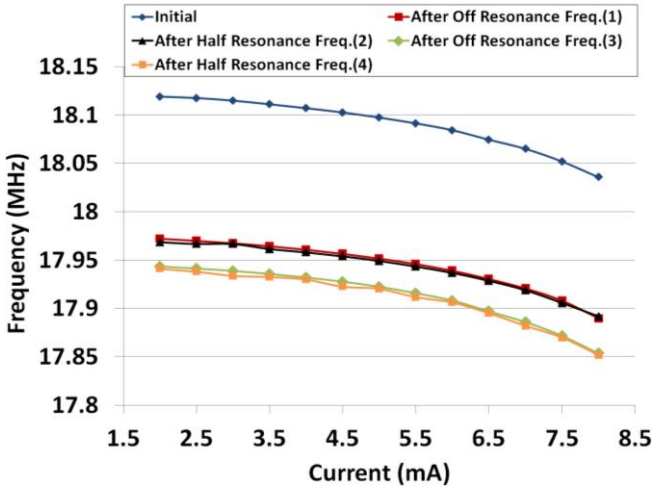

Figure 6.11. Measured resonance frequency of the 18MHz resonator of figure 1, at different bias currents. Different plots show the data taken after different localized oxidation runs at room temperature when the oxygen source was removed. As can be seen from the graph, the actuation at half the resonance frequency has had no effect on the shift in resonant frequency (steps 2 and 4), whereas each time the resonator was actuated at an off-resonance frequency, the resonance frequency has decreased.

It has been shown through 4 consecutive oxidation periods with alternating off/at resonance signals applied to the device that the cooling effect is occurring. Off-resonance

oxidation which has been applied in steps 1 and 3 has led to changes in the resonator frequency, whereas in steps 2 and 4 it is shown that when the excitation causes mechanical resonance, it results in almost no oxidation (no frequency trimming).

Another set of interesting data that was collected was with regard to the resonator temperature drift. Figure 6.12 shows the temperature drift characteristics of the same resonator measured before and after each of the oxidation steps.

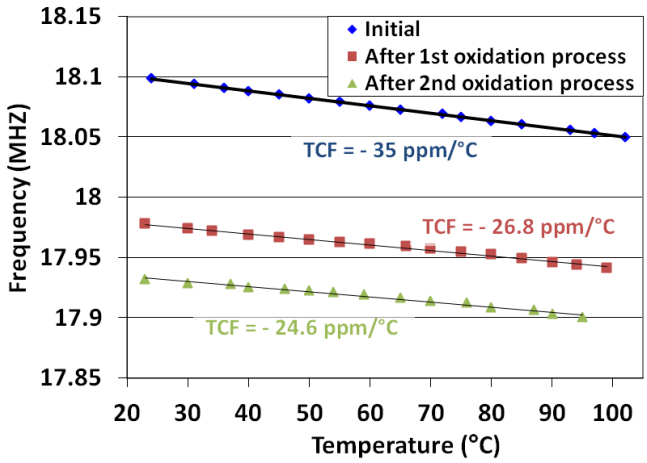

Figure 6.12. Temperature drift characteristics for the 18MHz resonator of figure 1 measured before and after each of the oxidation steps. The TCF becomes more positive (less negative) after each step due to the formation and thickening of SiO_2 on the surface of the actuators.

6.3 Electrostatic Frequency Tuning of Thermal Piezo-Resistive MEMS Resonators

The finite element modal analysis result showing the resonant mode shape for a 7.8MHz dual plate resonator in its in-plane extensional mode is shown in Figure.6.13. Red and blue colors show locations with the largest and smallest vibration amplitudes respectively. At resonance the two plates move back and forth in opposite directions causing the narrow actuator beams to expand and compress periodically. The 4 support

beams on the outer corners of the plates are to increase the vertical stiffness of the structure and avoid stiction of the plates to the handle layer during device fabrication.

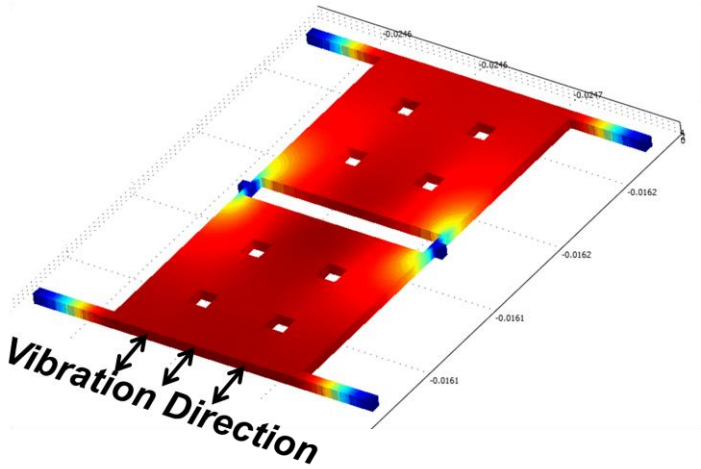

Figure 6.13. COMSOL modal analysis, showing the in-plane resonance mode shape of interest for a 7.8MHz dual-plate resonator. The two plates move back and forth in opposite directions while the narrow actuator beams undergo periodic compression and extension. Red and blue colors show locations with the largest and smallest vibration amplitudes respectively.

Fig. 6.14 shows the SEM view of a fabricated 7.8MHz dual-plate resonator along with its electrical connections. Thermal actuation of the device occurs by passing a fluctuating electrical current through the actuator beams in the middle of the structure. The AC force generated in the pillars as a result of the fluctuating temperature and therefore alternating thermal stress in the pillars, can actuate the resonator in its in-plane resonant mode. At resonance, the resistance of the pillars will be modulated by the resulting alternating mechanical stress due to the piezoresistive effect that results in a detectable small signal motional current in the device. In order to be able to actively change the frequency of the resonator, a separate DC voltage is applied to the underlying SOI substrate handle layer. The electrostatic force resulting from the DC tuning voltage will slightly move the plates in the out of plane direction and causes a change in the resonance frequency.

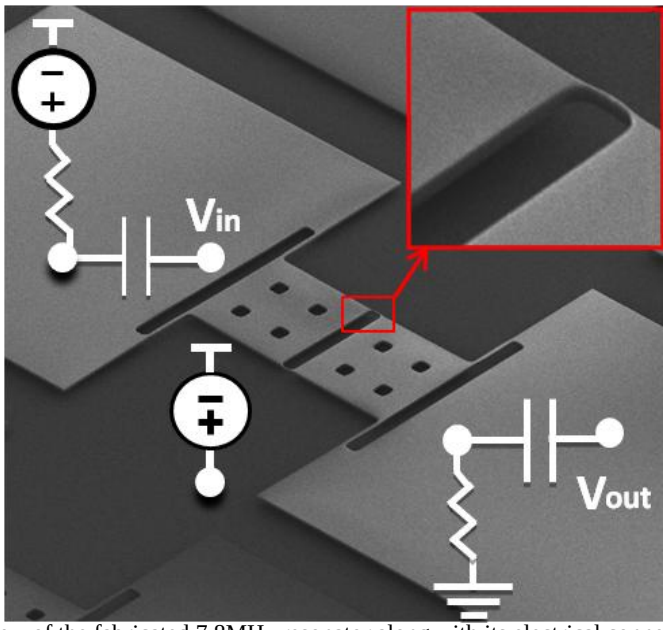

Figure 6.14. SEM view of the fabricated 7.8MHz resonator along with its electrical connections. For thermal actuation a combination of DC and AC current are driven through the device. A separate DC voltage is applied to the device handle layer for electrostatic tuning.

6.2.1 Measurement Setup and Results

One of the known sources of energy loss in micromechanical resonators is air damping that happens when a body of resonator plate is moving near a stationary body or surface. In our case the resonator plates are moving back and forth in the in-plane lateral direction while trapping air between the underlying stationary silicon surface of the handle layer. It is expected that due to the stress in the SOI substrate (mainly caused by the BOX layer), the device structure is initially bent upwards as can be seen in Fig. 6.15a.

Once a DC voltage is applied to the substrate, the electrostatic force between the substrate and the plate causes the plate to bend downwards.

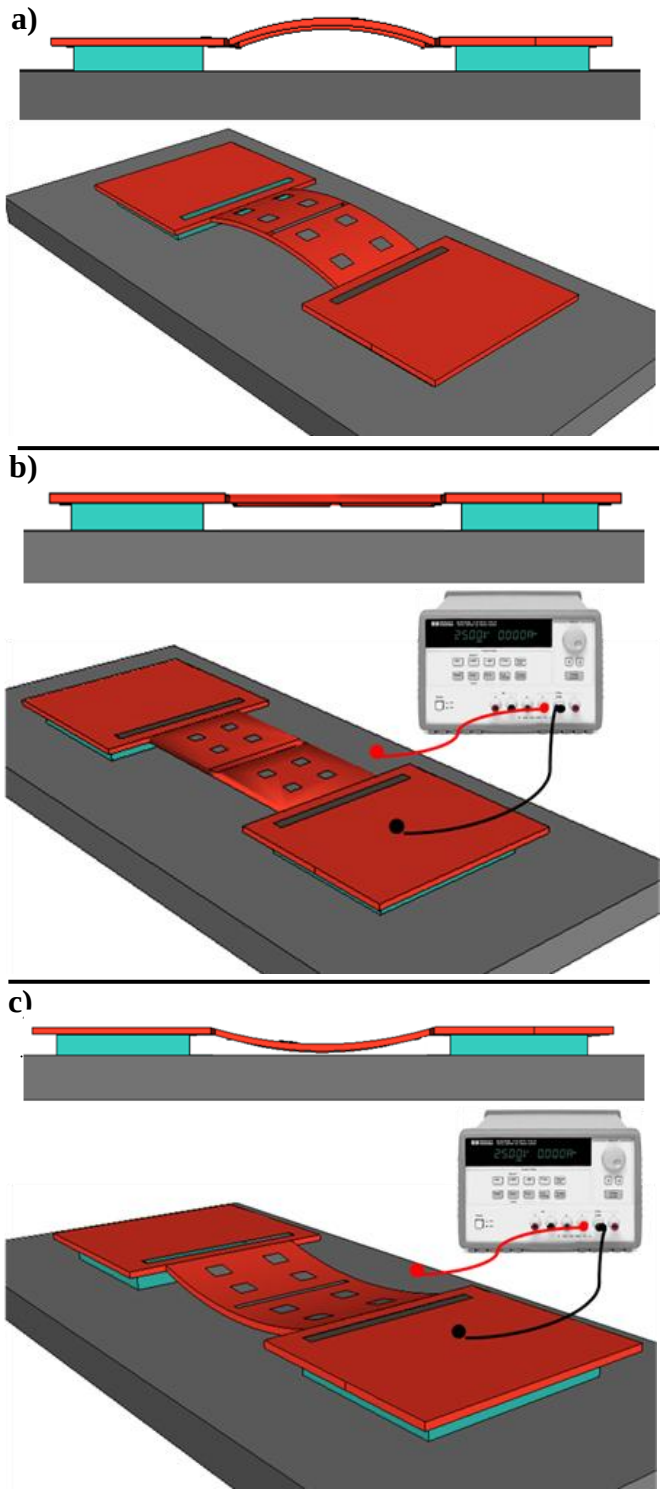

Figure 6.15. Cross sectional and 3D schematic diagram of the structure of the in-plane thermal piezo-resistive micro-electromechanical resonators. It shows the position of the resonators with regard to the underlying handle layer substrate. a) Due to the stress in the SOI substrate (mainly caused by the BOX layer), the device structure is initially bent upwards. b) Once a DC voltage is applied to the substrate, the electrostatic force between the substrate and the plate causes the plate to bend downwards. When the plates are bent downward and are fully horizontal. c) At higher voltages the resonator plates start bending downwards even more causing it to be bent in the opposite direction.

When the plates are bent downward and are fully horizontal as shown in Fig. 6.15b, Q factor is maximized due to minimized air damping (fully horizontal shearing motion). At higher voltages the resonator plates start bending downwards even more and there will be opposite curvature in comparison to the initial position of the plates as shown in Fig. 6.15c. Therefore the Q factor drops again due to increased air damping. It should be noted that when operating under low vacuum, the dominant source of resonator damping is still air-damping and therefore the same effect can be observed. Fig. 6.16 shows the measured change in quality factor of the resonator in both air and low vacuum versus the applied tuning voltage.

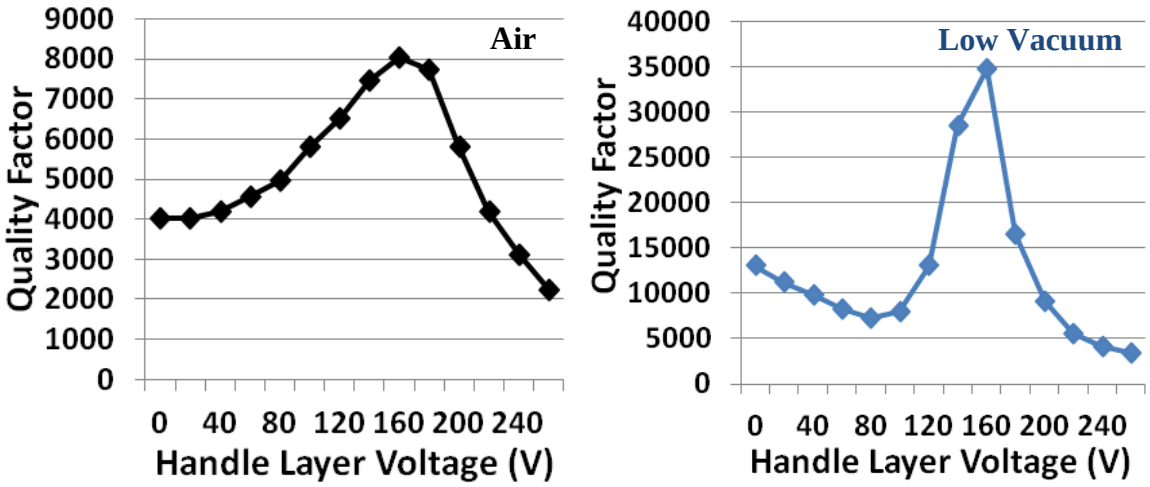

Figure 6.16. Measured changes in quality factor versus the applied tuning voltage. The left graph is measurement taken in air and the right graph is in partial vacuum (~70 Torr). In both cases by adjusting the handle layer voltage, Q factor has almost doubled.

Fig. 6.17 shows the measured change in frequency of the resonator in both air and low vacuum versus the applied tuning voltage. In both occasions the resonance frequency initially decreases reaching a minimum and then starts increasing. As talked about earlier, due to stress in the SOI substrate, the device structure is initially slightly bent upward. The electrostatic force resulting from the DC tuning voltage initially pulls the device layer

down canceling out the bending of the structure and therefore causing a decrease in the resonance frequency. If the DC tuning voltage is further increased, the plate is bent downwards and the frequency this time increases in the opposite direction. The frequency tuning shows a maximum tuning range of -430 ppm and +580 ppm in negative and positive directions of the frequency spectrum respectively.

The BOX thickness for this specific SOI substrate was 5µm leaving behind a relatively wide electrostatic tuning gap between the handle layer and the device. Much higher tuning ranges and lower tuning voltages are expected to be achievable by fabricating the resonators on SOI substrates with thinner BOX.

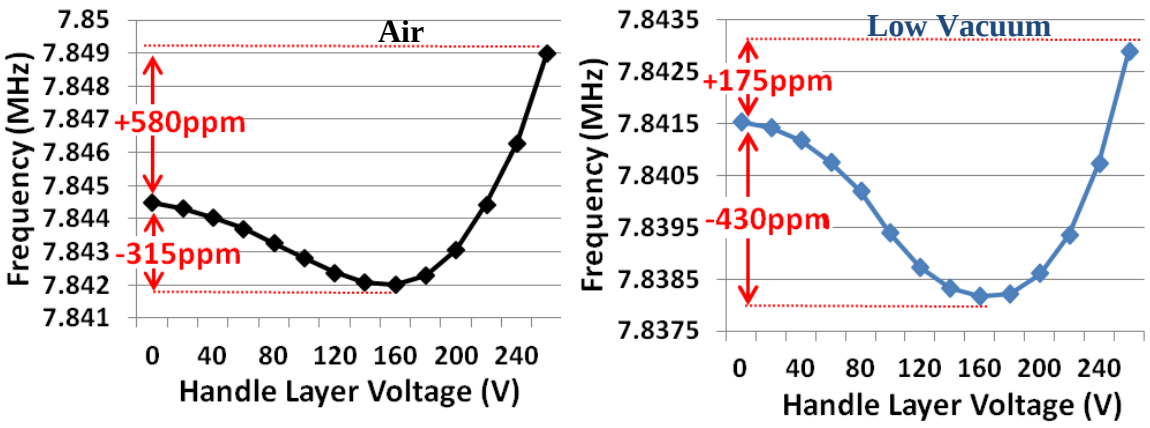

Figure 6.17. Measured changes in frequency versus the applied tuning voltage. The top graph is measurements taken in air and the bottom graph is in partial vacuum (~70 Torr). In both cases by adjusting the handle layer both positive and negative frequency tuning is obtained.

Therefore, here we presented an active frequency tuning mechanism has been proposed and has been proven to adjust the resonance frequency of in-plane thermal piezo-resistive micro-electromechanical resonators. Frequency tuning is experimentally carried out in both air and low vacuum by applying a electrostatic force on the device substrate. The frequency tuning shows changes in both directions of the frequency spectrum achieving a maximum tuning range of +580 ppm and -430 ppm in positive and

negative directions of the frequency spectrum respectively. Moreover, the performances of the tuned resonators, has shown an improvement in terms of the quality factor.

7. HIGH FREQUENCY THERMAL-PIEZORESISTIVE MEMS RESONATORS FOR DETECTION OF ORGANIC GASES

Highly sensitive and low-cost organic gas sensors have a number of applications mainly in the oil and gas industry. Examples include early detection of gas leaks and rapid on-site determination of organic content of oil sands. Achieving a high level of selectivity and specificity between different volatile organic compounds (VOC) could be a challenging chemical design issue. However, in most of the targeted applications in oil and gas industry the composition of the compound(s) of interest is somewhat known and constant and the information of interest is their concentration in surrounding air. Most carbon-based polymers have a tendency to absorb organic molecules in the gas phase. Coating a microscale resonator with such polymers will turn the device into a mass balance responding to the concentration of surrounding gas molecules.

Most of the VOC sensors demonstrated in the literature are based on either conductivity change in a thin film, or resonance frequency change in a mechanical resonator. Conductivity based sensors utilize carbon nanotubes [51,52] or conductive polymers [53,54]. Sensing based on resonant frequency shift generally provides more precision as the effect of noise in direct voltage or current measurement is highly suppressed in frequency measurements. A variety of VOC sensors using surface acoustic wave (SAW) [55,56], quartz crystal microbalance (QCM) [57,58], and micro electromechanical (MEMS) resonators [59-61] have previously been demonstrated. The miniaturized MEMS resonators can be batch fabricated as individual devices or arrays at

a very low cost and due to their much smaller size, they can provide orders of magnitude higher sensitivity and resolution compared to bulky quartz [57,58] and SAW [55,56] resonators. Electrostatic (capacitive) MEMS resonant chemical/gas sensors [59-61], some of which are integrated within a CMOS process [60,61] have previously been demonstrated. For such devices deposition of the chemically sensitive layer used for the detection of VOC is performed by dispensing, spray coating, or drop coating. One of the potential bottle necks for this type of device could be the penetration of the polymer coating inside the air-gaps of the resonator. The polymer residues could cause the air-gaps to clog up and therefore degrade the performance of this type of resonant sensor and even leave them non-operational. Piezoelectric MEMS resonators have also been used for gas sensing purposes through which mass sensitivities in the order of hundred picograms equivalent to minimum detectable gas concentration of few ppm has been achieved [62,63].

Thermally actuated resonators, as the third group of MEMS resonant sensors, are extremely simple to implement without fabrication challenges or the need for integration of different materials as needed for piezoelectric resonators. The simple monolithic structure of thermal-piezoresistive resonators makes them very robust for sensory applications where the resonator needs to be in contact with the surrounding environment [24]. This chapter presents high frequency versions of such devices capable of detection and concentration measurement of VOC in gas phase.

The resonators in this work are coated with the shipley-1813 photoresist whose main polymer ingredient is polyglycolic acid. Figure 7.1 shows both the two-dimensional

and three-dimensional structure of this non-conductive polymer which is both biodegradable and thermoplastic in nature [64].

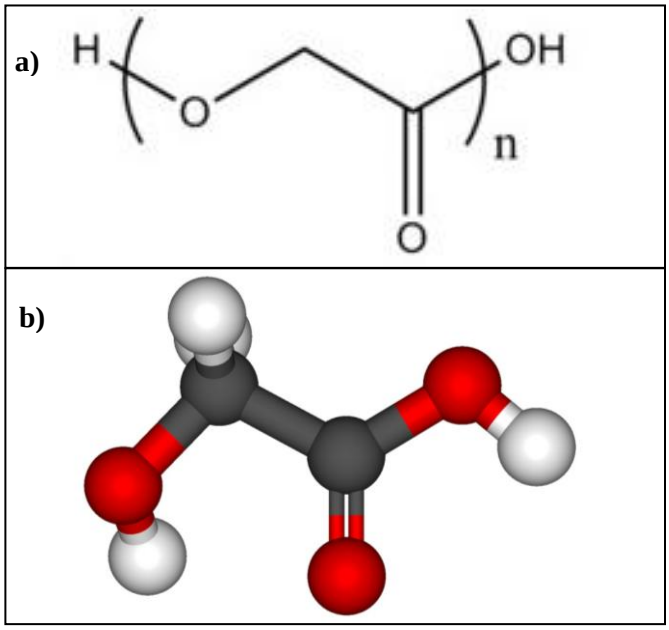

Figure 7.1. a) Two-dimensional and b) Three-dimensional schematics of the compound structure of polyglycolic acid which is the main polymer ingredient of the shipley-1813 photoresist that was used as the absorbent coating layer.

7.1 FABRICATION AND COATING PROCESS

The standard single mask silicon on insulator (SOI) MEMS process was used for fabrication of the thermal-piezoresistive resonators used in this work [25]. This process starts by growing a thin (~200 nm) layer of silicon dioxide on the substrate. The silicon dioxide layer is patterned to define the resonator structures. The silicon structures are then carved into the SOI device layer by deep reactive ion etching (DRIE) of silicon all the way down to the buried oxide (BOX) layer. Finally, the underlying buried oxide is removed in hydrofluoric acid (HF). At the same time the remaining oxide mask on top of the structures is also etched away. The whole procedure is shown in steps a to c of Figure 7.2.

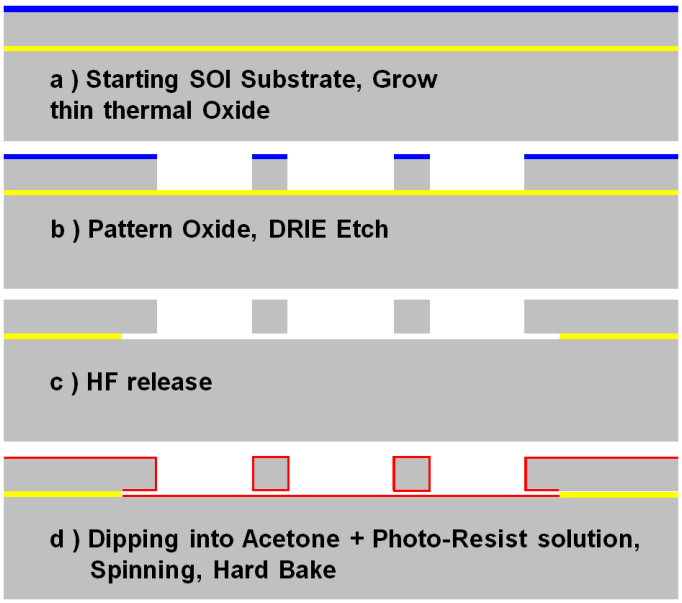

Figure 7.2. a-c) Thermally actuated resonator fabrication process flow and d) polymer coating.

In multiple studies, in order to examine the ability of high frequency crystalline silicon thermal-piezoresistive resonators as VOC sensors, the devices were coated using three different techniques: 1) coating the devices after release from the buried oxide layer (BOX) layer [65], 2) coating the devices before release [66], and 3) using the polymer already present from the fabrication stage [67] to collect the gas molecules. All three methods used the shipley-1813 photoresist as the absorbent coating layer and underwent the same procedure for experimentation.

Each of the sensors were exposed to either gasoline or toluene (the main component of gasoline) vapor. The frequency shift caused by the absorption of the gas vapor was measured using the network analyzer.

7.1.1. Polymer Coating after Releasing of the Structures

In the first polymer coating approach, the absorbent polymer layer was formed on the resonators sensing pads by dipping them in a dilute solution of the shipley-1813 photoresist in acetone [65]. The resonator samples were spun at 3000rpm for a few seconds to disperse the excess diluted photoresist followed by hard bake in order to get rid of the solvent (step d of Figure 7.2). This is expected to leave a thin dry layer of polymer on all silicon surfaces.

Even though the resonators prepared using this method were responding to organic gases, the sensitivity and full-range frequency shift was not very promising and a maximum frequency shift of only 200 ppm was obtained for a highly saturated gas sample.

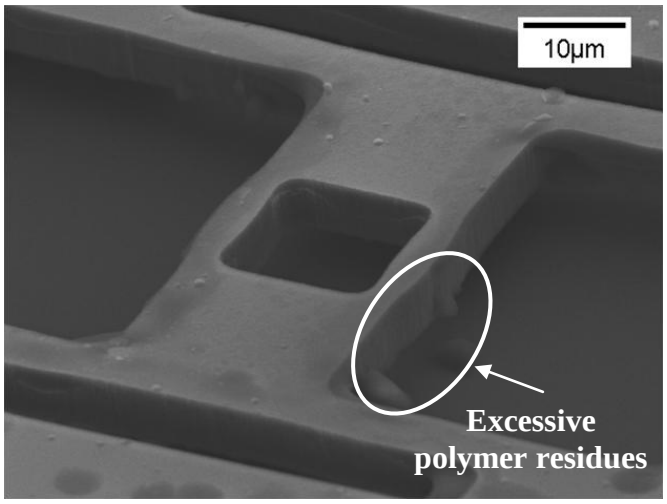

Figure 7.3. SEM view of a device in which high polymer thickness has resulted in excessive polymer residues in the gap between the resonators and the SOI handle layer which has left the devices non-operational.

The reason for such low frequency shift was the small polymer thickness on the surface of the devices due to use of a highly diluted polymer solution. Using higher concentration polymer solutions in this technique, generally results in excessive polymer

residues in the gap between the resonators and the SOI handle layer leaving the devices non-operational as can be seen in the SEM picture in Figure 7.3.

7.1.2. Polymer Coating before Releasing of the Structures

In order to prevent the resonant devices becoming non-operational due to the forming of the residues in the gap between the SOI handle layer and the resonator, a new procedure was utilized for polymer coating of the devices. Using this coating method, a thicker polymer coating was also obtained as shown in Fig. 7.4. Steps a and b which are not shown in Fig. 7.4 are identical to the fabrication process shown in Figure 7.2.

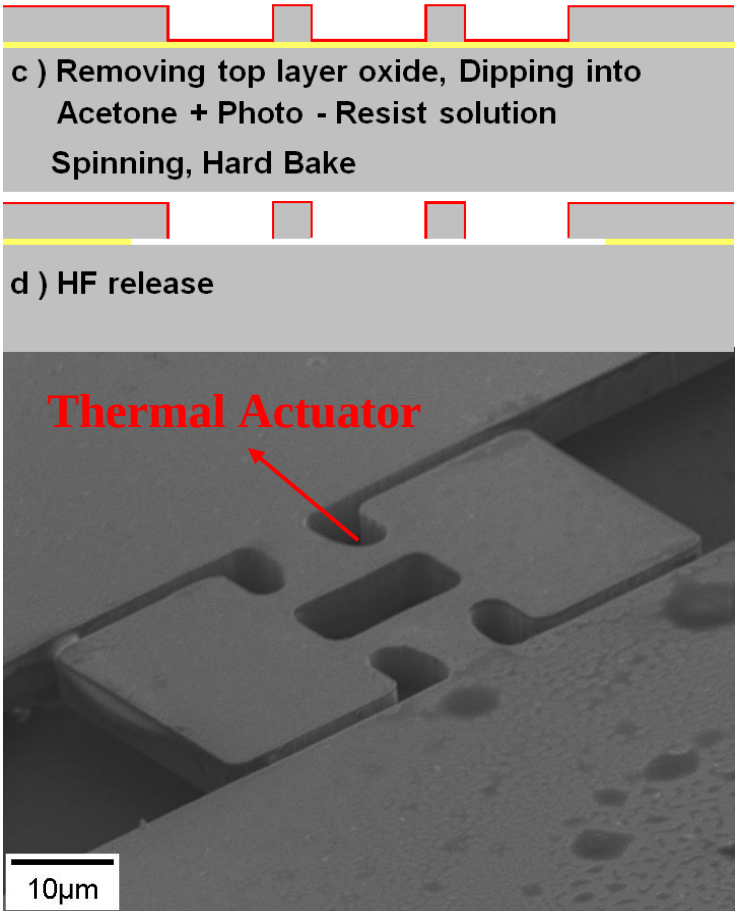

Figure 7.4. Second procedure for coating of the thermally actuated resonators in which the polymer is added before the devices are undercut and undercut is done in hydrofluoric acid after coating with polymer. Also, an SEM picture of a 24MHz I-shaped resonator used for gas sensing and coated using the second method is shown.

However, in this approach the polymer solution (a much higher concentration solution) is added and spin coated at a speed of 3000rpm before the devices are undercut [66]. Undercut is done in hydrofluoric acid after coating with polymer (steps c and d of the fabrication process shown in Fig. 7.4). Using this approach there will be no polymer residue underneath the device structures.

SEM view of a 24MHz I-shaped resonator polymer coated using the abovementioned technique is also shown in Fig. 7.4. This resonator has been fabricated on a SOI substrate with both device layer and BOX thickness of 5μm. This coating method showed a 10x improvement in the sensor frequency response and higher frequency shifts in the 2200 ppm range were achieved.

Although no polymer residues are to be seen underneath the device structures, there are non-uniform residues on the sidewalls and that limits the use of thicker polymer coatings. Such non-uniformities in the deposited mass could also cause a mass imbalance in the resonant structures causing lower quality factors or leaving the devices non-operational.

7.1.3. Utilizing the Photoresist Used for Patterning of the Devices as the Absorbent Polymer Coating

Although the second coating method presented major improvements in the sensor response, getting a thick uniform polymer coating was still a challenge and this fabrication technique suffered from a low process yield. In the third coating technique, the same layer of photoresist used for patterning of the devices, was used as the absorbent layer. For this purpose, as shown in Figure 7.5, the silicon structures were released in hydrofluoric acid (HF) after carving the structures into the SOI device layer (deep

reactive ion etching) without removing the remaining photoresist used as a mask during silicon etch [67]. It should be noted that there was no initial oxidation in this fabrication approach and the photoresist which forms the coating layer of the resonators was used as the mask. Figure 7.6 shows the SEM view of a released polymer coated 15.5MHz resonator. Although HF has damaged and penetrated through the photoresist at various locations on the wirebond pads next to the resonator, the smaller resonator surfaces were able to tolerate the resulting stress quite well and remain intact.

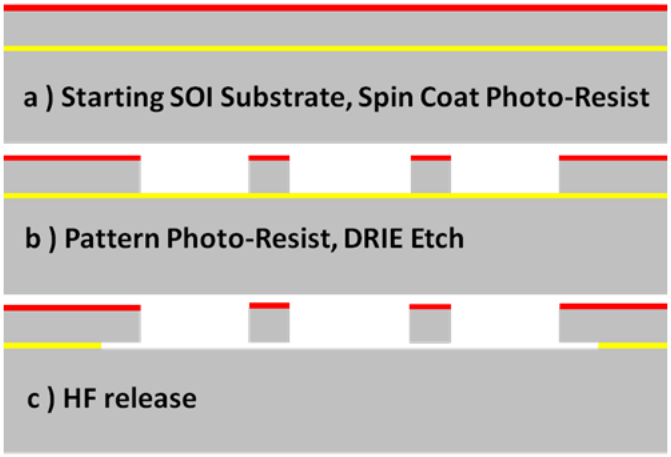

Figure 7.5. Thermally actuated resonator fabrication process flow, in which the photoresist used for the patterning is left on the structure as organic absorbent film. There was no initial oxidation in this fabrication approach and the photoresist which forms the coating layer of the resonators was used as the mask.

Using this approach the coating covers the resonator upper surface very uniformly without leaving behind any residues on the resonator sidewalls or in the gap between the resonant structure and the handle substrate. This fabrication method has allowed ~1.5µm thick polymer coatings to be formed on the surface of the resonator. This has led to higher sensitivities and saturation frequencies in comparison to previous results. Another major advantage associated with this coating procedure is the fact that there are no additional processes required in order to coat the devices.

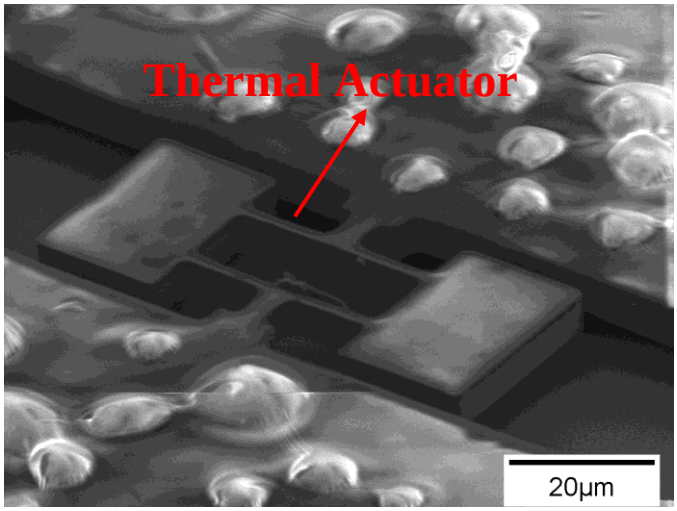

Figure 7.6. A SEM picture of a 15.5MHz I-shaped resonator used as gas sensor and polymer coated using the third mentioned method. The actuating beams are 36 µm long and 3µm wide. The two sensing platforms have a dimension of 31 by 22 µm.

7.2 Resonator Description and Operation

The resonators utilized in this work are referred to as I-Shaped resonators [25,27]. The schematic view of a thermally actuated I-shaped resonator is shown in Figure 7a. The operating principle of such devices have thoroughly been explained [25].

The electrical connections and components required for isolation of the AC actuation current from the DC bias current required for operation of the resonator are also shown in Figure 7.7a.

Figure 7.7b shows the in-plane extensional resonant mode of an I-shaped resonator. In this mode the masses on the two ends of the pillars vibrate back and forth in opposite directions. At resonance, the resistance of the pillars will be modulated by the resulting alternating mechanical stress due to the piezoresistive effect that results in a detectable small signal motional current in the device.

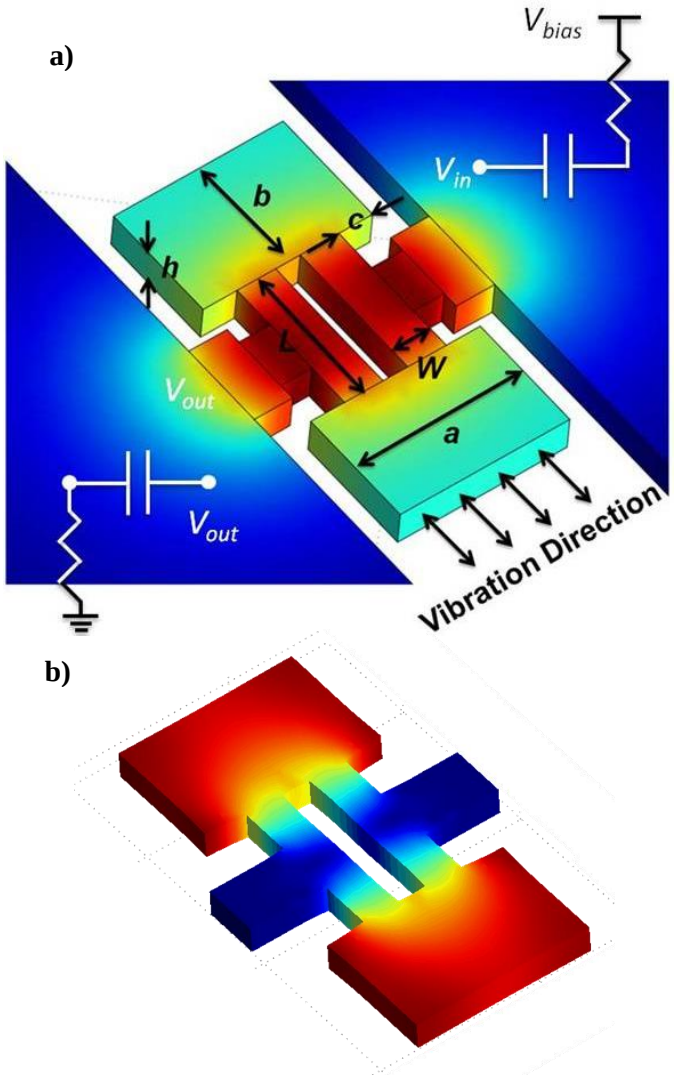

Figure 7.7. a) Schematic view of a thermally actuated I-shaped resonator showing the qualitative distribution of temperature fluctuation amplitude. The electrical connections required for operation of the resonator are also shown; b) COMSOL eigen frequency analysis results, showing the fundamental in-plane resonance mode shape for a thermally actuated I-shaped resonator. Red and blue colors show locations with the largest and smallest vibration amplitudes respectively.

7.3 Measurement Setup and Results

Figure 7.8 shows the schematic diagram of the setup used to characterize the sensory response of the coated resonators. In this setup, nitrogen bubbled through a liquid gasoline/toluene container is directed towards the resonator under test. Having a flow of the gas sample passing over the resonator surfaces maximizes the contact between

potential molecules of interest in the gas sample and the resonator surface, hence, maximizing the absorption probability.

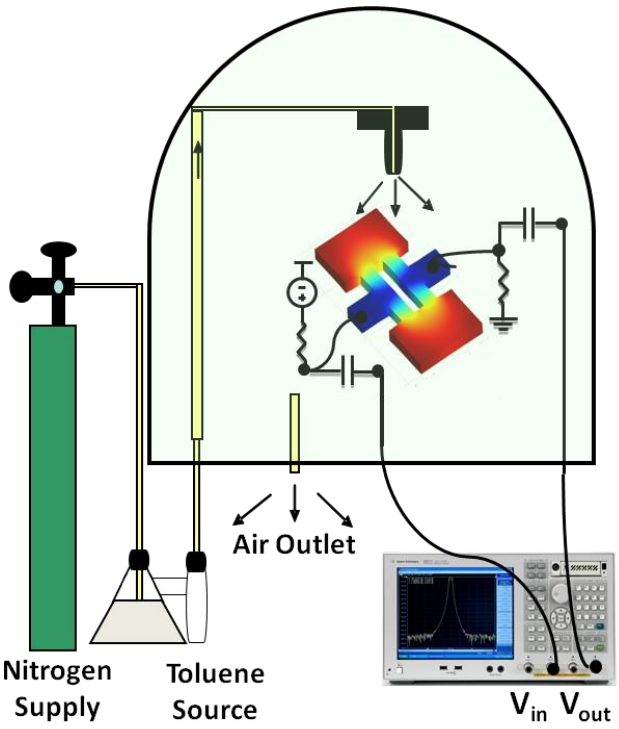

Figure 7.8. Schematic diagram of the setup used in order to characterize the resonator sensory response. Here nitrogen bubbled through a toluene container is directed towards the resonator under test.

Figure 7.9 shows the change in the measured frequency versus time for a resonator fabricated using the first approach. The change in frequency was recorded as the device was being exposed to nitrogen flow rich with gasoline vapor at room temperature.

As can be seen, upon exposure, the resonance frequency reduces over time with a time constant of ~4min. Restoration of the resonant frequency to its initial value happens rather quickly as soon as the source is removed. A relatively small maximum frequency shift of only ~200ppm was achieved [65] which is believed to be due to the thin polymer layer used as the absorbent layer and therefore it was decided to turn to other alternative approaches for coating of the devices.

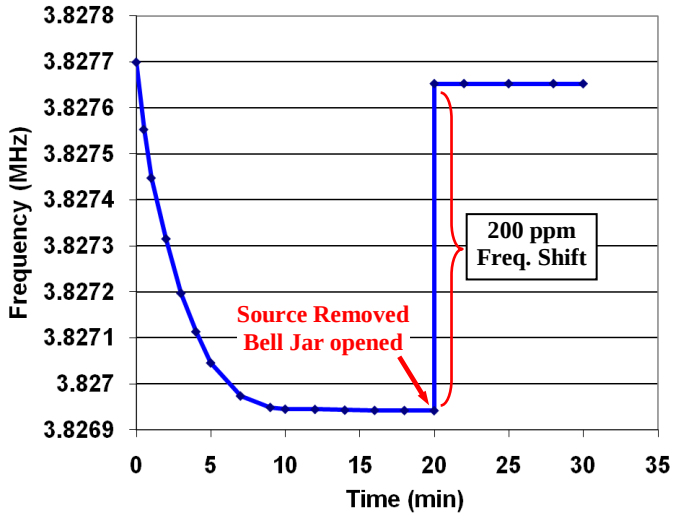

Figure 7.9. Change in the measured resonance frequency as a function of the cumulative exposure time for a 3.8MHz resonator fabricated using the first approach. An overall frequency shift of ~760Hz (198 ppm) is achieved. The gasoline source was removed after 20 min. The return to a frequency close to the initial frequency happens very quickly.

Figure 7.10 shows the change in the measured frequency versus time for the resonator shown in Fig. 7.4 which was coated using the second presented method.

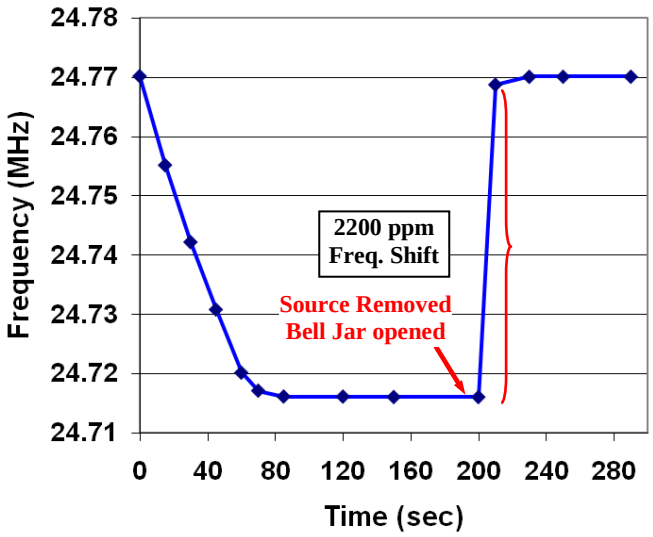

Figure 7.10. Change in the measured resonance frequency for the 24MHz I-shaped resonator of Figure 7.4 as a function of the cumulative exposure time showing an overall frequency shift of ~54kHz (2200 ppm). The source was removed after 200 sec. The return to a frequency very close to the initial frequency is almost instantaneous.

In resonator of Fig 7.4, the releasing of the structure was done after polymer coating). As can be seen, upon exposure of the resonator to gasoline vapor, the resonance frequency

reduces over time with a time constant of ~40sec. Again the resonant frequency is restored to its initial value almost instantaneously. It can be seen that a maximum frequency shift of ~2200ppm is achieved, which is more than 10 times the frequency shift obtained using the first coating procedure.

Figure 7.11 shows the measured resonance frequency of the structure of Figure 7.6 biased at three different currents while going through 3 cycles of toluene absorption/desorption at room temperature. This device was coated using the third mentioned method (the same layer of photoresist used for patterning the device was used as the absorbent polymer layer).

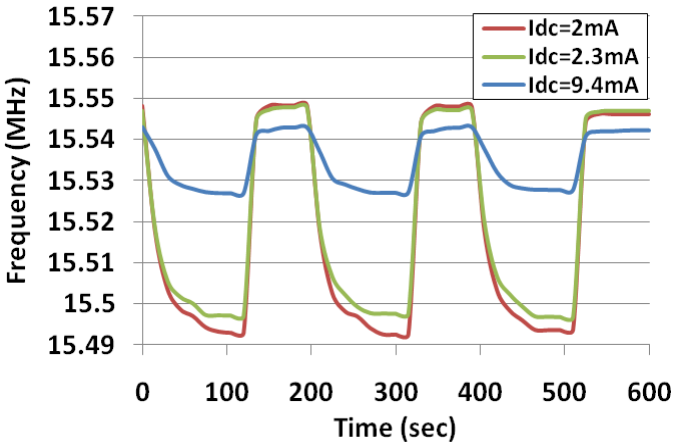

Figure 7.11. Measured frequency response for the 15.5MHz I-shaped resonator of Figure 7.6 as a function of the cumulative exposure time. The three graphs show measurements taken at 3 different bias currents. Maximum frequency shift of ~56KHz (3600 ppm) is obtained at a bias current of 2mA.

Upon exposure to the source, the resonance frequency decreases with a time constant of ~40 sec and again the resonance frequency moves back into its original position once the source is removed. As the resonator bias current and therefore its static temperature increases, the absorbed gas molecules move faster, and collide harder and more often. This leads to more of the gas molecules to break out and the gas absorption capacity to

decrease. The observed maximum frequency shift of 3600ppm (55kHz) at a bias current of 2mA is almost double the highest values measured for the resonators coated through the second technique.

7.3.1. Discussion

The mass sensitivity of the resonators can be theoretically calculated as follows:

$$f = \frac{1}{2\pi}\sqrt{\frac{k}{m}} \Rightarrow \frac{\partial f}{\partial m} = -\frac{f}{2m} \qquad (7.1)$$

where *k*, *m*, and *f* are the effective stiffness, effective mass and resonant frequency of the resonator respectively [25]. Knowing the dimensions and therefore the mass of the resonators, the mass of the absorbed organic molecules (∂m) can be estimated from the measured frequency shifts. Assuming an approximate density of 720 kg/m^3 for the volatile organic compound, the volume and consequently the effective thickness of the absorbed organic compounds (assuming a uniform distribution over the top surface of the coated resonator) can be calculated. In the graph of Figure 7.10, the observed maximum frequency shift of 2200ppm (0.22%) is equivalent to an absorbed organic layer of ~40nm thick. Doing the same calculations for the graph shown in Figure 7.11, the observed maximum frequency shift of 3600 is equivalent to an absorbed organic layer of ~60nm thick.

In order to see how the sensor responds to different gas concentrations, its frequency shift was measured while varying the temperature of the liquid source. Figure 7.12 shows the absolute value of the resonator frequency shift in ppm as a function of the temperature of the liquid source for both devices shown in Figures 7.4 and 7.6. As expected, at lower temperatures the lower organic vapor pressure leads to smaller

frequency shifts. The shift increases sharply (almost exponentially) with temperature (as the vapor pressure increases exponentially with temperature). At about 5ºC, for the sensor shown in Fig7.4, the sensor response starts to saturate and stays constant for temperatures above ~15 ºC. Saturation starts at about ~10 ºC for the sensor shown in Figure 7.6 and stays constant for temperatures above ~20 ºC.

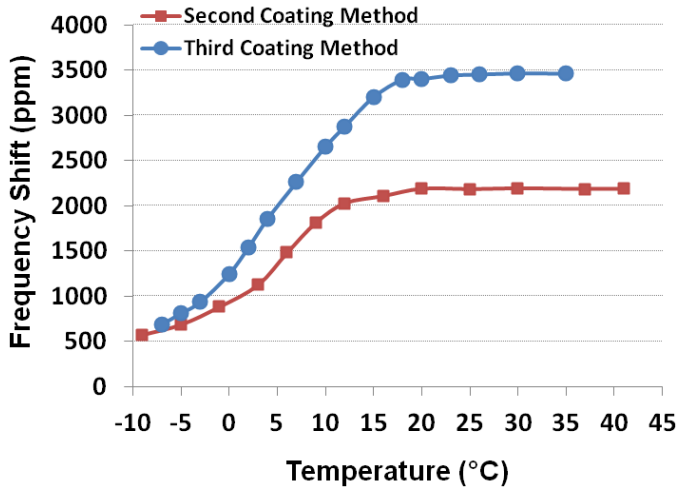

Figure 7.12. The resonator frequency shift as a function of the temperature of the liquid source. The frequency shift increases with temperature as the organic vapor pressure increases. The increase is exponential at lower temperatures, until the sensor reaches saturation.

The vapor pressure of a liquid is an indication of a liquid's evaporation rate which can be calculated through the equation:

$$\ln P = -\frac{\Delta h}{RT} + C \quad or \quad P = e^{(-\frac{\Delta h}{RT}+C)} \tag{7.2}$$

Here Δh is the changes in enthalpy due to evaporation, T is the temperature, R is the mass specific gas constant, P is the liquid vapor pressure and C is a constant. This equation, known as the Clausius–Clapeyron relationship shows that vapor pressure increases exponentially with temperature [68]. Therefore, the vapor pressure of liquid

toluene versus its temperature has an exponential relationship [69]. The graphs depicted in Figure 7.12 follow this trend of showing an almost exponential change in frequency versus the temperature of the liquid source. This is due to the change of vapor pressure with the temperature of the liquid source.

Table 7.1 summarizes the measurement results obtained for different resonators coated using the third method presented. Since the devices have similar absorbent layers and the same structural thickness, the percentage shift in their resonant frequencies is similar. Based on the vapor pressure taken from [69], at a temperature of -10C°, the minimum toluene concentration detected corresponds to ~4000 ppm whereas; assuming a minimum measurable frequency shift of 20Hz for the network analyzer, the minimum limit of detection (LOD) would be ~4.8 ppm.

Therefore high frequency thermally actuated in-plane silicon resonators were successfully used for detection of the presence of organic vapor in air. Three different coating methods were used and the sensitivity achieved using each method was compared. The thickness of the deposited gas vapor on the surface of sensor was calculated according to the change in the resonant frequency of the resonator. The observed maximum frequency shift of 3600ppm (55kHz) was achieved when the same layer of photoresist used for patterning of the devices, was used as the absorbent coating layer for the resonators. This frequency shift is equivalent to an absorbed organic layer of ~60nm thick in liquid form. Minimum LOD measurable is ~4.8 ppm. By using the last coating method, the response times have highly decreased, from ~4min to ~40 seconds.

Table 7-1Summary of measurement results obtained from different resonators at different bias currents and the calculated equivalent absorbed toluene thickness values.

Dimensions (μm) (a/ b / H) (L/W)	Freq. (MHz)	Bias Current (mA)	Q. Factor	Freq. Shift (Hz) (ppm)	Equivalent Toluene Thickness (nm)
31/ 22 / 5 36 / 3	15.5	9.4	4700	-16100 1040	17
		2.3	4500	-50000 3220	55
		2	4400	-55100 3560	60
31 / 22 / 5 36 / 3	14.3	8	3900	-15900 1110	19
		6	3750	-23600 1650	28
		4	3600	-39200 2740	47
		2	3100	-49800 3480	59
35 / 25 / 5 30 / 3	11.1	8	5260	-12600 1135	19
		6	5140	-21200 1910	32
		4	4900	-32800 2955	49
		2	4730	-39100 3520	59

8. CONCLUSIONS AND FUTURE WORKS

8.1 Contributions

The following is a list of contributions that have been achieved in this work.

- Thermally actuated single-crystal silicon in-plane resonators with piezoresistive output detection were successfully fabricated and characterized. The resonators were used for the cumulative mass measurement of airborne micro particles. Not only did the described in-plane thermally actuated flexural resonators maintain high quality factors in air, but they were also very robust and even after deposition of thousands of particles, no significant *Q* degradation was observed for such devices.
- Thermally actuated resonators with frequencies up to 61 MHz were used to measure the mass of individual artificially generated air-borne particles. Mass sensitivities as high as 1.6 kHz/pg were measured for the resonators. Comparison of the measured and calculated mass sensitivities shows a good agreement between the two. Mass measurement of individual arbitrary airborne particles in the cleanroom air sample was carried out using the same resonators. Due to the high mass sensitivity of the devices, individual particles as small as 200 nm in diameter deposited during each period of time could be distinguished. By counting and sizing the number of collected particles in an air volume, the cleanroom was classified. Furthermore, orders of magnitude higher mass sensitivities are achievable by further reducing the thickness and horizontal dimensions of the resonators.
- Self-sustained thermally actuated micromechanical oscillators were fabricated and used as highly sensitive mass sensors for detection of airborne particles. It was shown

that mutual interactions of thermal actuation and the piezoresistive effect can lead to a positive internal feedback loop maintaining mechanical vibrations without the need for a sustaining amplifier. Due to the quantized nature of the frequency shifts, the number of particles deposited during each time interval was distinguishable. Mass sensitivities as high as 31.5Hz/pg were measured for the microbalance sensors.

- Doping induced temperature compensation of thermally actuated N-type single-crystal silicon micromechanical resonators was demonstrated. Measurement data showing the correlation between doping concentration throughout the resonator stiffness elements and resonator TCF was presented showing that as expected, higher doping concentrations lead to less negative (more positive) TCF. While highly suppressed temperature drifts were achieved for highly doped structures, it was observed that the resonator bias current provides an added degree of freedom enabling further fine tuning of the resonator TCF. Temperature compensated resonators with fine tuned overall temperature drifts as low as -3.6ppm over the range of 25ºC to 100ºC were demonstrated. Temperature compensation using the presented technique can not only minimize the temperature drift, but is also expected to improve the short term stability, including phase noise characteristics of oscillators implemented utilizing such frequency references by eliminating the sharp dependence to electronic noise in the resonator bias current.
- Post-fabrication trimming of high frequency thermal-piezoresistive resonators, via localized self-induced thermal oxidation was demonstrated. This post fabrication trimming technique offers the possibility to compensate for all the variations in the

microfabrication processes without compromising on the performance of the resonator. Temperature compensation was also achieved due to the formation of a SiO_2 film on the surface of resonator actuator beams.

- An active frequency tuning mechanism was proposed proven to adjust the resonance frequency of in-plane thermal piezo-resistive micro-electromechanical resonators. Frequency tuning was experimentally carried out in both air and low vacuum by applying an electrostatic force on the device substrate. The frequency tuning showed changes in both directions of the frequency spectrum achieving a maximum tuning range of +580 ppm and -430 ppm in positive and negative directions of the frequency spectrum respectively. Moreover, the performances of the tuned resonators, has shown an improvement in terms of the quality factor.
- High frequency thermally actuated in-plane silicon resonators were successfully used for detection of the presence of organic vapor in air. Three different coating methods were used and the sensitivity achieved using each method was compared. The thickness of the deposited gas vapor on the surface of sensor was calculated according to the change in the resonant frequency of the resonator.

Below is a list of invention disclosures, journal and refereed conference papers, that have so far occurred under this research:

8.1.1 Invention Disclosures

1. S. Pourkamali, A. Rahafrooz and A. Hajjam, "Micromechanical resonators," International Application Number: PCT/US2011/055911, International Filing Date: October 2011, Publication No.: WO/2012/051256, Publication Date: April 2012.

2. S. Pourkamali, and A. Hajjam, “Temperature compensated high-frequency thermally actuated micro/nanomechanical resonators,” Filing Date: September 2010. (Pending)

8.1.2 Journal Publications

1. A. Hajjam, A. Logan, and S. Pourkamali, “Doping induced temperature compensation of thermally actuated high frequency silicon micromechanical resonators,” in IEEE MEMS Journal, vol. 21, issue. 3, pp. 681-687, Jun. 2012.

2. A. Hajjam, and S. Pourkamali, “Fabrication and characterization of MEMS-based resonant organic gas sensors,” in IEEE Sensors Journal, vol. 12, no. 6, pp. 1958-1964, Jun. 2012.

3. A. Hajjam, J. C. Wilson, and S. Pourkamali, “Individual air-borne particle mass measurement using high frequency micromechanical resonators,” in IEEE Sensors Journal, vol. 11, no. 11, pp. 2883-2890, Nov. 2011.

4. A. Hajjam, J. C. Wilson, A. Rahafrooz, and S. Pourkamali, “Fabrication and characterization of thermally actuated micromechanical resonators for airborne particle mass sensing, part II: device fabrication and characterization,” J. of Micromechanics and Micro-engineering (JMM), vol. 20, no. 12, pp. 1-10, Dec. 2010.

8.1.3 Refereed Conference Papers

1. A**.** Hajjam, Y. Guo, K. Dietrich and S. Pourkamali, “MEMS Resonant Human Breath Sensors for Survivor Detection in Disaster Areas,” in press, IEEE Sensors Conference, Taipei, Taiwan, Oct. 2012.

2. A**.** Hajjam, A. Rahafrooz and S. Pourkamali, "Electrostatic frequency tuning and Q-improvement of in-plane dual-plate MEMS resonators," proceedings, IEEE International frequency Control Symposium (IFCS 2012), Baltimore, May 2012.

3. A**.** Hajjam, A. Rahafrooz and S. Pourkamali, "Input-Output insulation in thermal-piezoresisitive resonant microstructures using embedded oxide beams," proceedings, IEEE International frequency Control Symposium (IFCS 2012), Baltimore, May 2012.

4. A. Hajjam, K. Dietrich, A. Rahafrooz, and S. Pourkamali, " A self-controlled frequency trimming technique for micromechanical resonators," proceedings, Hilton Head 2012, solid-state sensor, actuator and Microsystems workshop, June 2012.

5. A**.** Hajjam, A. Rahafrooz, J. Gonzales, R. Abdolvand and S. Pourkamali, "Localized thermal oxidation for frequency trimming and temperature compensation of micromechanical resonators," proceedings, IEEE International Conference on Micro Electro Mechanical Systems (MEMS), Paris, France, Jan. 2012.

6. A. Hajjam, A. Logan, and S. Pourkamali, "Fabrication and characterization of MEMS-based resonant organic gas sniffers" proceedings, IEEE Sensors Conference, Ireland, Nov. 2011.

7. A. Hajjam, A. Logan, J. Pandiyan, and S. Pourkamali, "High frequency thermal-piezoresistive MEMS resonators for detection of organic gases" proceedings, IEEE

International frequency Control Symposium (IFCS 2011), San Francisco, May 2011.

8. A. Hajjam, A. Rahafrooz, and S. Pourkamali, "Temperature compensated single-device electromechanical oscillators," proceedings, IEEE International Conference on Micro Electro Mechanical Systems (MEMS), Cancun, Mexico, Jan. 2011.

9. A**.** Hajjam, J. Wilson, A. Rahafrooz, and S. Pourkamali, "Self-sustained micromechanical resonant particulate microbalance/counters," proceedings, IEEE International Conference on Micro Electro Mechanical Systems (MEMS), Cancun, Mexico, Jan. 2011.

10. A. Hajjam, A. Logan, S. Pourkamali, "Thermally actuated MEMS resonant humidity sensors," proceedings, Covidien R&D Summit, Boulder, Colorado, Jan. 2011.

11. A. Hajjam, A. Rahafrooz, and S. Pourkamali, "Sub-100ppb/ºC temperature stability in thermally actuated high frequency silicon resonators via degenerate phosphorous doping and bias current optimization," proceedings, IEEE International Electron Device Meeting (IEDM), San Francisco, California, Dec. 2010.

12. A.Hajjam, J. Pandiyan, A. Rahafrooz, and S. Pourkamali, "MEMS resonant sensors for detection of gasoline vapor," IEEE Sensors Conference, Waikoloa, Hawaii, Nov. 2010.

13. A. Hajjam, J. Wilson, A. Rahafrooz, and S. Pourkamali, “Detection and mass measurement of individual air-borne particles using high frequency micromechanical resonators,” IEEE Sensors Conference, Waikoloa, Hawaii, Nov. 2010.

14. A. Hajjam, J.C. Wilson, A. Rahafrooz, and S. Pourkamali, “Fabrication and characterization of resonant aerosol particle mass sensors,” Proceedings, IEEE International Conference on Micro Electro Mechanical Systems (MEMS), Hong Kong, Jan. 2010.

15. A. Rahafrooz, A. Hajjam, B. Tousifar, and S. Pourkamali, “Thermal actuation, a suitable mechanism for high frequency electromechanical resonators,” Proceedings, IEEE International Conference on Micro Electro Mechanical Systems (MEMS), Hong Kong, Jan. 2010.

16. B. Harrington, A. Hajjam, J.C. Wilson, S. Pourkamali, R. Abdolvand “Thin-film piezoelectric-on-silicon particle mass sensors,” Proceedings, IEEE International Frequency Control Symposium (IFCS), New Port Beach, California, June 2010.

17. H. Behnam, A. Hajjam and H. Rakhshan, “Modeling twinkling artifact in sonography,” proceedings, IEEE International Conference on Bioinformatics and Biomedical Engineering (ICBBE), Chengdu, China, June 2010.

18. A. Hajjam, A. Rahafrooz, J.C. Wilson, and S. Pourkamali, “Thermally actuated MEMS resonant sensors for mass measurement of micro/nanoscale aerosol particles,” Proceedings, IEEE Sensors, Christchurch, New Zealand, Oct. 2009.

19. A. Hajjam, A. Rahafrooz, and S. Pourkamali, “Thermally actuated low impedance MEMS resonators for mass sensing applications,” Proceedings, IEEE International Conference of Electron Devices and Solid- State Circuits (EDSSC), Xian, China, Jan. 2009.

20. A. Rahafrooz, A. Hajjam, and S. Pourkamali, “Thermal actuation of high frequency micromechanical resonators,” Proceedings, IEEE SOI, San Francisco, California, Oct. 2009.

21. A. Rahafrooz, A. Hajjam, and S. Pourkamali, “Thermally actuated high frequency dimple MEMS resonators,” Proceedings, IEEE Signals and systems, Tunisia, Oct. 2009.

8.2 Future Directions

The developed thermal-piezoresistive MEMS sensors have an ultimately simple fabrication process. The fabricated resonators don’t require any sort of transduction gaps that may be clogged in sensing applications. In addition, their in-plane mode of vibration provides an almost even mass sensitivity which is an advantage in uniform mass sensing applications such as individual particle mass sensing. Such structures have a great potential for commercialization. There are some areas that may require further work:

- Air-borne particle mass sensing: Future work includes further design optimization and miniaturization of the resonator dimensions to achieve higher mass sensitivity. Arrays of devices with different size could be batch fabricated enabling the detection of particles with a variety of size distributions using different devices. Other future

work involves the integration of piezoresistive impact sensing mechanism in the structure of sensor enabling us to measure the impact force (kinetic energy) of the individual particles along with their mass. Combining the mass and energy measurements for individual particles permits the collision velocity to be determined, which leads to the determination of particle size in situations where the velocity is size dependent.

- Localized frequency trimming technique via thermal oxidation: Future directions would be to make it a precise self-controlled frequency trimming technique. The proof of concept for a self-controlled electronic frequency trimming technique has already been demonstrated [70] but further work is required in order for the potential use of this technique for the automatic trimming of a whole batch of resonators after fabrication.
- Volatile organic mass sensing: Using more suitable absorbent polymer coatings and maximization of the absorbing surface area using porous coatings could significantly improve the sensitivity of the sensors. Further characterization of the resonators in terms of their sensitivity towards different concentrations of the organic materials could enhance the selectivity of different coating substrates towards certain materials.
- Two-port resonators: Although having a one-port structure is beneficial (and even mandatory in case of self-sustained sensors), for some applications it is desirable to have two-port thermal-piezoresistive structures. Due to the lower feed through, a two-port resonator can be easily put inside a positive feedback loop to form an oscillator or at least boost its Q. Therefore, unlike a one-port structure, post-data processing and

de-embedding the effects of parasitic and used biasing resistors is not necessary in order to extract the pure resonance behavior of two-port resonators. Some primary research has been done and the results were presented on this topic [ssss], however further research is necessary in this area.

- Higher frequency self-sustained counters: In this research oscillation frequencies up to 6MHz was shown for thermal-piezoresistive resonant sensors. Achieving higher oscillation frequencies could substantially increase the resonator mass sensitivity. There may be the need for new resonator structures to achieve higher frequencies.

REFERENCES

[1] A. Rahafrooz, "High frequency thermally actuated single crystal micromechanical resonators with piezoresistive readout". Ph.D. dissertation, University of Denver, 2011.

[2] C. T. C. Nguyen, "MEMS technology for timing and frequency control," IEEE Trans. on Ultrason., Ferroelectr., Freq. Control, vol. 54, no. 2, pp. 251 – 270, Feb. 2007.

[3] A. Hajjam, J. C. Wilson, A. Rahafrooz, and S. Pourkamali, "Fabrication and characterization of thermally actuated micromechanical resonators for airborne particle mass sensing, part II: device fabrication and characterization," *J. of Micromechanics and Microengineering (JMM)*, vol. 20, no. 12, pp. 1-10, Dec. 2010.

[4] A. Hajjam, and S. Pourkamali, "Fabrication and characterization of MEMS-based resonant organic gas sensors," in *IEEE Sensors Journal*, vol. 12, no. 6, pp. 1958-1964, Jun. 2012.

[5] A. Hajjam, A. Logan, S. Pourkamali, "Thermally actuated MEMS resonant humidity sensors," proceedings, Covidien R&D Summit, Boulder, Colorado, Jan. 2011.

[6] S. Trolier-McKinstry, "Piezoelectric and Acoustic Materials for Transducer Applications." New York: Springer, 2008.

[7] J. Leskinen et al, "Diffusion based nanoparticle monitor using QCM-technology," Proc. European Aerosol Conference, pp. 247-50, 2009.

[8] W. D. Bowers, R. L.Chuan and T. M.Duong, "A 200 MHz surface acoustic wave resonator mass microbalance," Review of Scientific Instruments , vol. 62, Issue 6, pp. 1624 - 1629, 1991.

[9] J .P. Black, A. Elium, R. M. White, M. G. Apte, L A. Gundel, R. Cambie, "MEMS-enabled miniaturized particulate matter monitor employing 1.6 GHz aluminum nitride thin-film bulk acoustic wave resonator (FBAR) and thermophoretic precipitator," Proc. IEEE Ultrasonics Symposium, pp. 476 – 480, 2007.

[10] H. Campanella, "Acoustic wave and electromechanical resonators," *Artech House Publication*, 2010.

[11] Y.Ahn, H .Guckel and J.D.Zook, "Capacitive microbeam resonator design," *J. Micromech. Microeng.* vol.11 pp.70–80, 2001.

[12] D. W. Allen and J. A. Barnes "A modified Allan variance with increased oscillator characterization ability Proc. Freq. Control Symp. pp. 470-475, 1981.

[13] J.H. Seo and O. Brand, "High *Q*-factor in-plane-mode resonant microsensor platform for gaseous/liquid environment," *J. Microelectromech. Syst.*, vol.17, pp.483-493, 2008.

[14] A. Hajjam, A. Rahafrooz, and S. Pourkamali, "Sub-100ppb/ºC temperature stability in thermally actuated high frequency silicon resonators via degenerate phosphorous doping and bias current optimization," proceedings, IEEE International Electron Device Meeting (IEDM), San Francisco, California, Dec. 2010.

[15] J. Weber et al , "Shear mode FBARs as highly sensitive liquid biosensors," *J Sensors & Actuators*, vol. 128, pp.84–8, 2006.

[16] L .Rodriguez-Pardo et al, "Sensitivity, noise, and resolution in QCM sensors in liquid media," *J. IEEE Sensors*, vol.5, pp. 1251-58, 2005.

[17] D. C Woods and R. L Chuan, "Aerosol characterization with a quartz crystal microbalance cascade impactor," Proc. of Advances in Particulate Sampling and Measurements, vol. 22, pp.1639-45, 1979.

[18] P. A. Baron and K. Willeke 2001 Aerosol Measurement, Principles, Techniques and Applications 2nd edn (New York: Wiley-Interscience)

[19] M. Ward and D. Buttry, "In situ interfacial mass detection with piezo-electric transducers," *J science*, vol.249, pp. 1000-6, 1989.

[20] B. Harrington, A. Hajjam, J.C. Wilson, S.Pourkamali, R.Abdolvand "Thin-film piezoelectric-on-silicon particle mass sensors," Proc., IEEE IFCS10, pp. 238-241 2010.

[21] Z. Hao, R. Abdolvand and F. Ayazi, "A high-Q length-extensional bulk-mode mass sensor with annexed sensing platforms," in Proc. IEEE MEMS06, pp. 598-601, 2006.

[22] S. Kim, T. Ono, and M. Esashi, "Capacitive resonant mass sensor with frequency demodulation detection based on resonant circuit," *Appl. Phys. Lett.*, vol. 88, 053116, 2006.

[23] A. Rahafrooz, S. Pourkamali, "Detection of sub-ppm traces of aqueous heavy-metal ions using micro-electro-mechanical beam resonators", *J. Micromechanics and Microengineering*, vol.19, no. 115003. Nov. 2009.

[24] A. Hajjam, J.C. Wilson, A. Rahafrooz and S. Pourkamali, "Detection and mass measurement of individual air-borne particles using high frequency micromechanical resonators," in Proc. IEEE Sensors, pp. 2000-2004 Nov 2010.

[25] A. Hajjam, J. C. Wilson, and S. Pourkamali, "Individual air-borne particle mass measurement using high frequency micromechanical resonators," in *IEEE Sensors Journal*, vol. 11, no. 11, pp. 2883-2890, Nov. 2011.

[26] S. Pourkamali, G. K. Ho and F Ayazi, "Low-impedance VHF and UHF capacitive silicon bulk acoustic wave resonators," *IEEE Trans. Electron Devices*, vol. 54, no. 8, pp. 2017-2023, Aug. 2007.

[27] G.K. Ho, K. Sundaresan, S. Pourkamali, F. Ayazi, "Micromechanical IBARs: tunable high-Q resonators for temperature-compensated reference oscillators," *J. Microelectromech. Syst.*, vol. 19, no. 3, pp. 503-515, Jun. 2010.

[28] T. M Bhide et al, "Shear horizontal surface acoustic wave sensor platform development for chemical and biological detection," *J Anal. Chem*, vol. 73, pp. 5937–44, 2001.

[29] E. Berkenpas et al, "Pure shear horizontal SAW biosensor on langasite," IEEE Trans. Ultrason., Ferroelectr, Freq. Control, vol. 51, pp. 1404–11, 2004.

[30] A. Hajjam, A. Logan, and S. Pourkamali, "Doping induced temperature compensation of thermally actuated high frequency silicon micromechanical resonators," in press, *IEEE MEMS Journal*.

[31] A. Rahafrooz, and S. Pourkamali, "Fully Micromechanical Piezo-Thermal Oscillators," Proceedings, IEEE International Electron Device Meeting (IEDM), 2010.

[32] R. Melamud, et al, "Temperature-insensitive composite micromechanical resonators," in *IEEE Journal of Microelectromechanical Systems*, vol.18, no. 6, pp. 1409–19, Dec. 2009.

[33] Product data sheet, 500 series Temperature Compensated Crystal Oscillators (TCXO), Oscilent Corporation, http://www.oscilent.com/catalog/Category/TCXO_VCXO_VCO.html.

[34] K. Sundaresan, et al, "Electronically temperature compensated silicon bulk acoustic resonator reference oscillator," IEEE J. of Solid State Circuits, vol. 42, pp. 1425-1434, June 2007.

[35] J. C. Salvia et al, "Real-Time temperature compensation of MEMS oscillators using an integrated micro-oven and a Phase-Locked loop", *J. Microelectromech. Syst.*, vol. 19, pp. 192-201, 2009.

[36] C. T.-C. Nguyen and R. T. Howe, "Micro-resonator frequency control and stabilization using an integrated micro oven," in IEEE Transducers Conference, Boston, Jun. 1993, pp. 1040–1043.

[37] C. M. Jha et al, "Thermal isolation of encapsulated MEMS resonators," *J. Microelectromech. Syst.*, vol. 17, pp. 175–184, Feb. 2008.

[38] W.-T. Hsu and C. T.-C. Nguyen, "Stiffness compensated temperature insensitive micromechanical resonators," in IEEE MEMS, Las Vegas, Jan. 2002, pp. 731–734.

[39] R. Tabrizian, G. Casinovi and F. Ayazi, "Temperature-stable high-Q AlN-on-silicon resonators with embedded array of oxide pillars," in. Hilton Head Solid-State Sensors, Actuators, and Microsystems workshop, June 2010, pp. 100-101.

[40] J. S. Wang and K. M. Lakin, "Low-temperature coefficient bulk acoustic wave composite resonators," *Applied Physics Letters*, vol. 40, pp. 308-310, Feb. 1982.

[41] A.K. Samarao, G. Casinovi, F. Ayazi, "Passive TCF compensation in high Q silicon micromechanical resonators", IEEE MEMS, Hong Kong, Jan. 2010, pp. 116–119.

[42] A.K. Samarao, and F. Ayazi, "Temperature compensation of silicon micromechanical resonators via degenerate doping," in IEEE International Electron Device Meeting, Dec. 2009, pp. 789-792.

[43] S. Vepřek, "Electronic and mechanical properties of nanocrystalline composites when approaching molecular size," *J. Thin Solid Films*, vol. 297, Issues 1-2, pp.145-153, Apr. 1997.

[44] W-T. Hsu, A. R. Brown, "Frequency trimming of MEMS resonator oscillators", IEEE Intl. Freq. Control Symp. pp 1088-1091, 2007.

[45] M. A. Abdelmoneum, M. U. Demirci, S.S. Li, and C.T.-C Nguyen, "Post-fabrication laser Trimming of micromechanical filters", *Technical Digest, IEEE Int. Electron Devices*, pp. 39-42, 2004.

[46] A. K. Samarao and F. Ayazi, "Post-fabrication electrical trimming of silicon bulk acoustic resonators using joule heating," Proc. IEEE MEMS Conference, Italy, pp. 892-895, Jan. 2009.

[47] A. Hajjam, A. Rahafrooz, J. Gonzales, R. Abdolvand and S. Pourkamali, "Localized thermal oxidation for frequency trimming and temperature compensation of micromechanical resonators," Proc., IEEE MEMS, Paris, France, Jan. 2012, pp. 704-707.

[48] R.R.A. Syms, "Electrothermal frequency tuning of folded and coupled vibrating micromechanical resonators," *J. Microelectromech. Syst.*, vol. 7, no. 2, pp. 164–171, 1998.

[49] H. Kahn, M.A. Huff, A.H. Heuer, "Heating effects on the Young's modulus of films sputtered onto micromachined resonators," Proc. Mat. Res. Soc., vol. 518 (1998), pp. 33–38

[50] S.G. Adams, F.M. Bertsch, K.A. Shaw, P.G. Hartwell, F.C. Moon, N.C. Macdonald, "Capacitance-based tunable resonators," *J. Micromech. Microeng*, vol. 8, pp. 15–23, 1998.

[51] M. J. Fernandez, J. L. Fontecha, M. C. Horrillo, C. Vera, I. Obieta, and I. Bustero, "Surface acoustic wave gas sensors based on polyisobutylene and carbon nanotube composites," *J. Sensors Actuat. B*, vol. 156, no. 1, pp. 1–5, Aug. 2011.

[52] M. Penza, R. Rossi, M. Alvisi, M. A. Signore, G. Cassano, D. Dimaio, R. Pentassuglia, E. Piscopiello, E. Serra, and M. Falconieri, "Characterization of metal-modified and vertically-aligned carbon nanotube films for functionally enhanced gas sensor applications," *J. Thin Solid Film*, vol. 517, no. 22, pp. 6211–6216, Sep. 2009.

[53] H. Bai and G. Shi, "Gas sensors based on conducting polymer," *J. Sensors*, vol. 7, no. 3, pp. 267–307, 2007.

[54] S. A. Waghuley, S. M. Yenorkar, S. S. Yawale, and S. P. Yawale, "Application of chemically synthesized conducting polymer-polypyrrole as a carbon dioxide gas sensor," *J. Sensors Actuat. B: Chem.*, vol. 128, no. 2, pp. 366–373, Jan. 2008.

[55] Y. T. Li, H. C. Hao, M. C. Chen, T. H. Lin, P. H. Ku, C. M. Yang, K. T. Tang, and D. J. Yao, "Polymer-coated surface acoustic wave sensor array for low concentration NH3 detection," in Proc. IEEE NEMS Conf., Kaohsiung, Taiwan, Feb. 2011, pp. 333–337.

[56] L. A. Mashat, H. D. Tran, W. Wlodarski, R. B. Kaner, and K. Kalantarzadeh, "Polypyrrole nanofiber surface acoustic wave gas sensors," *J. Sensors Actuat. B: Chem.*, vol. 134, no. 2, pp. 826–831, Sep. 2008.

[57] N. V. Quy, V. A. Minh, N. V. Luan, V. N. Hung, and N. V. Hieu, "Gas sensing properties at room temperature of a quartz crystal microbalance coated with ZnO nanorods," *J. Sensors Actuat. B: Chem.*, vol. 153, no. 1, pp. 188–193, Mar. 2011.

[58] M. Harbeck, D. Erbahar, I. Gurol, E. Musluoglu, V. Ahsen, and Z. Ozturk, "Phthalocyanines as sensitive coatings for QCM sensors: Comparison of gas and liquid sensing properties," *J. Sensors Actuat. B: Chem.*, vol. 155, no. 1, pp. 298–303, Jul. 2011.

[59] Y. Hwang, F. Gao, and R. N. Candler, "Porous silicon resonator for sensitive vapor detection," in Proc. Solid State Sensors Actuat. Workshop, 2010, pp. 150–153.

[60] M. C. Liu, C. L. Dai, C. Chan, and C. Wu, "Manufacture of a polyaniline nanofiber ammonia sensor integrated with a readout circuit using the CMOS-MEMS technique," *J. Sensors*, vol. 9, no. 2, pp. 869–880, 2009.

[61] O. Brand, "CMOS-based resonant sensors," in Proc. IEEE Sensors Conf., Irvine, CA, Nov. 2005, pp. 129–132.

[62] L. Khine, J. M. Tsai, A. Heidari, and Y. J. Yoon, "Piezoelectric MEMS resonant gas sensor for defense applications," in Proc. IEEE Defense Sci. Res. Conf., Singapore, Aug. 2011, pp. 1–3.

[63] G. Uma, M. Umapathy, L. B. Vidhya, M. Maya, T. Sophia, and K. Tamilarasi, "Design and analysis of resonant based gas sensor," in *Proc. IEEE Sens. Appl. Symp. Conf.*, Atlanta, GA, Feb. 2008, pp. 119–121.

[64] A. Pandey, G. C. Pandey, and P. B. Aswath, "Synthesis of polylactic acid–polyglycolic acid blends using microwave radiation," *J. Mech. Behavior Biomed. Mater.*, vol. 1, no. 3, pp. 227–233, Jul. 2008.

[65] A. Hajjam, J. Pandiyan, A. Rahafrooz, and S. Pourkamali, "MEMS resonant sensors for detection of gasoline vapor," in Proc. IEEE Sensors Conf., Kona, HI, Nov. 2010, pp. 1538–1541.

[66] A. Hajjam, A. Logan, J. Pandiyan, and S. Pourkamali, "High frequency thermal-piezoresistive MEMS resonators for detection of organic gases," in Proc. IEEE Int. Freq. Cont. Symp., San Francisco, CA, May 2011, pp. 1–5.

[67] A. Hajjam, A. Logan, and S. Pourkamali, "Fabrication and characterization of MEMS-based resonant organic gas sniffers," in Proc. IEEE Sensors Conf., Limerick, Ireland, Oct. 2011, pp. 1–4

[68] M. Galleano, A. Boveris, and S. Puntarulo, "Understanding the Clausius-Clapeyron equation by employing an easily adaptable pressure cooker," *J. Chem. Edu.*, vol. 85, no. 2, pp. 276–278, Feb. 2008.

[69] S. Podhuvan. *Data Sheet, CRC Handbook of Chemistry and Physics* [Online]. Available: http://en.wikipedia.org/wiki/Toluene_(data_page)

[70] A. Hajjam, K. Dietrich, A. Rahafrooz, and S. Pourkamali, " A self-controlled frequency trimming technique for micromechanical resonators," in press, Hilton Head 2012, solid-state sensor, actuator and Microsystems workshop, June 2012.